Signals and Systems Master Thesis

Low-field MR Imaging Using a Nonuniform Fast Fourier Transform

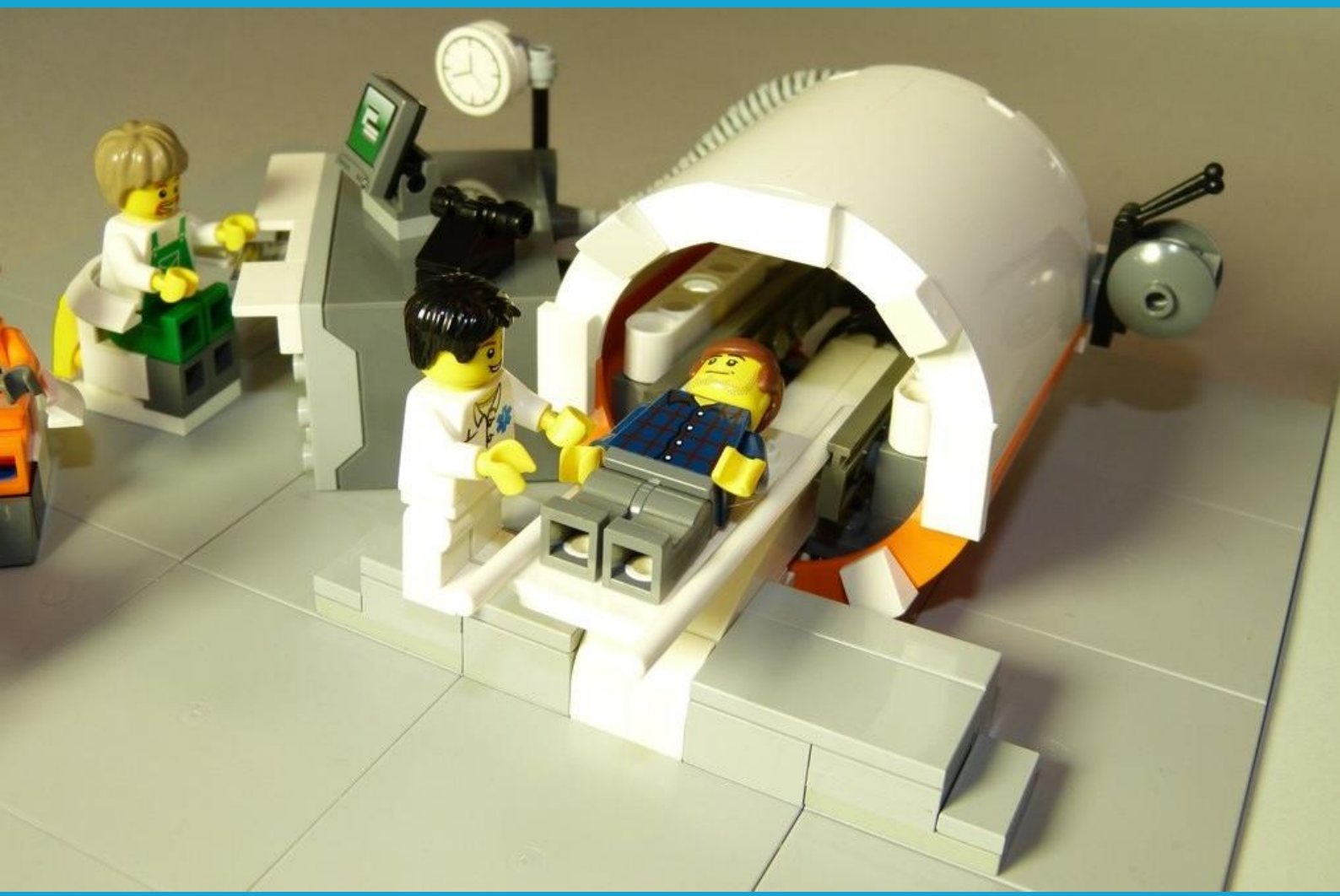

Maria Macarulla Rodriguez

Signals and Systems Master Thesis

Low-field MR Imaging Using a Nonuniform Fast Fourier Transform

by

Maria Macarulla Rodriguez

to obtain the degree of Master of Science
at the Delft University of Technology,
to be defended publicly on Wednesday August 26, 2020 at 10:00 AM.

Student number:	4932293	
Project duration:	December 9, 2019 – August 26, 2020	
Thesis committee:	Dr. ir. R.F. Remis,	TU Delft, supervisor
	Dr. ir. M.B. van Gijzen,	TU Delft
	Prof. dr. A.G. Webb,	LUMC
	Ir. Merel de Leeuw den Bouter,	TU Delft

This thesis is confidential and cannot be made public until August 26, 2020.

TU Delft

Abstract

Low-field Magnetic Resonance Imaging (LF MRI) is a cheap and safe technique to visualise the internal structure of the human body. Unlike other imaging techniques, Magnetic Resonance Imaging does not use ionising radiation to generate the images. Instead, it uses magnetic fields and radio waves which are nonthreatening to the health. The LF MRI scanners are constructed out of inexpensive materials and their maintenance is affordable. Therefore, these scanners are a promising alternative for developing countries that present economic limitations. Nonetheless, since Magnetic Resonance scanners use a weak magnetic field, the process of image reconstruction requires complex algorithms that need time. This thesis will examine the way in which the computational time of the image reconstruction from a low-field Magnetic Resonance Imaging can be reduced, using an algorithm based on the fast Fourier transform.

Keywords— Low-Field Magnetic Resonance Imaging, nonuniform fast Fourier transform, nonlinear gradients, inhomogeneous background field

Acknowledgements

I would like to express my special gratitude to my two supervisors, Dr. Ir. R.F. Remis and Ir. Merel de Leeuw den Bouter. Both have constantly guided me through all of my thesis, helped me improved my research step by step with their precious feedback, reading my report countless times, and correcting all of my mistakes.
To my colleagues from Circuits and Systems and friends, who have been working on their thesis as well, making these research months more bearable.
I would like to thank my parents and sister, with whom I have spent most of the time due to the COVID-19 crisis and who have supported me while working on my thesis. I can never thank them enough for giving me the opportunity and encouraging me to study at TU Delft.

Maria Macarulla Rodriguez
Delft, August 2020

Contents

List of Figures

List of Tables

1 Introduction

Medical imaging is a powerful tool to diagnose. It helps the experts to identify the disease or to detect it earlier, thus avoiding complications. Several medical imaging techniques exist and Magnetic Resonance Imaging (MRI) stands out among the others due to its safety. However, it is an expensive technique and it is out of the range of developing countries. This thesis is focused on the low-field MRI, a cheap alternative to conventional Magnetic Resonance Imaging, to detect a particular disease, namely hydrocephalus, which highly affects developing countries.
This first introductory chapter begins in section 1.1 defining what hydrocephalus is, its treatment, mortality and morbidity, and its effect in Sub-Saharan Africa. Subsequently, in section 1.2, the low-field Magnetic Resonance Imaging is presented along with a brief mention of the state of the art. Section 1.3 presents the purpose of this thesis and section 1.4 its structure.

1.1. Hydrocephalus

Cerebrospinal fluid (CSF) is a transparent liquid present in the brain and spinal cord [11]. Figure 1.1 shows the nervous system in the human brain and it will be helpful for the reader to locate the different parts of the brain that will be mentioned along this introduction.
The cerebrospinal fluid flows through the subarachnoid space, the ventricular system and the central canal of the spinal cord. The CSF has three crucial functions: (1) protection of the brain acting as a shock absorber inside the skull, (2) it transports neurologic substances and nutrients, and (3) it compensates the blood volume changes inside the cranium, keeping constant pressure.
Most of the cerebrospinal fluid is generated in the choroid plexus inside the ventricular system and its volume depends on the age. On average, an adult has around 150 ml and it is renewed every 3 to 4 hours. After it is produced, the CSF travels through the encephalon and spinal cord and eventually, it is reabsorbed in the bloodstream.
Any disorder in the CSF flow (production, travelling or absorption) leads to hydrocephalus. This term comes from the Greek, where *hydor* means water and *kefalé* means head. Hydrocephalus is a neurologic disorder in which the brain accumulates an excess of cerebrospinal fluid. Some of the symptoms of this disorder are memory problems, headaches, motor difficulties or urinary incontinence.
Hydrocephalus can be diagnosed by physical examination, lumbar puncture, Computed Tomography (CT) or Magnetic Resonance Imaging (MRI). Along this thesis, a specific type of MRI will be studied to diagnose hydrocephalus.
Hydrocephalus can be classified into several types depending on different concepts:

- Communicating or noncommunicating. Communicating hydrocephalus occurs when the CSF is blocked after leaving the ventricular system. It can appear after radiation or chemotherapy treatment on the brain, infection or head trauma. Noncommunicating hydrocephalus, also known as obstructive hydrocephalus, happens when the CSF is blocked among the connections of the ventricular system.
- Congenital or acquired. Patients that are born with hydrocephalus correspond to congenital, while acquired hydrocephalus can affect a patient of any age.
- Other classification such as causes of the disorder, age of the patient, neurologic outcomes, etc.
- A classification proposed by [29] is based on different spots of obstruction. They proposed a model of the dynamics of the cerebrospinal fluid based on electrical circuits of Ohm's Law where they show the potential points of obstruction. In most of the cases, tracers are necessary in order to determine which is the place of obstruction.

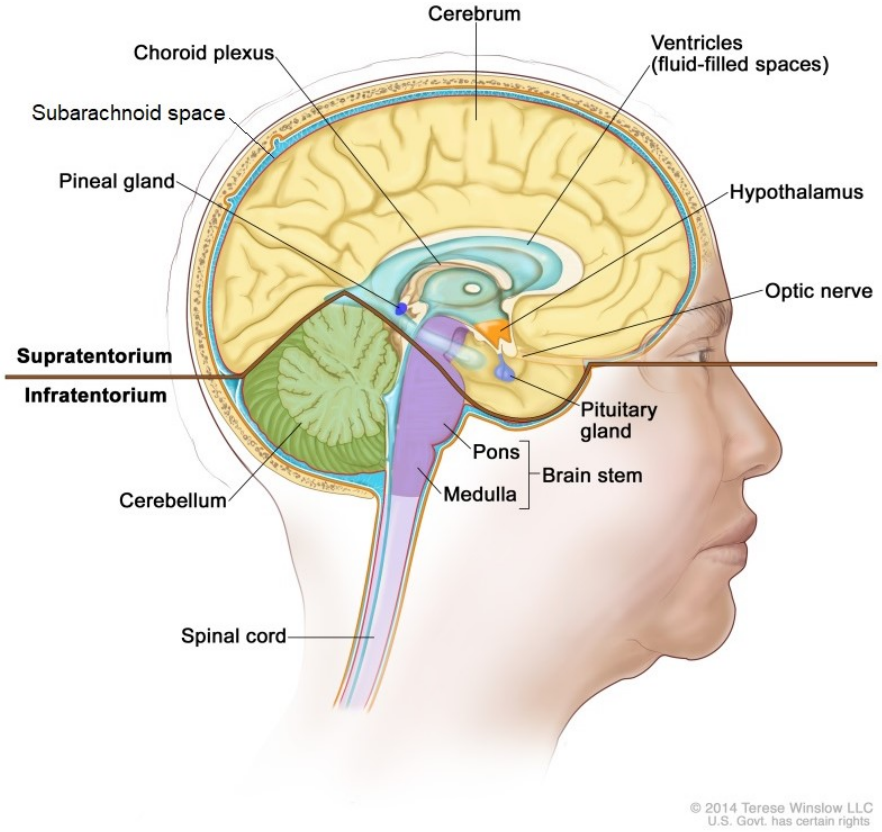

Figure 1.1: Nervous system of the brain where the cerebrospinal fluid is represented with blue colour. Adapted from [3]

1.1.1. Treatment

One of the most ancient methods used to treat hydrocephalus consisted in bandaging the head of the patient in order to reduce the size of the skull [2]. It was not effective and therefore it was dropped out. Other conservative treatments are diet, drugs or radiation. Commonly, conservative treatments are not used due to its inefficiency. An exception is acetazolamide, which reduces the productions of cerebrospinal fluid. It was discovered by Elvidge in 1957 and it has been used since then. Another way to reduce the production of CSF is by irradiating the choroid plexus. Nevertheless, the mentioned treatment has negative collateral effects on the central nervous system due to radiation.

Ventricular puncture was discovered in the forties and it was used as an emergency treatment. The ancestor of ventricular puncture is trephination. This treatment dates from the neolithic times and it consisted in removing a piece of bone from the skull with surgical tools. In many cases it was associated with magical reasons, in order to eliminate evil spirits from the head, but it had also medical background and it was applied to treat hydrocephalus. Ventricular puncture was substituted by external ventricular drainage (EVD) in the seventies since it derived in severe complications such as infections. In EVD, a catheter is inserted into the ventricles of the brain in order to reduce CSF (see figure 1.2). Besides allowing continuous drainage of CSF, EVD possesses more functions such as measuring intracranial pressure or administrating medication.

Subcutaneous reservoir (see figure 1.3) is useful for both drain cerebrospinal fluid and introduce drugs into the brain. A reservoir is placed in the ventricle and it is connected to a dome located over the parietal bones, which are located in the cranial roof and sides of the skull [12].

Shunt (see figure 1.4) was created by Erwin Payr of Greifswald at the beginning of the twentieth century. A shunt is a drainage system that allows CSF to properly flow from the brain to another part of the body where it can be absorb. A drawback is that shunts may require replacement during the lifetime of the patient.

Endoscopic third ventriculostomy (ETV) consists in creating a hole in the third ventricle allowing the CSF to flow out of the brain without any external device (see figure 1.5). It can work as an alternative to shunting. Although it avoids many complications that the shunt procedure presents, such as infections, need for replacement or costs, it can be noneffective for some children. Endoscopic third ventriculostomy might require more than one surgery, and thus increasing the risk of having complications [20].

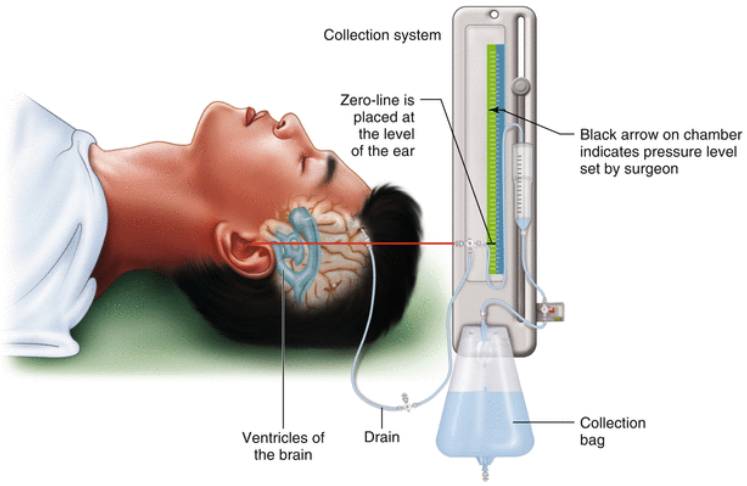

Figure 1.2: External ventricular drainage. Reprinted from [10]

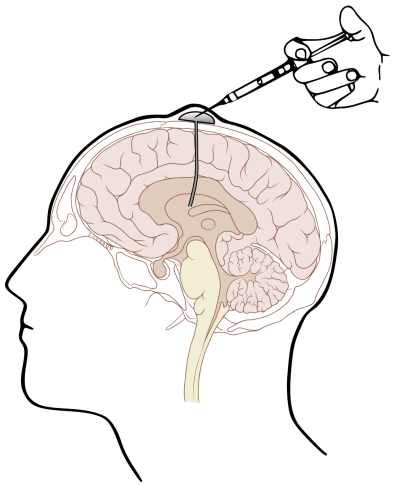

Figure 1.3: Subcutaneous reservoir. Reprinted from [24]

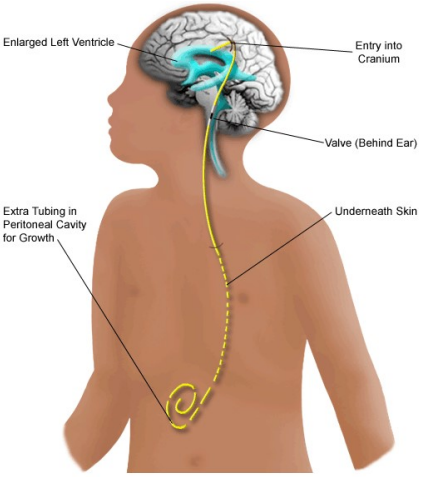

Figure 1.4: Shunt placement. Reprinted from [28]

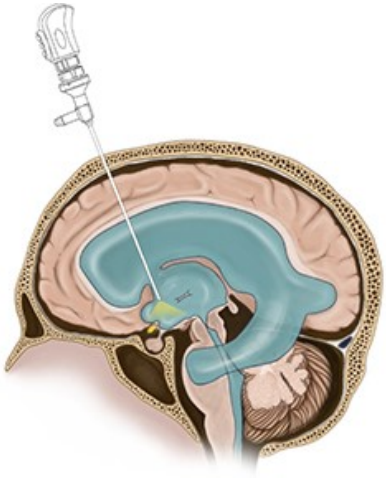

Figure 1.5: Endoscopic third ventriculostomy Reprinted from [16]

1.1.2. Mortality and Morbidity

Hydrocephalus needs to be treated otherwise it can be potentially mortal. An investigation was carried out at the Great Ormond Street Hospital in the United Kingdom [22]. During a period of twenty years, starting in 1938, 239 children that suffered hydrocephalus were followed. A group of 182 patients was not operated and the mortality rate among them was 49%. Many of the not operated survivors showed brain damage.

Moreover, mortality can also be related to complications of treatment. Any surgical intervention supposes a risk, e.g. shunt failure [37]. Shunt problems can be obstruction, over- or under-drainage or infection. The mortality rates before 1960 due to shunt placement were high, from 50% to 80%, and infection was the main cause of death. In the nineties, this mortality was reduced to 4.6% and the causes were infection (16.7%) and mechanical shunt failure (66.7%) [15]. The mortality rates from several studies are collected in [37]: (1) the overall mortality, 14.6%, (2) nontumoral mortality, 8.6%, 13.7%, and (3) the mortality related to shunt, 2.9%, 3.65%.

Morbidity refers to any limitation of the normal life of a patient. Although treated, hydrocephalus can lead to some negative effects on the patient. These include motor complications, brain damage, hearing or vision problems, endocrine dysfunction, epilepsy, depression and pain. Morbidity can be reduced by detecting the disorder at an early stage and by providing the required treatment. One way to detect this disorder is brain imaging with MRI which is what this project is focused on.

Some morbidity rates can be seen in [37] in a table. The highlights of this table related to morbidity problems are depression (43.2%), headache (44%), motor handicap (60%) and visual problems (83%). All of the rates are the worst cases.

1.1.3. Hydrocephalus in Sub-Saharan Africa: Uganda

Hydrocephalus is very usual in developing countries and the main cause is infection. Developing countries have economic limitations and this signifies a constraint in the medicine scope. In some cases, the required instruments or medication to treat the diseases are not available. And even though this equipment is present, many patients cannot afford it.

As mentioned in sections 1.1.1 and 1.1.2, a risk of infection or malfunction exists with shunts. A shunt failure can occur at any time during the lifetime of a patient and it requires immediate surgical intervention. Besides, shunts need after-surgery maintenance. The patients that go through a shunt surgery have to return to the hospital for inspection and transportation is an issue. These complications increase the costs of treatment and therefore, developing countries have to take into account alternative options such as endoscopic third ventriculostomy (ETV).

A study was carried out by [40] at CURE Children's Hospital of Uganda about hydrocephalus, its causes and the performance of ETV treatment, from 2001 to 2003 of 300 children. Seventy percent had a successful ETV surgery and they avoided a shunt placement. Nevertheless, ETV was discarded in 55 patients and ETV treatment had to be replaced by shunt. Distorted anatomy (post-infectious hydrocephaly), turbid CSF and congenital anomaly were the main conditions why ETV was abandoned for those 55 patients. The mortality rate of ETV treatment, including all surgeries (some patients had to undergo several ETV surgeries), was 1.9%.

The incidence of hydrocephalus is 3-5/1000 live births. Although this rate is accurate in first world countries, it is significantly outnumbered in developing countries. The reason is that 60% hydrocephalus cases are due to infection. In 2005, there were 30 million births in sub-Saharan Africa, but since the 60% of hydrocephalus cases are post-infectious, the clinical article [41] estimated that from 225,000 to 375,000 infants had hydrocephalus in that year.

The costs and benefits of the surgeries carried out in one year at CURE Children's Hospital of Uganda in 2005 were calculated in [41]. The results showed that the treatment of hydrocephalus is profitable and sustainable in developing countries: it was concluded that the benefit-cost ratio when treating all patients was 7:1 in the most conservative estimation and 50:1 in the highest. This means that leaving untreated patients in sub-Saharan countries supposes a negative effect on their economy. Whereas preventing and curing hydrocephalus signifies long term benefits. Facilitating medical technology in order to detect hydrocephalus as soon as possible in developing countries would be convenient for their economy.

1.2. Low-Field MRI

Magnetic Resonance Imaging is a technique for image acquisition. It is based in the nuclear magnetic resonance (NMR) phenomenon, where different tissues of a body can be differentiated. Unlike other imaging technologies, such as Computed Tomography (CT) or Positron-emission tomography (PET), MRI does not use ionising radiation and therefore, it is not harmful to the health of the patient being scanned. Moreover, MRI offers high-quality anatomical images. Nonetheless, it is expensive and needs costly maintenance.

Developing countries use CT for brain imaging instead of MRI due to cost reasons. Computed Tomography uses X-rays which are hazardous for humans, in particular for the children. Low-field MRI is a cheap, safe alternative for developing countries instead of the high-field MRI or CT. Low-field MRI uses a weak magnetic field, and thus has low power conditions and minimally or not shielded protection. Although low-field MRI presents low image resolution by comparison with the high-field or CT, it is not an issue in the diagnose of hydrocephalus since only

cerebrospinal fluid has to be differentiated from brain tissue. It is not necessary to distinguish among other brain tissues therefore, not much resolution is needed. Likewise, quality in the image is not necessary to make treatment decisions. Another advantage of LF MRI is that the design of the scanner does not have to be cumbersome since the patients are infants [26]. This thesis is focused on the low-field MRI scanner in Leiden University Medical Center described in [27].

1.2.1. Other Applications of Low-Field MRI Scanner

The characteristics of a low-field MRI make it useful for certain applications of the biomedical field and also for other environments. Some examples are given by [35] using a Laser Polarised Noble Gas Low-field MRI. It can be used as a portable system for diagnostic lung imaging in humans. Moreover, it allows patients with implants (e.g. pacemakers) in. Another application is a low-cost tabletop MRI instrument for research in animals. This MRI system could be on board a space station since it is compatible with operation in restricted environments.
Another interesting application is mention in [7]. It is an ultra-low-field MRI scan that can be used in the baggage checks of the airports in order to detect liquid explosives. This scan was used for two weeks at the Albuquerque International Airport. Although any dangerous items were not found, the ones exceeding the liquid limit were detected.
Low-field MRI can be applied as image guidance during surgery. Low-field MRI was used in [25] for intraoperative neurosurgery. It was tested on 310 patients and none of them had negative effects related to the intraoperative MRI. With this technique, the probability of complete tumour removal is increased. Moreover, the brain shifts caused by movement are avoided by updating the image data.

1.3. Thesis Objective

The procedures employed to retrieve an image from a conventional Magnetic Resonance Imaging are no longer useful for a low-field MRI. The image processing for an LF MRI is more complex and therefore, requires more computational time. In this thesis, an algorithm based on the fast Fourier transform (FFT), the nonuniform fast Fourier transform (NUFFT), will be tested and will be used to try to obtain an image from an LF MRI. This algorithm uses few FFT operations and therefore, it speeds the image processing and saves computational time.

1.4. Structure of the Thesis

This thesis has been divided into three parts, namely

- **Literature Review**. The first part deals with the background knowledge needed to understand the results. First, the signal model of an LF-MRI is derived and then the theory of the nonuniform fast Fourier transform algorithm is explained.
- **Methodology**. The second part clarifies the procedure that will be followed for the results in the third part and how the problem of this thesis will be tackled. Moreover, the algorithms employed will be detailed.
- **Results and Discussion**. The third part exposes and discusses the results of the research, and finalises with the conclusions and future work.

I

Literature Review

2

Signal Detection

In this chapter, the general MRI detection formula will be derived in section 2.2. The generalised MRI signal equation will be modified to match two specific cases, (1) when the main background field presents inhomogeneities, in section 2.3, and (2) when the gradient fields are nonlinear, in section 2.4. In section 2.5, the signal equation will be given when both nonidealities are present.

2.1. Introduction

Signal detection is based on the Nuclear Magnetic Resonance (NMR) phenomenon. The object to be imaged is compounded by different tissues that are made of nuclei. Nuclei with odd atomic numbers and/or odd atomic weight present an angular momentum, also called spin. This is represented in figure 2.1 Another property of nuclei is that they present a magnetic moment when placed in an external magnetic field. Examples of the most important nuclei used in MRI are hydrogen and carbon-13.

Figure 2.1: Nuclei with spin. Reprinted from [6]

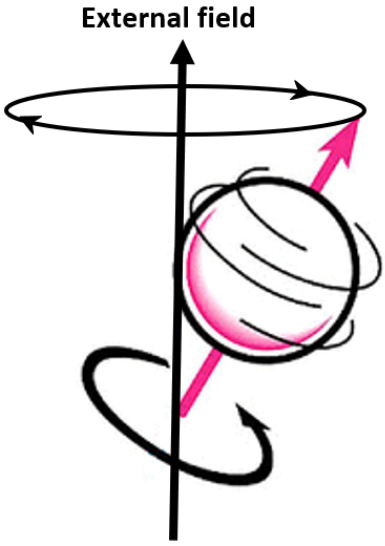

Figure 2.2: Nuclei with spin aligned with the external magnetic field. Adapted from [6]

In the presence of an external magnetic field, nuclei can absorb and emit electromagnetic radiation and have a resonance frequency. Moreover, the external magnetic field aligns the nuclei. This is represented in figure 2.2. When a radio-frequency (RF) pulse is applied to the aligned nuclei, they are tilted. Afterwards, nuclei precess around the magnetic field, emitting an RF signal while going back to the aligned position.
The time that it takes for this RF signal to disappear is different for each type of tissue and it is used to distinguish the different tissues. It is called T2 relaxation. Likewise, the time that a nuclei takes to realign with the external magnetic field is different for each type of tissue and therefore, it is also used to distinguish between tissues. This time is known as T1 relaxation.

2.2. Detection Principles

The next step is to convert the NMR phenomenon into an electrical signal. This procedure will be based on section 3.4 of [23].

The sum of the magnetic properties of the spins form a net magnetisation $\mathbf{M}(\mathbf{r},t)$. Like the individual spins, the net magnetisation is flipped when an RF pulse is applied. Then, it starts to precess at the Larmor frequency around the main magnetic field producing a time-changing magnetic field that can be measured using Faraday's law. Faraday's law of induction states that an electromotive force will be induced in a conductor that is exposed to a time-varying magnetic field. The magnetic flux is defined by

$$\Phi(t) = \int_S \mathbf{B}(\mathbf{r},t) \cdot d\mathbf{S}, \tag{2.1}$$

where $\mathbf{B}(\mathbf{r},t)$ represents the magnetic field that a coil sees, $\mathbf{S}$ is the surface of the coil, $d\mathbf{S}$ corresponds to the infinitesimal vector element of the surface S.

The aim is to set equation (2.1) as a function of the net magnetisation $\mathbf{M}(\mathbf{r},t)$, which is roughly a slice of the desired object. In order to continue with equation (2.1), first some terms must be defined [19].

- Equivalent current distribution of the magnetisation [14]

$$\mathbf{J}_\mathbf{M}(\mathbf{r},t) = \nabla \times \mathbf{M}(\mathbf{r},t). \tag{2.2}$$

- Magnetic vector potential, according to [17] and [19]

$$\mathbf{A}(\mathbf{r},t) = \frac{\mu_0}{4\pi} \int_{object} \frac{\mathbf{J}_\mathbf{M}(\mathbf{r}',t)}{|\mathbf{r}-\mathbf{r}'|} d\mathbf{r}'. \tag{2.3}$$

- Magnetic field

$$\mathbf{B}(\mathbf{r},t) = \nabla \times \mathbf{A}(\mathbf{r},t) \tag{2.4}$$

Using Stokes' theorem [18], equation (2.1) leads to

$$\Phi(t) = \int_S \mathbf{B}(\mathbf{r},t) \cdot d\mathbf{S} = \oint_{\delta S} \mathbf{A}(\mathbf{r},t) \cdot d\mathbf{r}. \tag{2.5}$$

Where S is the coil surface bounded by the closed contour δS, $\mathbf{B}(\mathbf{r},t)$ corresponds to the magnetic field and $\mathbf{A}(\mathbf{r},t)$ to the magnetic vector potential. Continuing with the right-hand side of equation (2.5) and equations (2.2), (2.3) and (2.4)

$$\Phi(t) = \frac{\mu_0}{4\pi} \oint_{\delta S} \int_{object} \frac{\mathbf{J}_\mathbf{M}(\mathbf{r}',t)}{|\mathbf{r}-\mathbf{r}'|} d\mathbf{r}' \cdot d\mathbf{r} = \frac{\mu_0}{4\pi} \int_{object} \oint_{\delta S} \frac{\nabla_{\mathbf{r}'} \times \mathbf{M}(\mathbf{r}',t)}{|\mathbf{r}-\mathbf{r}'|} \cdot d\mathbf{r} d\mathbf{r}' \tag{2.6}$$

Using the following chain rule

$$\begin{aligned} \nabla \times (\mathbf{aM}) &= (\nabla \mathbf{a}) \times \mathbf{M} + (\mathbf{a}\nabla) \times \mathbf{M}, \\ (\mathbf{a}\nabla) \times \mathbf{M} &= \nabla \times (\mathbf{aM}) - (\nabla \mathbf{a}) \times \mathbf{M}, \end{aligned} \tag{2.7}$$

where

$$(\mathbf{a}\nabla) \times \mathbf{M} = \frac{\nabla_{\mathbf{r}'} \times \mathbf{M}(\mathbf{r}',t)}{|\mathbf{r}-\mathbf{r}'|}, \tag{2.8}$$

gives

$$\Phi(t) = \frac{\mu_0}{4\pi} \int_{object} \oint_{\delta S} \left(\nabla_{\mathbf{r}'} \times \frac{\mathbf{M}(\mathbf{r}',t)}{|\mathbf{r}-\mathbf{r}'|} - \left(\nabla_{r'} \frac{1}{|\mathbf{r}-\mathbf{r}'|} \right) \times \mathbf{M}(\mathbf{r}',t) \right) \cdot d\mathbf{r} d\mathbf{r}'. \tag{2.9}$$

Since the object is finite, the term $\nabla_{\mathbf{r}'} \times \frac{\mathbf{M}(\mathbf{r}',t)}{|\mathbf{r}-\mathbf{r}'|}$ disappears.

$$\begin{aligned} \Phi(t) &= \frac{\mu_0}{4\pi} \int_{object} \oint_{\delta S} \left(\left(-\nabla_{r'} \frac{1}{|\mathbf{r}-\mathbf{r}'|} \right) \times \mathbf{M}(\mathbf{r}',t) \cdot d\mathbf{r} \right) d\mathbf{r}' \\ &= \frac{\mu_0}{4\pi} \int_{object} \oint_{\delta S} \left(\left(\frac{\mathbf{r}-\mathbf{r}'}{|\mathbf{r}-\mathbf{r}'|^3} \right) \times \mathbf{M}(\mathbf{r}',t) \cdot d\mathbf{r} \right) d\mathbf{r}'. \end{aligned} \tag{2.10}$$

Using the triple product rule

$$\mathbf{b} \times \mathbf{M} \cdot d\mathbf{r} = -\mathbf{M} \cdot \mathbf{b} \times d\mathbf{r} \tag{2.11}$$

results in

$$\begin{aligned} \Phi(t) &= -\frac{\mu_0}{4\pi} \int_{object} \oint_{\delta S} \left(\mathbf{M}(\mathbf{r}',t) \cdot \frac{\mathbf{r}-\mathbf{r}'}{|\mathbf{r}-\mathbf{r}'|^3} \times d\mathbf{r} \right) d\mathbf{r}' \\ &= \int_{object} \mathbf{B}_\mathbf{r}(\mathbf{r}') \cdot \mathbf{M}(\mathbf{r}',t) d\mathbf{r}'. \end{aligned} \tag{2.12}$$

Where $\mathbf{M}(\mathbf{r}', t)$ is one slice of the desired object and

$$\mathbf{B}_\mathbf{r}(\mathbf{r}') = \frac{\mu_0}{4\pi} \oint_{\delta S} \frac{d\mathbf{r} \times (\mathbf{r} - \mathbf{r}')}{|\mathbf{r} - \mathbf{r}'|^3} \tag{2.13}$$

corresponds to the receiver coil sensitivity, i.e. the magnetic field that would be created at point $\mathbf{r}'$ by an unit steady current in the receiver coil.
Now that the magnetic flux $\Phi(t)$ depends on the net magnetisation $\mathbf{M}(\mathbf{r}', t)$, the aim is to measured the voltage. As said before, Faraday's law of induction states that an electromotive force will be induced in a coil that is exposed to a time-varying magnetic field. Therefore, the voltage is obtained as

$$V(t) = -\frac{\partial \Phi(t)}{\partial t}. \tag{2.14}$$

Substituting equation (2.12) in (2.14) and replacing $\mathbf{r}'$ with $\mathbf{r}$ to simplify the notation leads to

$$V(t) = -\frac{\partial}{\partial t} \int_{object} \mathbf{B}_\mathbf{r}(\mathbf{r}) \cdot \mathbf{M}(\mathbf{r}, t) d\mathbf{r}. \tag{2.15}$$

Equation (2.15) is the fundamental formula of MR signal detection. Reformulating it in scalar form with the decomposition $\mathbf{B}_\mathbf{r} = B_{r,x}\mathbf{i} + B_{r,y}\mathbf{j} + B_{r,z}\mathbf{k}$, we get

$$V(t) = -\frac{\partial}{\partial t} \int_{object} \left[B_{r,x}(\mathbf{r}) M_x(\mathbf{r}, t) + B_{r,y}(\mathbf{r}) M_y(\mathbf{r}, t) + B_{r,z}(\mathbf{r}) M_z(\mathbf{r}, t) \right] d\mathbf{r}. \tag{2.16}$$

The z component in (2.16) can be discarded since the longitudinal relaxation T1 is slow varying compared with the transverse relaxation T2. In a 3 Tesla MRI scanner, T1 values are around 1000 ms, while T2 values are around 100 ms in the brain tissues [39].

$$V(t) = -\int_{object} \left[B_{r,x}(\mathbf{r}) \frac{\partial M_x(\mathbf{r}, t)}{\partial t} + B_{r,y}(\mathbf{r}) \frac{\partial M_y(\mathbf{r}, t)}{\partial t} \right] d\mathbf{r}. \tag{2.17}$$

We continue working on the equation (2.17). The magnetic field can be expressed as

$$B_{r,x}(\mathbf{r}) = |B_{r,xy}(\mathbf{r})| \cos \phi_r(\mathbf{r}), \tag{2.18a}$$
$$B_{r,y}(\mathbf{r}) = |B_{r,xy}(\mathbf{r})| \sin \phi_r(\mathbf{r}). \tag{2.18b}$$

In which ϕ_r is the reception phase angle and $\phi_r \in [0, 2\pi]$. To calculate the time-derivative terms of equation (2.17), the free precession equations are taken from chapter 3 in [23]

$$M_x(\mathbf{r}, t) = |M_{xy}(\mathbf{r}, 0)| \mathrm{e}^{-t/T_2(\mathbf{r})} \cos[-\omega(\mathbf{r})t + \phi_e(\mathbf{r})], \tag{2.19a}$$
$$M_y(\mathbf{r}, t) = |M_{xy}(\mathbf{r}, 0)| \mathrm{e}^{-t/T_2(\mathbf{r})} \sin[-\omega(\mathbf{r})t + \phi_e(\mathbf{r})]. \tag{2.19b}$$

Where ϕ_e is the initial phase shift introduced by the RF pulse and $\phi_e \in [0, 2\pi]$. The transverse relaxation is represented by T_2. The negative sign preceding $\omega(\mathbf{r})$ indicates that the spins precess clockwise.
Proceeding with the time derivation, the following equations are obtained

$$\begin{aligned} \frac{\partial M_x(\mathbf{r}, t)}{\partial t} &= \omega(\mathbf{r}) |M_{xy}(\mathbf{r}, 0)| \mathrm{e}^{-t/T_2(\mathbf{r})} \sin[-\omega(\mathbf{r})t + \phi_e(\mathbf{r})] \\ &\quad - \frac{1}{T_2(\mathbf{r})} |M_{xy}(\mathbf{r}, 0)| \mathrm{e}^{-t/T_2(\mathbf{r})} \cos[-\omega(\mathbf{r})t + \phi_e(\mathbf{r})], \end{aligned} \tag{2.20a}$$

$$\begin{aligned} \frac{\partial M_y(\mathbf{r}, t)}{\partial t} &= -\omega(\mathbf{r}) |M_{xy}(\mathbf{r}, 0)| \mathrm{e}^{-t/T_2(\mathbf{r})} \cos[-\omega(\mathbf{r})t + \phi_e(\mathbf{r})] \\ &\quad - \frac{1}{T_2(\mathbf{r})} |M_{xy}(\mathbf{r}, 0)| \mathrm{e}^{-t/T_2(\mathbf{r})} \sin[-\omega(\mathbf{r})t + \phi_e(\mathbf{r})]. \end{aligned} \tag{2.20b}$$

T_2 relaxation is much slower (order of hundred milliseconds) than the free precession rate or Larmor frequency $\omega(\mathbf{r})$ (order of megahertz)

$$\omega(\mathbf{r}) >> \frac{1}{T_2(\mathbf{r})}. \tag{2.21}$$

Therefore, the last term from both (2.20) equations is omitted, getting

$$\frac{\partial M_x(\mathbf{r}, t)}{\partial t} = \omega(\mathbf{r}) |M_{xy}(\mathbf{r}, 0)| \mathrm{e}^{-t/T_2(\mathbf{r})} \sin[-\omega(\mathbf{r})t + \phi_e(\mathbf{r})], \tag{2.22a}$$
$$\frac{\partial M_y(\mathbf{r}, t)}{\partial t} = -\omega(\mathbf{r}) |M_{xy}(\mathbf{r}, 0)| \mathrm{e}^{-t/T_2(\mathbf{r})} \cos[-\omega(\mathbf{r})t + \phi_e(\mathbf{r})]. \tag{2.22b}$$

Now equations (2.18) and (2.22) are substituted into (2.17) giving

$$V(t) = -\int_{object} \big(|B_{r,xy}(\mathbf{r})| \cos\phi_r(\mathbf{r})\omega(\mathbf{r})|M_{xy}(\mathbf{r},0)|\mathrm{e}^{-t/T_2(\mathbf{r})} \sin[-\omega(\mathbf{r})t + \phi_e(\mathbf{r})] \\ -|B_{r,xy}(\mathbf{r})| \sin\phi_r(\mathbf{r})\omega(\mathbf{r})|M_{xy}(\mathbf{r},0)|\mathrm{e}^{-t/T_2(\mathbf{r})} \cos[-\omega(\mathbf{r})t + \phi_e(\mathbf{r})]\big)d\mathbf{r}. \tag{2.23}$$

Making use of two trigonometric function

$$\sin(\alpha - \beta) = \cos\beta \sin\alpha - \sin\beta \cos\alpha, \tag{2.24}$$

in the equation (2.23) gives

$$V(t) = -\int_{object} \omega(\mathbf{r})|B_{r,xy}(\mathbf{r})||M_{xy}(\mathbf{r},0)|\mathrm{e}^{-t/T_2(\mathbf{r})} \sin[-\omega(\mathbf{r})t + \phi_e(\mathbf{r}) - \phi_r(\mathbf{r})]d\mathbf{r}. \tag{2.25}$$

Since the transverse magnetisation $M_{xy}(\mathbf{r},0)$ precesses at the Larmor frequency, the corresponding voltage signal $V(t)$ is at high frequency as well. Therefore, this signal is demodulated with the phase-sensitive detection (PSD) method in order to move it to lower frequencies and simplify the signal processing. This method is done by multiplying the voltage signal by a sinusoidal signal and eliminating the high frequency components by low-pass filtering it.
It is necessary to use a quadrature detection to have information about the direction of rotation of ω. This is achieved by using two PSD system orthogonal to each other. Therefore, two reference signals are multiplied on equation (2.25), $2\cos\omega_0 t$ and $2\sin\omega_0 t$, and they are represented by $S_R(t)$ and $S_I(t)$ respectively.

$$S_R(t) = \int_{object} \omega(\mathbf{r})|B_{r,xy}(\mathbf{r})||M_{xy}(\mathbf{r},0)|\mathrm{e}^{-t/T_2(\mathbf{r})} \cos\left[-\omega(\mathbf{r})t + \omega_0 t + \phi_e(\mathbf{r}) - \phi_r(\mathbf{r}) + \frac{\pi}{2}\right]d\mathbf{r}, \tag{2.26}$$

$$S_I(t) = \int_{object} \omega(\mathbf{r})|B_{r,xy}(\mathbf{r})||M_{xy}(\mathbf{r},0)|\mathrm{e}^{-t/T_2(\mathbf{r})} \sin\left[-\omega(\mathbf{r})t + \omega_0 t + \phi_e(\mathbf{r}) - \phi_r(\mathbf{r}) + \frac{\pi}{2}\right]d\mathbf{r}. \tag{2.27}$$

Furthermore, $\omega(\mathbf{r})$ can be reformulated taking into account the spatial dependency of the resonance frequency as

$$\omega(\mathbf{r}) = \omega_0 + \Delta\omega(\mathbf{r}). \tag{2.28}$$

Where ω_0 refers to the frequency associated to the main magnetic field B_0, i.e. $\omega_0 = \gamma B_0$, where γ is the gyromagnetic ratio. Equations (2.26) and (2.27) are simplified using equation (2.28) to

$$S_R(t) = \omega_0 \int_{object} |B_{r,xy}(\mathbf{r})||M_{xy}(\mathbf{r},0)|\mathrm{e}^{-t/T_2(\mathbf{r})} \cos\left[-\Delta\omega(\mathbf{r})t + \phi_e(\mathbf{r}) - \phi_r(\mathbf{r}) + \frac{\pi}{2}\right]d\mathbf{r}, \tag{2.29}$$

$$S_I(t) = \omega_0 \int_{object} |B_{r,xy}(\mathbf{r})||M_{xy}(\mathbf{r},0)|\mathrm{e}^{-t/T_2(\mathbf{r})} \sin\left[-\Delta\omega(\mathbf{r})t + \phi_e(\mathbf{r}) - \phi_r(\mathbf{r}) + \frac{\pi}{2}\right]d\mathbf{r}. \tag{2.30}$$

The two components $S_R(t)$ and $S_I(t)$ are used to express the signal in complex form using Euler's formula $\mathrm{e}^{ix} = \cos x + i\sin x$

$$S(t) = \omega_0 \int_{object} |B_{r,xy}(\mathbf{r})||M_{xy}(\mathbf{r},0)|\mathrm{e}^{-t/T_2(\mathbf{r})}\mathrm{e}^{-i\left[\Delta\omega(\mathbf{r})t - \phi_e(\mathbf{r}) + \phi_r(\mathbf{r}) - \frac{\pi}{2}\right]}d\mathbf{r}. \tag{2.31}$$

Expressing the terms $|B_{r,xy}(\mathbf{r})|$ and $|M_{xy}(\mathbf{r},0)|$ in complex form we get

$$|B_{r,xy}(\mathbf{r})|\mathrm{e}^{-i\phi_r(\mathbf{r})} = B^*_{r,xy}(\mathbf{r}), \tag{2.32a}$$

$$|M_{xy}(\mathbf{r},0)|\mathrm{e}^{i\phi_e(\mathbf{r})} = M_{xy}(\mathbf{r},0). \tag{2.32b}$$

Where $B^*_{r,xy}(\mathbf{r})$ indicates the conjugate of $B_{r,xy}(\mathbf{r})$. Applying both equations into equation (2.31) and omitting the constant $\omega_0\mathrm{e}^{i\frac{\pi}{2}}$ and the T2 relaxation for simplification

$$S(t) = \int_{object} B^*_{r,xy}(\mathbf{r})M_{xy}(\mathbf{r},0)\mathrm{e}^{-i\Delta\omega(\mathbf{r})t}d\mathbf{r}. \tag{2.33}$$

Assuming a uniform distributed sensitivity in the receiver coil and discarding off-resonance effects we get

$$S(t) = \int_{object} M_{xy}(\mathbf{r},0)\mathrm{e}^{-i\omega t}d\mathbf{r}. \tag{2.34}$$

The preceding formula is the final signal expression for a homogeneous field in the region of interest, where M_{xy} denotes the transverse magnetisation at position $\mathbb{r}$ and ω corresponds to the precessional frequency. In this case, M_{xy} can be retrieved using a Fourier transform. However, in low-field MRI, inhomogeneities and nonlinear effects are present in the field and a conventional Fourier transform causes artefacts in the image.
In the following sections 2.3 and 2.4, the nonideal effects will be modeled.

2.3. Background Field Inhomogeneities

While HF-MRI have strong main magnetic field, around several Tesla, LF-MRI is weak (order of mT). This causes inhomogeneities in the background field, both magnitude and direction.
The magnetic field distribution is no longer constant and it is rewritten as follows

$$B(\mathbf{r}) = B_0 + \Delta B(\mathbf{r}), \tag{2.35}$$

then

$$\Delta\omega(\mathbf{r}) = \gamma \Delta B(\mathbf{r}). \tag{2.36}$$

Substituting (2.36) in (2.34)

$$S(t) = \int_{object} M_{xy}(\mathbf{r}, 0) \mathrm{e}^{-i\gamma \Delta B(\mathbf{r}) t} d\mathbf{r}. \tag{2.37}$$

Equation (2.37) is the signal expression for an inhomogeneous static field, $\Delta B(\mathbf{r})$ depends on the location [8][32]. It can be rewritten in one dimension and with discrete notation [4]

$$S(k_x) = \sum_{p=0}^{N-1} M_x(x_p) \mathrm{e}^{-i\gamma \Delta B(x_p) k_x} \Delta x, \quad 0 \leq k_x \leq N-1. \tag{2.38}$$

In which k_x correspond to k-space components, frequency domain, and x_p is the position at the pth sample in the space domain. Note that the size of the pixel must be taken into account and this is represented by Δx. The number of samples is N.
The two-dimensional signal equation is expressed in discrete form likewise

$$S(k_x, k_y) = \sum_{p=0}^{m-1} \sum_{q=0}^{n-1} M_x(x_p, y_q) \mathrm{e}^{-i\gamma\left(\Delta B(x_p, y_q) k_x + \Delta B(x_p, y_q) k_y\right)} \Delta x \Delta y, \quad \begin{matrix} 0 \leq k_x \leq m-1, \\ 0 \leq k_y \leq n-1. \end{matrix} \tag{2.39}$$

In which the total number of samples is $N = mn$.

2.4. Nonlinear Gradient Fields

Linear gradient magnetic fields are used to spatially encode the signal received. For instance, a gradient along the z-direction would be applied in order to select one transverse slice of the object. In figure 2.3, a linear gradient field is present and it gives a different Larmor frequency of the nuclei along the z-axis. When applying an RF pulse with the frequency associated to the desired slice, i.e. $\omega = \gamma B$, the magnetisation of the nuclei flips into the transverse plane, giving a signal. On the other hand, figure 2.4 represents the gradient field that a low-field MRI would generate. As the previous case in figure 2.3, we desired an image of the brain and therefore, the pertinent RF pulse is applied. However, this frequencies are not unique for the head, and nuclei from the neck of the patient are tilted as well, introducing noise to the image. In other words, several space locations have the same frequencies and this is known as nonbijective encoding.
The linearity of these fields depends on the geometry of the coils. A less complex coil system, such as in low-field MRI, causes nonlinearities [9].
Expressing equation (2.34) in one dimension and supposing a homogeneous main field and nonlinear gradients we get

$$S(t) = \int_{FOV_x} M_x(x) \mathrm{e}^{-i\gamma\left(B_0 t + B(x) \int_0^t f_x(\tau) d\tau\right)} dx. \tag{2.40}$$

Where FOV_x is the Field of View in the x direction, $B_x(x)$ represents the gradient field depending on the x direction and f_x is its temporal dependence. Assuming that the gradient magnetic field has the form [21][42]

$$B_x(x) = xG_x + H_x(x), \tag{2.41}$$

where G_x is a constant and $H_x(x)$ represents the nonlinearities [34], and demodulating the signal, the preceding equation leads to

$$S(t) = \int_{FOV_x} M_x(x) \mathrm{e}^{-i\gamma\left(xG_x + H_x(x)\right)t} dx. \tag{2.42}$$

Writing this in discrete form

$$S(k_x) = \sum_{p=0}^{N-1} M_x(x_p) \mathrm{e}^{-i\gamma\left(x_p G_x + H_x(x_p)\right)k_x} \Delta x, \quad 0 \leq k_x \leq N-1, \tag{2.43}$$

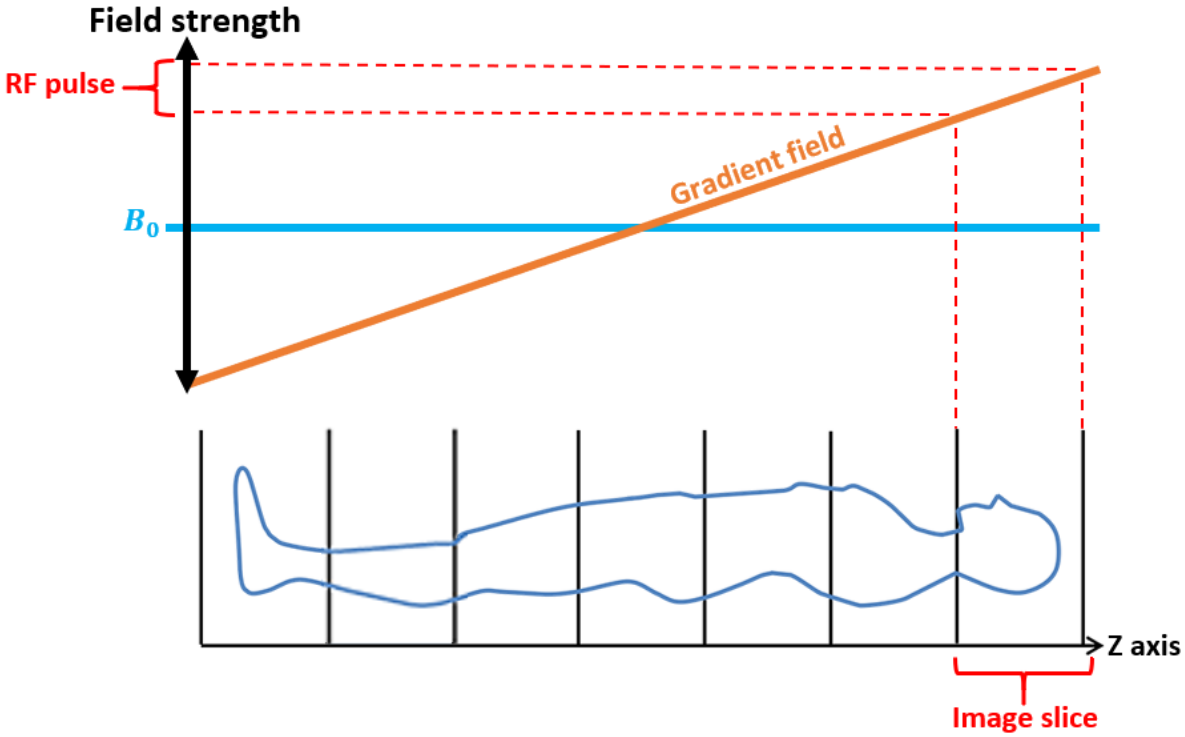

Figure 2.3: Linear gradient field, represented with an orange line, to select a slice. Adapted from [1]

and in the same way, in two dimensions the gradient magnetic fields are

$$\begin{aligned} B_x(x,y) &= xG_x + H_x(x,y), \\ B_y(x,y) &= yG_y + H_y(x,y). \end{aligned} \tag{2.44}$$

The corresponding two-dimensional discrete signal equation for an homogeneous background field and nonlinear gradients is

$$S(k_x,k_y) = \sum_{p=0}^{m-1}\sum_{q=0}^{n-1} M_{xy}(x_p,y_q)\mathrm{e}^{-i\gamma\left((x_pG_x+H_x(x_p,y_q))k_x+(y_qG_y+H_y(x_p,y_q))k_y\right)}\Delta x\Delta y, \quad \begin{aligned} &0 \le k_x \le m-1, \\ &0 \le k_y \le n-1. \end{aligned} \tag{2.45}$$

In the absence of nonlinearities, the terms H_x and H_y disappear and what is left is the linear gradients applied in order to encode the k-space.

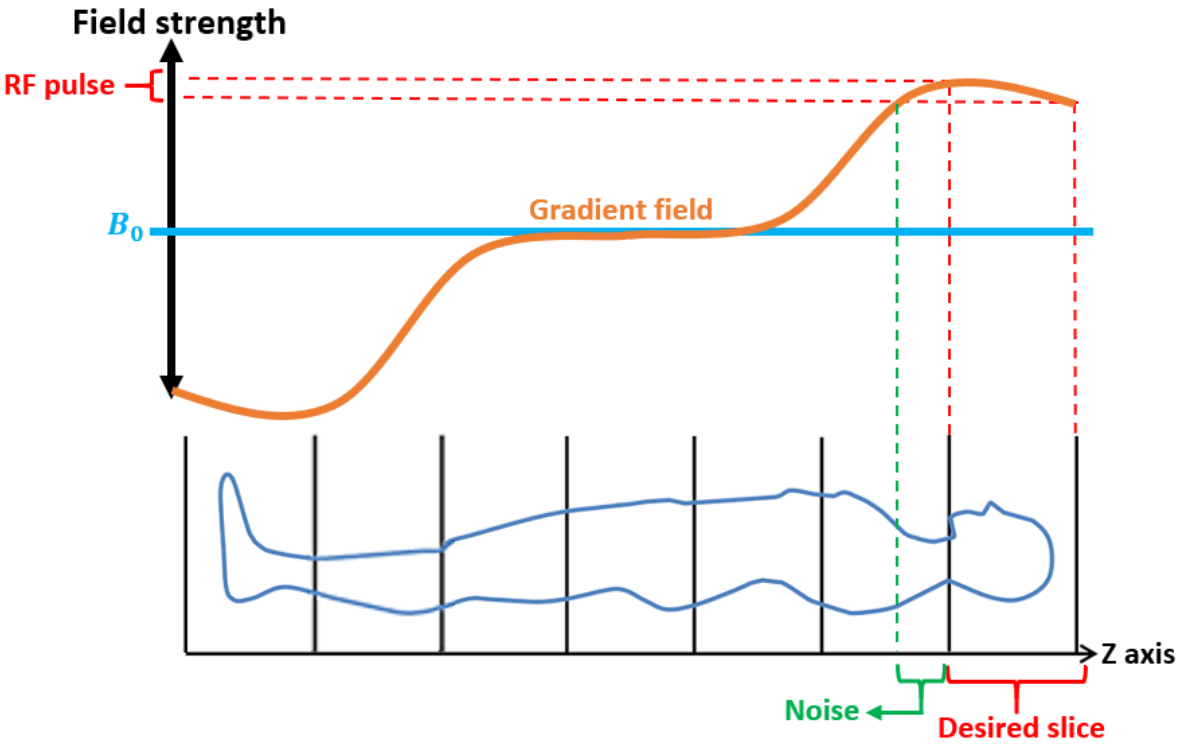

Figure 2.4: Gradient field of a low-field MRI, represented with an orange line, to select a slice. Adapted from [1]

2.5. Inhomogeneous Background Field and Nonlinear Gradients

Now it is assumed that the main field presents inhomogeneities and the gradients are nonlinear. In order to simplify the notation, both nonidealities will be grouped in one space-dependent term, i.e. ΔB_x and ΔB_y. These include the inhomogeneous main field and both nonlinear gradients, along x- and y-direction respectively. This way, we obtain the following nomenclature in both one and two dimensions that will be used along this thesis.

$$S(k_x) = \sum_{p=0}^{N-1} M_x(x_p) \mathrm{e}^{-i\gamma \Delta B_x(x_p) k_x} \Delta x, \quad 0 \leq k_x \leq N-1 \tag{2.46}$$

$$S(k_x, k_y) = \sum_{p=0}^{m-1} \sum_{q=0}^{n-1} M_{xy}(x_p, y_q) \mathrm{e}^{-i\gamma \left((\Delta B_x(x_p, y_q)) k_x + (\Delta B_y(x_p, y_q)) k_y \right)} \Delta x \Delta y, \quad \begin{matrix} 0 \leq k_x \leq m-1, \\ 0 \leq k_y \leq n-1. \end{matrix} \tag{2.47}$$

3

Nonuniform Fourier Transform

The article [30] proposes an algorithm for the nonuniform discrete Fourier transform (NUDFT) based on the fast Fourier transform (FFT) algorithm using a low rank matrix approximation. The advantage of using this method is that it takes few FFT operations, saving computational time. This thesis will be based on the MATLAB software [5] provided by the mentioned article.
This chapter is focused on describing the nonuniform Fourier transform and the algorithm employed by [30]. In the first section 3.1, the nonuniform Fourier transform will be defined. Section 3.2 shows the connection between the nonuniform Fourier transform and the signal model described in the previous chapter 2. In section 3.3, the algorithm for type one nonuniform Fourier transform will be described. The type one nonuniform Fourier transform for the two-dimensional case will be seen in section 3.4. In section 3.5, a brief explanation will be given for the nonuniform Fourier transform of type two. Last section 3.6 corresponds to the two-dimensional nonuniform Fourier transform of type two.

3.1. Introduction

The uniform discrete Fourier transform (DFT) is computed as

$$f_j = \sum_{k=0}^{N-1} c_k \mathrm{e}^{-2\pi i j k/N}, \quad 0 \leq j \leq N-1. \tag{3.1}$$

Where $\mathbf{c} = (c_0, \dots, c_{N-1})^T$ is the $N \times 1$ vector with complex numbers in the space domain and the computed values for the frequency domain are $\mathbf{f} \in \mathbb{C}^{N\times 1}$. The samples j/N are equally spaced in the interval $[0, 1]$ and the frequencies k are integers in the interval $[0, N-1]$. Note that we assume the number of samples in frequency to be equal to the number of samples in the temporal domain, that is N. This is not a necessary condition, but it simplifies the notation.
Three specific cases are described below taking the DFT (equation (3.1)) as the reference.

- When the samples are equally spaced but the frequencies are not integers is known as a type one nonuniform discrete Fourier transform or **NUDFT-I**. The $N \times 1$ vector $\boldsymbol{\omega} = (\omega_0, \dots, \omega_k, \dots, \omega_{N-1})^T$, $\omega_k \in [0, N]$ represents the noninteger frequencies.

$$f_j = \sum_{k=0}^{N-1} c_k \mathrm{e}^{-2\pi i \frac{j}{N} \omega_k}, \quad 0 \leq j \leq N-1. \tag{3.2}$$

- When the samples are not equally spaced and the frequencies are integers is known as a type two nonuniform discrete Fourier transform or **NUDFT-II**. The $N \times 1$ vector $\mathbf{x} = (x_0, \dots, x_j, \dots, x_{N-1})^T$, $x_j \in [0, 1]$ represents the nonequispaced samples.

$$f_j = \sum_{k=0}^{N-1} c_k \mathrm{e}^{-2\pi i x_j k}, \quad 0 \leq j \leq N-1. \tag{3.3}$$

- When the samples are not equally spaced and the frequencies are not integers is known as a type three nonuniform discrete Fourier transform or **NUDFT-III**. The $N \times 1$ vector $\mathbf{x} = (x_0, \dots, x_j, \dots, x_{N-1})^T$, $x_j \in [0, 1]$

represents the nonequispaced samples and the $N \times 1$ vector $\boldsymbol{\omega} = (\omega_0, \dots, \omega_k, \dots, \omega_{N-1})^T$, $\omega_k \in [0, N]$ represents the noninteger frequencies.

$$f_j = \sum_{k=0}^{N-1} c_k \mathrm{e}^{-2\pi i x_j \omega_k}, \quad 0 \leq j \leq N-1. \tag{3.4}$$

3.2. Nonuniform Fourier Transform and the Signal Model

The format of the NUDFT-I matches our signal model described in chapter 2 with an inhomogeneous background field and nonlinear gradients, equation (2.46).
In a type one NUDFT, equation (3.2), the samples are equally spaced and the frequencies are not integers, and this is the case of our signal model.

$$S(k_x) = \sum_{p=0}^{N-1} M_x(x_p) \mathrm{e}^{-i\gamma \Delta B_x(x_p) k_x \Delta x} \quad \Leftrightarrow \quad f_j = \sum_{k=0}^{N-1} c_k \mathrm{e}^{-2\pi i \frac{j}{N} \omega_k}. \tag{3.5}$$

In the signal equation, $\Delta B_x(\mathbf{x})$ is the nonlinear magnetic field, which corresponds to the noninteger frequencies $\boldsymbol{\omega}$ in the NUDFT. The object $M_x(\mathbf{x})$ corresponds to the $\mathbf{c}$ coefficients. The linear k-space samples and the MRI signal $S(\mathbf{k_x})$ correspond to the equispaced samples j/N and the frequencies $\mathbf{f}$, respectively.
In the following chapters, the algorithm for the type one nonuniform Fourier transform will be described for the one and two dimensional cases. To simplify the notation, we will continue with the nomenclature of the NUDFT.

3.3. Type One NUDFT

In a type one NUDFT the samples are equally spaced and the frequencies are not integers. The NUDFT-I, equation (3.2), can be expressed in matrix notation as

$$\mathbf{f} = \tilde{F}_1 \mathbf{c} \quad \left(\tilde{F}_1\right)_{jk} = \mathrm{e}^{-2\pi i \frac{j}{N} \omega_k}, \quad 0 \leq j, k \leq N-1. \tag{3.6}$$

Where the computed values for the frequency domain are $\mathbf{f} \in \mathbb{C}^{N\times 1}$ and $\mathbf{c} \in \mathbb{C}^{N\times 1}$ is the vector with the space domain values. The $N \times 1$ vector $\boldsymbol{\omega} = (\omega_0, \dots, \omega_k, \dots, \omega_{N-1})^T$, $\omega_k \in [0, N]$ represents the noninteger frequencies and j/N are the equispaced samples.
The matrix notation for the uniform DFT is

$$F_{jk} = \mathrm{e}^{-2\pi i jk/N}. \tag{3.7}$$

The Hadamard division[1] of $\tilde{F}_1 \bullet F$ can be approximated by a low rank matrix if the frequencies are near-integers. This means that for a small integer K, there are vectors such that

$$\tilde{F}_1 \bullet F \approx \mathbf{v}_0 \mathbf{u}_0^T + \cdots + \mathbf{v}_{K-1} \mathbf{u}_{K-1}^T, \quad \mathbf{v}_0, \dots, \mathbf{v}_{K-1}, \mathbf{u}_0, \dots, \mathbf{u}_{K-1} \in \mathbb{C}^{N\times 1} \tag{3.8}$$

Where the vectors $\mathbf{v}_0, \dots, \mathbf{v}_{K-1}$ and $\mathbf{u}_0, \dots, \mathbf{u}_{K-1}$ are computed with Chebyshev polynomials using a three-term recurrence relation. Using (3.8) in (3.6)

$$\tilde{F}_1 \mathbf{c} \approx \left((\mathbf{v}_0 \mathbf{u}_0^T + \cdots + \mathbf{v}_{K-1} \mathbf{u}_{K-1}^T) \circ F \right) \mathbf{c} = \sum_{r=0}^{K-1} D_{\mathbf{v}_r} F D_{\mathbf{u}_r} \mathbf{c}, \tag{3.9}$$

where $D_{\mathbf{v}_r}$ is the diagonal matrix with the entries of $\mathbf{v}$ and $D_{\mathbf{u}_r}$ is the diagonal matrix with the entries of $\mathbf{u}$. The computational cost of this operation is K FFTs, i.e. $\mathcal{O}(KN \log N)$.
In the article [30], there are two approaches to compute the algorithm for the NUDFT-II: (1) supposing that the samples are nearly equispaced, where Taylor or Chebyshev expansions are used to calculate the low rank matrix. (2) Assuming arbitrary distributed samples.
This thesis will be based on the second approach, where arbitrarily distributed samples are considered. In the following sections, the explanation given in the mentioned article will be adapted to the nonuniform Fourier transform of type one. For this, equation (3.6) is reformulated as follows

$$\mathbf{f} = \tilde{F}_1 \mathbf{c} \quad \left(\tilde{F}_1\right)_{jk} = \mathrm{e}^{-2\pi i j \omega_k}, \quad 0 \leq j, k \leq N-1. \tag{3.10}$$

Now the vector of frequencies $\boldsymbol{\omega} = (\omega_0, \dots, \omega_k, \dots, \omega_{N-1})^T$, $\omega_k \in [0, 1]$ represents the nonequispaced frequencies and j are the integer samples in the interval $[0, N-1]$.

[1] The Hadamard division or elementwise division is represented by $\bullet$ and the Hadamard product or elementwise product by $\circ$.

3.3.1. Type One NUDFT Assuming Arbitrarily Distributed Frequencies

Since the frequencies are not nearly equispaced, the approximation of equation (3.8) does not hold. In this subsection, the NUDFT-I (equation (3.2)) will be modeled so that this approximation can be applied.
The sequence $s_0, \dots, s_{N-1}$, that takes the values $0, \dots, N$, forms an equispaced grid in which s_k/N is the closest to ω_k.
How the nonequispaced frequencies are assigned can be visualised in figures 3.1 and 3.2. The left figure 3.1 shows equally spaced samples. Therefore, the $\mathbf{s}/N$ sequence to which these samples are assigned is the same as the samples. Nonetheless, figure 3.2 represents nonequispaced samples. These samples are assigned to their closes equispaced point.

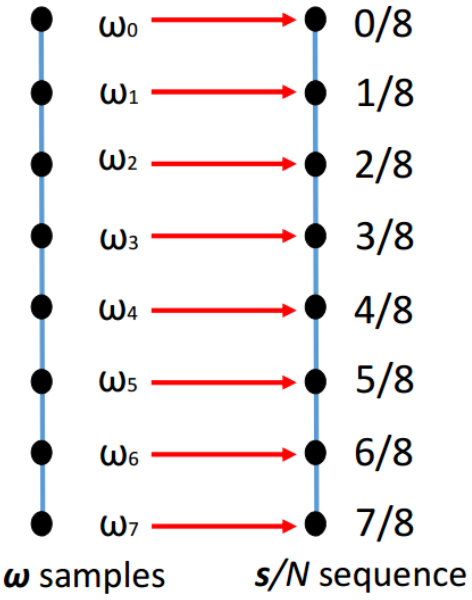

Figure 3.1: Equispaced frequency samples

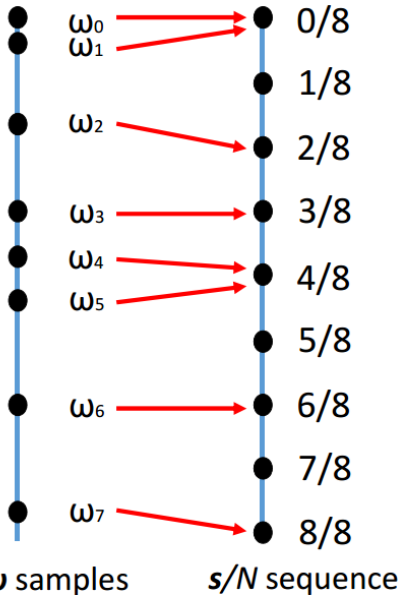

Figure 3.2: Nonequispaced frequency samples assigned to their closest point in the equispaced grid

Each ω_k is distanced from the equispaced node $1/(2N)$ at most, then

$$\left|\omega_k - \frac{s_k}{N}\right| \leq \frac{1}{2N}, \quad 0 \leq k \leq N-1. \tag{3.11}$$

A new sequence $t_0, \dots, t_{N-1}$ must be defined because the uniform DFT does not have a sample at $s_k/N = 1$. Since the complex exponential presents periodicity, i.e. $\mathrm{e}^{-2\pi i N k/N} = \mathrm{e}^{-2\pi i 0 k/N} = 1$, ω_k is reassigned to the equispaced node at 0. The new sequence is given by

$$t_k = \begin{cases} s_k, & 0 \leq s_k \leq N-1, \\ 0, & s_k = N. \end{cases} \tag{3.12}$$

Looking again at figure 3.2, the last frequency sample ω_7 is assigned to $s_7/N = 8/8$ and therefore, its value in the t sequence is $t_7 = 0$.
The nonuniform Fourier matrix (equation (3.10)) can be rewritten as

$$\left(\tilde{F}_1\right)_{jk} = \mathrm{e}^{-2\pi i j \omega_k} = \mathrm{e}^{-2\pi i j(\omega_k - s_k/N)} \mathrm{e}^{-2\pi i \frac{j}{N} s_k} = \mathrm{e}^{-2\pi i j(\omega_k - s_k/N)} \mathrm{e}^{-2\pi i \frac{j}{N} t_k}, \quad 0 \leq j,k \leq N-1. \tag{3.13}$$

The previous equation can be simplified as a Hadamard product of $\mathrm{e}^{-2\pi i j(\omega_k - s_k/N)}$ and the (j, t_k) entry of the uniform Fourier matrix (equation (3.7)). Continuing with equation (3.13)

$$\begin{aligned} \left(\tilde{F}_1\right)_{jk} = A \circ F(:, \mathbf{t}), \quad (F(:,\mathbf{t}))_{jk} = \mathrm{e}^{-2\pi i \frac{j}{N} t_k}, \\ A_{jk} = \mathrm{e}^{-2\pi i j(\omega_k - s_k/N)}, \end{aligned} \tag{3.14}$$

for $0 \leq j,k \leq N-1$ and where $\mathbf{t} = (t_0, \dots, t_{N-1})^T$. Taking the columns indexed by $(t_0, \dots, t_{N-1})$ from the DFT matrix gives $F(:, \mathbf{t})$. An example of how this matrix is constructed can be seen in figure 3.3, when the sequence $\mathbf{t} = [1, 0, 0, 3]$ and the number of samples is $N = 4$.
Another example is represented in figures 3.4 and 3.5. These figures are related to the examples of figures 3.1

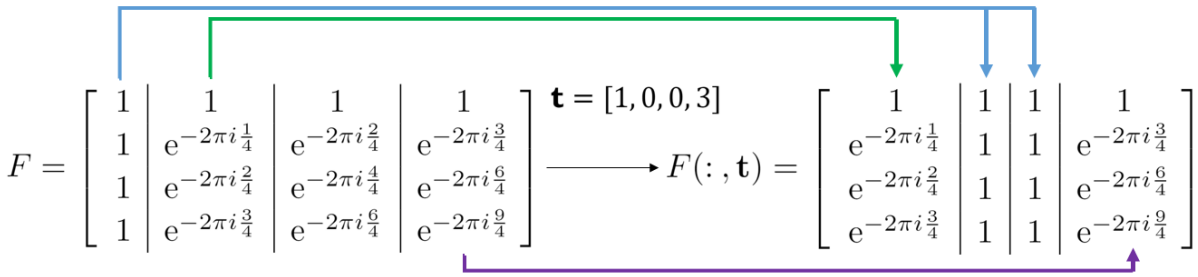

Figure 3.3: Example of the discrete Fourier transform matrix with the columns indexed by the sequence $\mathbf{t} = [1, 0, 0, 3]$ when the number of samples is $N = 4$

and 3.2.
The first figure 3.4 shows the discrete Fourier transform matrix created from the **s** sequence from 3.1. Since this sequence is ordered, the corresponding $F(:, \mathbf{t})$ matrix corresponds to the conventional DFT matrix. Each colour represents a different frequency, the real part is represented by a solid line, and the imaginary part by a dashed line.
Regarding figure 3.5, it represents the DFT matrix with its columns permuted according to the **t** sequence taken from the $\mathbf{s}/N$ sequence of figure 3.2. Note that this $F(:, \mathbf{t})$ matrix has to be multiplied elementwise by the A matrix, equation 3.14, in order to properly perform the nonuniform Fourier transform. As the previous figure 3.4, each colour represents a different frequency, the real part is represented by a solid line, and the imaginary part by a dashed line.

Since $N(\omega_k - s_k/N) \in [-1/2, 1/2]$ and $j/N \in [0, 1]$, the matrix A can be approximated by a low rank matrix, i.e. $A \approx A_K$, and $(A \circ F(:, \mathbf{t}))\mathbf{c}$ can be obtained using equation (3.9), i.e.

$$\tilde{F}_1\mathbf{c} = (A \circ F(:, \mathbf{t}))\mathbf{c} \approx (A_K \circ F(:, \mathbf{t}))\mathbf{c} = \sum_{r=0}^{K-1} D_{\mathbf{v}_r} F(:, \mathbf{t}) D_{\mathbf{u}_r}\mathbf{c}, \tag{3.15}$$

The next step is to compute the low rank matrix approximation, which is done via bivariate Chebyshev expansions of the function e^{-ixy}. The integer K can be selected using Table 1 from [30] or also using the following equation

$$K = \max\left\{3, \left\lceil 5\delta \mathrm{e}^{W(\log(140/\epsilon)/(5\delta))}\right\rceil\right\}, \tag{3.16}$$

in which $W(x)$ is the Lambert-W function, ϵ represents the working precision, such that $||A - A_K||_{\max} \leq \epsilon$. The bigger K is, the more similar the approximation matrix to A is, and therefore, the working precision is smaller. The perturbation parameter is represented by δ, i.e. the maximum distance between the nonuniform frequencies ω_k and the equispaced grid s_k which is at most $1/2$

$$\delta = \max\{|N\omega_k - s_k|\} \leq 1/2, \quad 0 \leq k \leq N - 1. \tag{3.17}$$

Taking the asymptotic approximation in equation (3.16) of $W(x)$ as $x \to \infty$, gives the following equation

$$K = \mathcal{O}\left(\frac{\log(1/\epsilon)}{\log\log(1/\epsilon)}\right), \tag{3.18}$$

when $\epsilon \to 0$ and therefore, equation (3.15) can be computed in $\mathcal{O}(N \log N \log(1/\epsilon)/\log\log(1/\epsilon))$ operations. The integer K is at most 16 with double precision ($\epsilon = 2.22\mathrm{e}{-16}$).

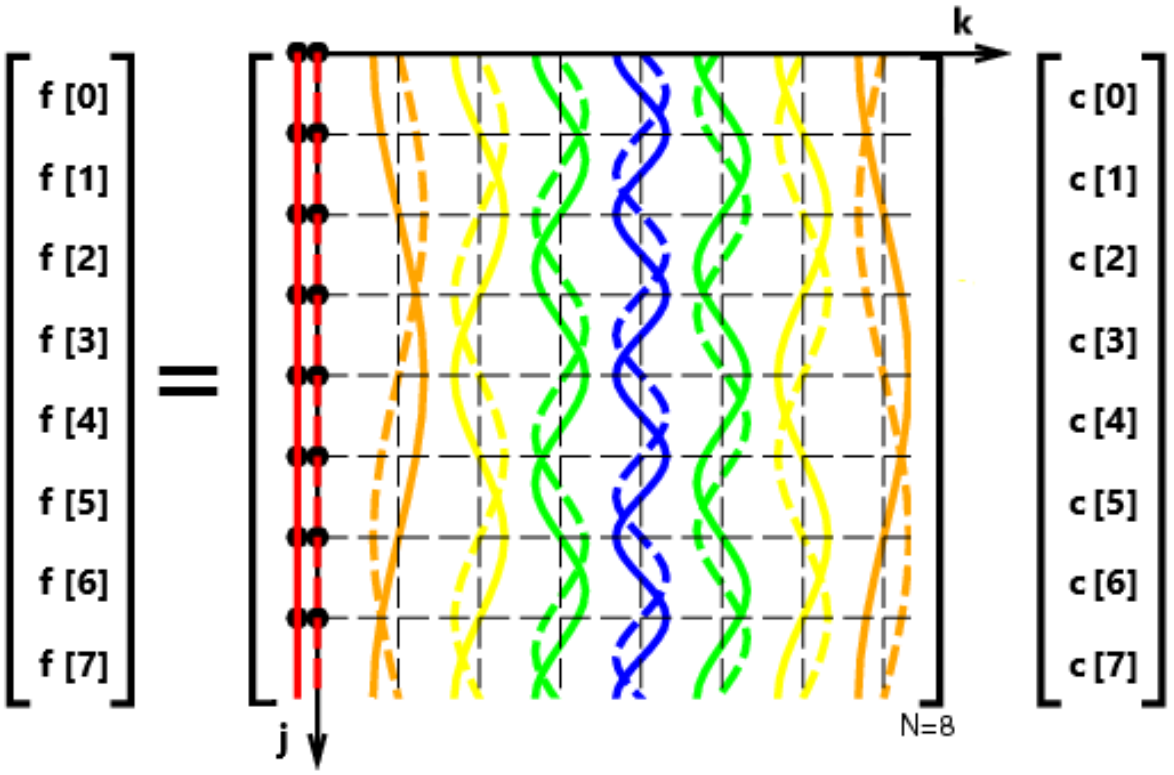

Figure 3.4: Discrete Fourier transform matrix created from $\mathbf{s}/N$ sequence of figure 3.1. Adapted from [36]

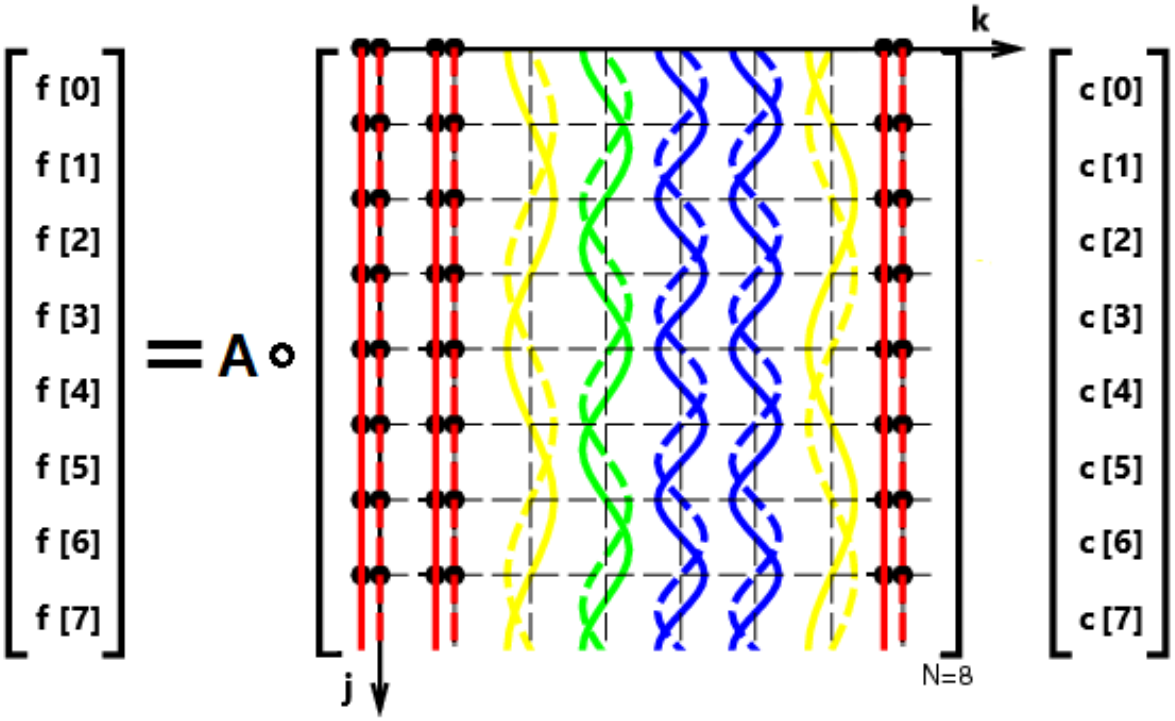

Figure 3.5: Discrete Fourier transform matrix with permuted columns created from $\mathbf{s}/N$ sequence of figure 3.2. Note that this matrix $F(:, \mathbf{t})$ is multiplied elementwise by the A matrix. Adapted from [36]

3.4. Two-dimensional Type One NUDFT

The two-dimensional uniform discrete Fourier transform is computed as

$$f_{j_1 j_2} = \sum_{k=0}^{N-1} c_k \mathrm{e}^{-2\pi i\left(\frac{j_1}{m}+\frac{j_2}{n}\right)k}, \quad \begin{matrix} 0 \le j_1 \le m-1, \\ 0 \le j_2 \le n-1. \end{matrix} \tag{3.19}$$

In which the total number of samples is $N = mn$, the frequency values are $f \in \mathbb{C}^{m\times n}$ and the Fourier coefficients in the space domain are $\mathbf{c} \in \mathbb{C}^{mn\times 1}$. The uniform 2D FFT costs $\mathcal{O}(mn(\log m + \log n))$ operations.
Based on the article [30], the two-dimensional nonuniform Fourier transform of type one is defined as

$$f_{j_1 j_2} = \sum_{k=0}^{N-1} c_k \mathrm{e}^{-2\pi i(j_1\omega_k + j_2\phi_k)}, \quad \begin{matrix} 0 \le j_1 \le m-1, \\ 0 \le j_2 \le n-1. \end{matrix} \tag{3.20}$$

The vector $\mathbf{c} \in \mathbb{C}^{mn\times 1}$ contains the Fourier coefficients in the space domain, the matrix $f \in \mathbb{C}^{m\times n}$ are the frequency values and $\boldsymbol{\omega}$, $\boldsymbol{\phi}$ are the nonequispaced frequencies where $\boldsymbol{\omega} = (\omega_0, \dots, \omega_k, \dots, \omega_{N-1})^T$, $\omega_k \in [0,1]$ and $\boldsymbol{\phi} = (\phi_0, \dots, \phi_k, \dots, \phi_{N-1})^T$, $\phi_k \in [0,1]$. The samples j_1 and j_2 are integers.
Although the previous equation takes $\mathcal{O}(Nmn)$ operations, this number can be reduced using the ideas of the approximation algorithm that the article [30] proposes.
Assigning the nonequispaced frequencies to the closest uniform spaced frequencies, similar to the procedure of subsection 3.3.1, equation (3.20) can be simplified to[2]

$$f_{j_1 j_2} = \sum_{k=0}^{N-1} c_k A^{\omega}_{j_1 k} A^{\phi}_{j_2 k} \mathrm{e}^{-2\pi i(j_1 t^{\omega}_k/m + j_2 t^{\phi}_k/n)}, \quad \begin{matrix} A^{\omega}_{j_1 k} = \mathrm{e}^{-2\pi i j_1(\omega_k - s^{\omega}_k/m)}, \\ A^{\phi}_{j_2 k} = \mathrm{e}^{-2\pi i j_2(\phi_k - s^{\phi}_k/n)}. \end{matrix} \tag{3.21}$$

Note that $\mathrm{e}^{-2\pi i(j_1 t^{\omega}_k/m + j_2 t^{\phi}_k/n)}$ is related to the two-dimesional uniform Fourier transform. Expressing the previous equation (3.21) in matrix form gives

$$f = (A^{\omega} \circ F)\mathrm{diag}(\mathbf{c})(A^{\phi} \circ F)^T \tag{3.22}$$

Where $\circ$ represent the Hadamard product or elementwise product, $\mathrm{diag}(c)$ creates a diagonal matrix out of the column vector c and F represents the Fourier matrix.
Since $m|\omega_k - s^{\omega}_k/m| \le 1/2$, $n|\phi_k - s^{\phi}_k/n| \le 1/2$, $j_1/m \in [0,1]$ and $j_2/n \in [0,1]$, both $A^{\omega} \in \mathbb{C}^{m\times N}$ and $A^{\phi} \in \mathbb{C}^{n\times N}$ matrices can be approximated by a low rank matrix as

$$\begin{aligned} A^{\omega} &\approx \mathbf{v}^{\omega}_0 (\mathbf{u}^{\omega}_0)^T + \cdots + \mathbf{v}^{\omega}_{K_1-1} (\mathbf{u}^{\omega}_{K_1-1})^T \\ A^{\phi} &\approx \mathbf{v}^{\phi}_0 (\mathbf{u}^{\phi}_0)^T + \cdots + \mathbf{v}^{\phi}_{K_2-1} (\mathbf{u}^{\phi}_{K_2-1})^T \end{aligned} \tag{3.23}$$

Substituting equation (3.23) into (3.21) and using

$$A \circ F \approx A_K \circ F = (\mathbf{v}\mathbf{u}^T) \circ F = D_{\mathbf{v}} F D_{\mathbf{u}}, \tag{3.24}$$

gives

$$f_{j_1 j_2} = \sum_{r_1=0}^{K_1-1} \sum_{r_2=0}^{K_2-1} D_{\mathbf{v}^{\omega}_{r_1}} F_m I(:, t^{\omega}_k) D_{\mathbf{u}^{\omega}_{r_1}} \mathrm{diag}(\mathbf{c}) D_{\mathbf{u}^{\phi}_{r_2}} I(t^{\phi}_k, :) F^T_n D_{\mathbf{v}^{\phi}_{r_2}}. \tag{3.25}$$

There are $K_1 K_2$ terms in the previous equation (3.25). Each requires an $m \times n$ two-dimensional fast Fourier transform. Besides, each term adds $m \times n$ matrices. Therefore, the total number of operations is $\mathcal{O}(K_1 K_2 mn(\log m + \log n) + mn)$.

3.5. Type Two NUDFT

The type two nonuniform Fourier transform is explained in this section because it will be used in the Conjugate Gradient to retrieved the object in chapter 7.
In a NUDFT-II, equation (3.3), the samples are nonequispaced and the frequencies are integers. Equation 3.3 can be expressed in matrix form in a similar way as equation (3.6) as follows

$$\mathbf{f} = \tilde{F}_2 \mathbf{c} \quad \left(\tilde{F}_2\right)_{jk} = \mathrm{e}^{-2\pi i x_j k}, \quad 0 \le j,k \le N-1. \tag{3.26}$$

[2] See section 4 of [30] for more details

Where the computed values for the frequency domain are $\mathbf{f} \in \mathbb{C}^{N\times 1}$ and $\mathbf{c} \in \mathbb{C}^{N\times 1}$ is the vector with the values in the space domain. The $N \times 1$ vector $\mathbf{x} = (x_0, \dots, x_j, \dots, x_{N-1})^T$, $x_j \in [0, 1]$ represents the nonequispaced samples and $k \in [0, N]$ are the integer frequencies.
The nonuniform type two matrix can be expressed as the nonuniform type one matrix

$$(\tilde{F}_1)_{jk} = \mathrm{e}^{-2\pi i \frac{j}{N}\omega_k} = \mathrm{e}^{-2\pi i \frac{\omega_k}{N} j} = (\tilde{F}_2)_{kj}, \quad 0 \leq j, k \leq N-1. \tag{3.27}$$

Therefore, $\tilde{F}_2 = \tilde{F}_1^T$. The method explained in subsection 3.3.1 works similarly for a nonuniform Fourier transform of type two and the computational costs for NUFFT-II are $KN \log N$.

3.6. Two-dimensional Type Two NUDFT

The type two nonuniform Fourier transform is explained in this section because it will be used in the Conjugate Gradient to retrieved the object in chapter 9.
The nonuniform 2D Fourier transform of type two presents nonequispaced samples and it is computed as

$$f = \mathrm{diag}\left((A^y \circ F)c(A^x \circ F)^T\right). \tag{3.28}$$

Where $\circ$ represent the Hadamard product or elementwise product, $\mathrm{diag}(x)$ takes the vector in the diagonal of the x matrix and F represents the Fourier matrix. The matrices A^x and A^y are computed in a similar way as equation (3.21).
A low rank approximation matrix can be applied to equation (3.28) giving

$$f_j = \sum_{r_1=0}^{K_1-1} \sum_{r_2=0}^{K_2-1} D_{\mathbf{u}^y_{r_1}} I(t^y_j, :) F_m D_{\mathbf{v}^y_{r_1}} c\, D_{\mathbf{v}^x_{r_2}} F_n^T I(:, t^x_j) D_{\mathbf{u}^x_{r_2}}. \tag{3.29}$$

This operations is similar to the one presented for the type one case in equation (3.25). Recall that a nonuniform Fourier transform of type one is equivalent to transpose a type two (see equation (3.27)). Therefore, the computational cost of the previous equation (3.29) is $\mathcal{O}(K_1 K_2 mn(\log m + \log n) + mn)$. The reader is referred to [30] for further explanations.

II

Methodology

4

Procedure

In this chapter, the methodology used in the chapters 6, 7 and 8 for the one and two dimensional case respectively will be described. Moreover, the algorithms that will be used to obtain these results will be explained.
The chapter begins in section 4.1 with an introduction and a description of the problem, and in section 4.2, the forward and inverse problem will be explained.

4.1. Introduction

In this section, the signal model for one and two dimensions described in chapter 2 will be represented with the nonuniform nomenclature of chapter 3.

One dimension Recall that the signal model of the low-field MRI described in chapter 2 is expressed as

$$S(k_x) = \sum_{p=0}^{N-1} M_x(x_p) \mathrm{e}^{-i\gamma \Delta B_x(x_p) k_x} \Delta x, \quad 0 \leq k_x \leq N-1 \tag{4.1}$$

For notational convenience, ΔB_x represents both background field inhomogeneities and nonlinear gradients grouped, as explained in section 2.5.
Expressing the object in matrix form as in equation (3.10)

$$\mathbf{S} = \tilde{F}_1 \mathbf{M}_x \quad \left(\tilde{F}_1\right)_{k_x p} = \mathrm{e}^{-i\gamma k_x \Delta B_x(x_p)}, \quad 0 \leq p, k_x \leq N-1. \tag{4.2}$$

Where $\mathbf{S} \in \mathbb{C}^{N\times 1}$ is the MRI signal, $\mathbf{M}_x \in \mathbb{Q}^{N\times 1}$ is the transverse magnetisation or the desired object, the nonuniform magnetic field $\Delta B_x(x_p) \in [0,1]$ and the integer k-space samples $k_x \in [0, N-1]$. The gyromagnetic ratio is represented by γ.
Since the main background magnetic field is not homogeneous and also other nonlinear effects in the gradients exist, the total field $\Delta B_x(\mathbf{x})$ is not uniform. Therefore, the samples in the k-space are distorted and the object cannot be retrieved using the inverse operation. In order to retrieve the object, an iterative solver must be applied.

Two dimensions In a similar way as in one dimension, the two-dimensional discrete signal equation of a low-field MRI is expressed as follows

$$S(k_x, k_y) = \sum_{p=0}^{m-1} \sum_{q=0}^{n-1} M_{xy}(x_p, y_q) \mathrm{e}^{-i\gamma\left(\Delta B_x(x_p,y_q) k_x + \Delta B_y(x_p,y_q) k_y\right)} \Delta x \Delta y, \quad \begin{matrix} 0 \leq k_x \leq m-1, \\ 0 \leq k_y \leq n-1. \end{matrix} \tag{4.3}$$

Note that the previous equation represents both the background field inhomogeneities and the nonlinear gradients along x- and y-direction grouped in ΔB_x and ΔB_y respectively.
Matching equation (4.3) to the nonuniform formula in equation (3.20) gives

$$\begin{aligned} S(k_x, k_y) &= \sum_{p=0}^{N-1} M_{xy}(r_p) A^x_{k_x p} A^y_{k_y p} \mathrm{e}^{-i\gamma\left(k_x t^x_p/n + k_y t^y_p/m\right)} \Delta x \Delta y, \\ A^x_{k_x p} &= \mathrm{e}^{-i\gamma k_x (\Delta B_x(r_p) - s^x_p/n)}, \quad A_{k_y p} = \mathrm{e}^{-i\gamma k_y (\Delta B_y(r_p) - s^y_p/m)}. \end{aligned} \tag{4.4}$$

Where $0 \leq p \leq N-1$ and $N = mn$, (s_p^x, s_p^y) is the closest point from an $m \times n$ equispaced grid to $(\Delta B_x(r_p), \Delta B_y(r_p))$. The sequence $(t_0^x, t_0^y), \ldots, (t_{n-1}^x, t_{m-1}^y)$ is equal to the sequence $(s_0^x, s_0^y), \ldots, (s_{n-1}^x, s_{m-1}^y)$ but assigning $t_p^x = 0$ or $t_p^y = 0$ when $s_p^x = n$ or $s_p^y = m$ respectively (see section 3.4 in chapter 3 for more details). The transverse magnetisation of the desired object at the r_p position is $M_{xy}(r_p)$ and $S(k_x, k_y)$ is the received signal in a low-field MRI at the (k_x, k_y) k-space point. The size of the pixel is $\Delta x \Delta y$ and γ is the gyromagnetic ratio.
Note that in this chapter, the sequences s and t, the fields $\Delta B_x(x, y)$ and $\Delta B_y(x, y)$ and the object $M_{xy}(x, y)$ are $N \times 1$ vectors, where $N = mn$. Whereas the received MRI signal $S(k_x, k_y)$ and the k-space samples are $m \times n$ matrices.
The two-dimensional object cannot be retrieved using the inverse operation since the frequency samples are nonlinear. Instead, an iterative solver can be used to solve the problem.

4.2. Problem Statement

In summarised form, the whole process consists in placing an object in a magnetic field to create an MRI signal and then try to retrieve the object from this signal. In other words, first a forward problem is performed to obtain the MRI signal. Then, using this signal, the solution to the inverse problem is found. This solution is the object retrieved and it will be compared to the original object in the results of chapters 6, 7, 8 and 9.
How the forward and inverse problems are implemented is explained in subsections 4.2.1 and 4.2.2 respectively.

4.2.1. Forward Problem

The object and the nonuniform magnetic field are created to generate the MRI signal. Several experiments with different fields and objects were carried out in order to analyse a variety of results in one and two dimensions. Some of them will be shown in the following chapters.

One dimension For the one dimensional case, the full nonuniform Fourier matrix $\tilde{F}_1$ is generated using the aforementioned field. This is done by multiplying the column vector of k-space samples k_x by the row vector with the values of the magnetic field ΔB_x at the x positions. Then, this matrix is multiplied by the $-i\gamma$ constant and the exponential of the result is taken. The MRI signal is generated by multiplying the full nonuniform Fourier matrix by the object sampled at the x positions, i.e. $\tilde{F}_1 M_x(\mathbf{x})$. The forward problem is summarised in the block diagram of figure 4.1 for one dimension.

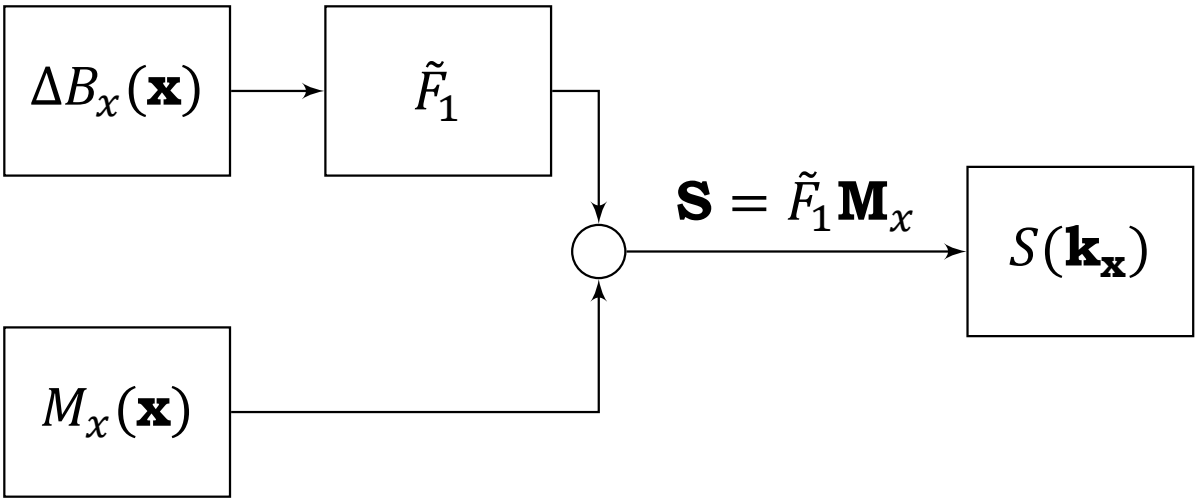

Figure 4.1: Scheme of the forward problem in 1D, i.e. the procedure to generate the MRI signal $S(\mathbf{k_x})$ from the gradient field along x-direction $\Delta B_x(\mathbf{x})$ and the object $M_x(\mathbf{x})$

Two dimensions Regarding the two-dimensional case, the 2D nonuniform Fourier transform is applied multiplying the object by two nonuniform Fourier matrices as

```
Fy = exp(-i*gamma*(0:m-1)'*By(:)');
Fx = exp(-i*gamma*(0:n-1)'*Bx(:)');
S = Fy*diag(M_xy(:))*Fx.';
```

Where the matrices `Bx` and `By` correspond to the magnetic fields applied to the object, ΔB_x and ΔB_y respectively. The matrix `S` is the received signal and the matrix `M_xy` is the transverse magnetisation of the object. The variable `gamma` is the gyromagnetic ratio. The forward problem is represented in the figure 4.2 for two dimensions.

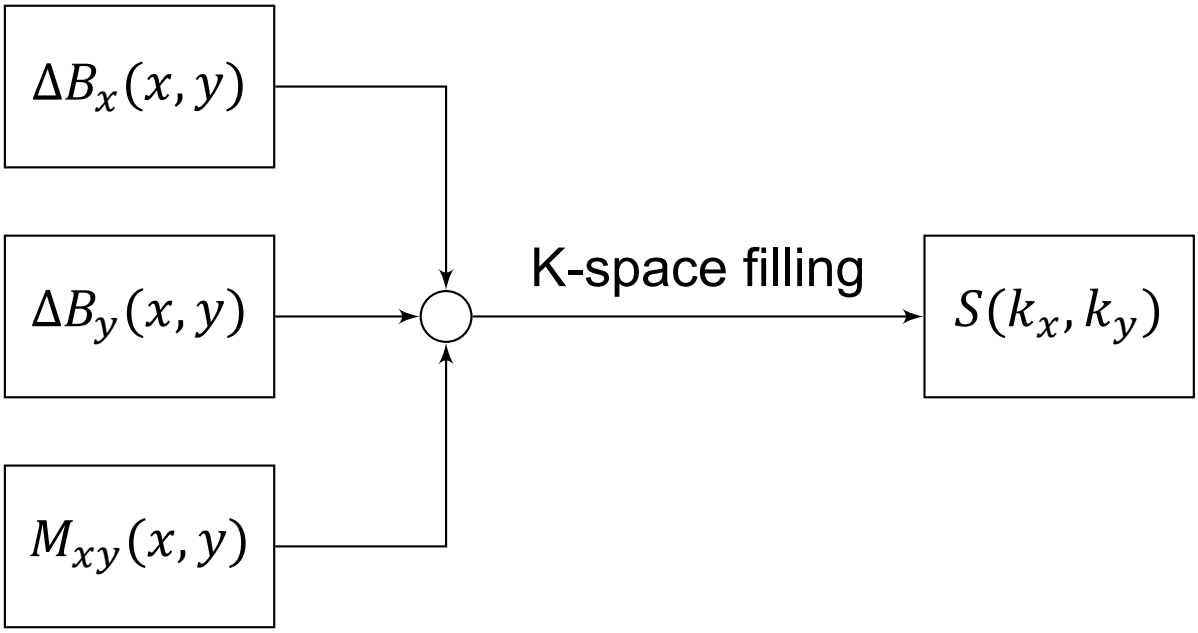

Figure 4.2: Scheme of the forward problem in 2D, i.e. the procedure to generate the two-dimensional MRI signal $S(k_x, k_y)$ from the gradient field along x-direction $\Delta B_x(x, y)$, the gradient field along y-direction $\Delta B_y(x, y)$ and the object $M_{xy}(x, y)$

4.2.2. Inverse Problem

Once the MRI signal is generated, the aim is to retrieve the object using an iterative solver and the *nufft()* algorithm from Chebfun [5].

One dimension The original problem is stated as follows

$$S = \tilde{F}_1 M_x \tag{4.5}$$

Where we want to find the solution for M_x. In order to save computational time, the approximation of the nonuniform Fourier algorithm *nufft()* described in chapter 3 is applied

$$S = (A_K \circ F(:, \mathbf{t}))M_x \tag{4.6}$$

In each iteration of the solver, K FFTs would be performed. Therefore, the total time of the algorithm would be roughly $\mathcal{O}(RKN \log N)$. Where R is the number of iterations, K is the rank of the approximation matrix, and N is the number of samples.
The article [30] uses the Conjugate Gradient (CG) method to solve equation (4.6). To apply the CG method, the system of equations must be linear and $\tilde{F}_1$ must be a positive definite matrix (symmetric with positive eigenvalues). This is not the case and therefore, equation (4.5) is modified in order to obtain a positive definite matrix. This can be done by multiplying equation (4.5) from the left by $\tilde{F}_1^*$ and obtaining the matrix $\tilde{F}_1^*\tilde{F}_1$ which is definite positive. Nonetheless, the article [30] takes advantage that the matrix $\tilde{F}_1\tilde{F}_1^*$ is Toeplitz and it can be computed using a fast Toeplitz multiply saving computational time. How to obtain $\tilde{F}_1\tilde{F}_1^*$ is explained below.
The nonuniform Fourier matrix $\tilde{F}_1$ presents linearly independent rows and therefore, its pseudo-inverse is defined as

$$\tilde{F}_1^{-1} = \tilde{F}_1^*(\tilde{F}_1\tilde{F}_1^*)^{-1}. \tag{4.7}$$

Where $\tilde{F}_1\tilde{F}_1^*$ is a matrix with constant diagonal entries, i.e. a Toeplitz matrix, and it can be computed using a fast Toeplitz multiply. The fast Toeplitz multiply costs one direct FFT and one inverse FFT of size $2N$. Constructing the Toeplitz matrix costs one nonuniform FFT of type one. This will be detailed in section 5.1.
Inserting the inverse nonuniform Fourier matrix in the signal equation

$$\begin{aligned} S &= \tilde{F}_1 M_x, \\ \tilde{F}_1^{-1} S &= M_x, \end{aligned} \tag{4.8}$$

and applying the pseudo-inverse (equation (4.7)) to the previous equation (4.8) gives

$$\begin{aligned} \tilde{F}_1^*(\tilde{F}_1\tilde{F}_1^*)^{-1} S &= M_x, \\ (\tilde{F}_1\tilde{F}_1^*)^{-1} S &= (\tilde{F}_1^*)^{-1} M_x. \end{aligned} \tag{4.9}$$

Simplifying the notation with $M'_x = (\tilde{F}_1^*)^{-1} M_x$

$$(\tilde{F}_1 \tilde{F}_1^*)^{-1} S = M'_x, \tag{4.10}$$

and writing the equation with the format of the CG gives

$$S = (\tilde{F}_1 \tilde{F}_1^*) M'_x. \tag{4.11}$$

The Conjugate Gradient method can be used in the equation (4.11) since it is a linear system with a positive definite matrix. In order to retrieve the object after solving M'_x, the conjugate of a nonuniform Fourier transform is applied, i.e. $M_x = \tilde{F}_1^* M'_x$, which can be done by applying a NUFFT-II. This will be detailed in section 5.1.
Regarding the total number of operations that this process takes is summarised in the following bullet points.

- One NUFFT-I to create the Toeplitz matrix $\tilde{F}_1 \tilde{F}_1^*$, i.e. $\mathcal{O}(KN \log N)$.
- Two FFTs of size $2N$ per iteration of the CG to solve $S = (\tilde{F}_1 \tilde{F}_1^*) M'_x$ using the fast Toeplitz product, i.e. $\mathcal{O}(2R(2N) \log(2N))$.
- One NUFFT-II to retrieve the object from M'_x, i.e. $\mathcal{O}(KN \log N)$.

The inverse problem is represented in the figure 4.3.

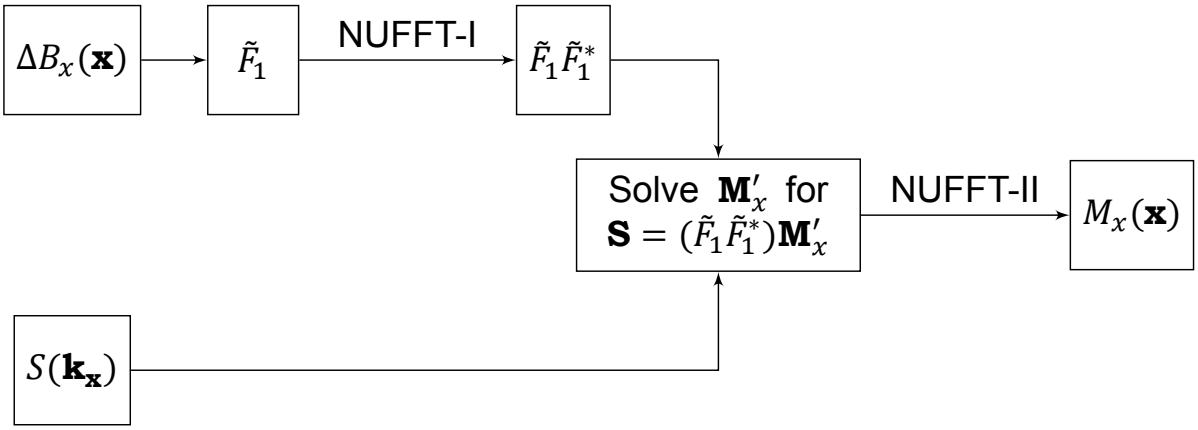

Figure 4.3: Scheme of the inverse problem in 1D, i.e. the procedure to retrieve the object $M_x(\mathbf{x})$

Two dimensions The procedure of the inverse problem for two dimensions is very similar to the one dimension. The problem is stated below

$$S = \tilde{F}_1^y \text{diag}(\mathbf{M}_{xy}) \tilde{F}_1^{x\,T}. \tag{4.12}$$

Where S is an $m \times n$ matrix which represents the signal received, $\text{diag}(\mathbf{M}_{xy})$ is an $mn \times mn$ diagonal matrix with the object as a column vector in the diagonal. The matrices $\tilde{F}_1^x$ and $\tilde{F}_1^y$ multiplying from the right and left sides of the object are analogous to perform the 2D nonuniform Fourier Transform. The aim is to find a solution for the desired object M_{xy}.
The previous equation (4.12) can be also expressed as

$$\mathbf{S} = \left(\tilde{F}_1^x \otimes \tilde{F}_1^y\right) \mathbf{M}_{xy}. \tag{4.13}$$

Now both the signal and the object are column vectors of size $mn \times 1$. The symbol $\otimes$ represents the Kronecker product. This system cannot be solved using the Conjugate Gradient method since the matrix $\left(\tilde{F}_1^x \otimes \tilde{F}_1^y\right)$ is not positive definite. Therefore, equation (4.12) is modified below.

$$\begin{aligned} &S = \tilde{F}_1^y \text{diag}(\mathbf{M}_{xy}) \tilde{F}_1^{x\,T}, \\ &(\tilde{F}_1^y)^{-1} S (\tilde{F}_1^{x\,T})^{-1} = \text{diag}(\mathbf{M}_{xy}). \end{aligned} \tag{4.14}$$

Using equation (4.7) gives

$$\begin{aligned} &\tilde{F}_1^{y\,*} (\tilde{F}_1^y \tilde{F}_1^{y\,*})^{-1} S (\tilde{F}_1^{x\,*} \tilde{F}_1^x)^{-1} \tilde{F}_1^{x\,*} = \text{diag}(\mathbf{M}_{xy}), \\ &(\tilde{F}_1^y \tilde{F}_1^{y\,*})^{-1} S (\tilde{F}_1^{x\,*} \tilde{F}_1^x)^{-1} = (\tilde{F}_1^{y\,*})^{-1} \text{diag}(\mathbf{M}_{xy}) (\tilde{F}_1^{x\,*})^{-1}. \end{aligned} \tag{4.15}$$

And to simplify the notation, $M'_{xy} = (\tilde{F}_1^{y\,*})^{-1} \text{diag}(\mathbf{M}_{xy}) (\tilde{F}_1^{x\,*})^{-1}$.

$$\begin{aligned} &(\tilde{F}_1^y \tilde{F}_1^{y\,*})^{-1} S (\tilde{F}_1^{x\,*} \tilde{F}_1^x)^{-1} = M'_{xy}, \\ &S = (\tilde{F}_1^y \tilde{F}_1^{y\,*}) M'_{xy} (\tilde{F}_1^{x\,*} \tilde{F}_1^x). \end{aligned} \tag{4.16}$$

And converting the matrices to vectors leads to

$$\mathbf{S} = \left((\tilde{F}_1^{x\,*}\tilde{F}_1^{x})^T \otimes (\tilde{F}_1^{y}\tilde{F}_1^{y\,*})\right)\mathbf{M}'_{xy}. \tag{4.17}$$

In which the matrix $(\tilde{F}_1^{x\,*}\tilde{F}_1^{x})^T \otimes (\tilde{F}_1^{y}\tilde{F}_1^{y\,*})$ is symmetric with positive eigenvalues. Therefore, $\mathbf{M}'_{xy}$ can be solved using the Conjugate Gradient method. However, this matrix is not Toeplitz and it cannot be computed using a fast Toeplitz multiply, as it was done in the one-dimensional case.
The object can be finally retrieved using a 2D NUFFT-II on the solution $\mathbf{M}'_{xy}$. This will be detailed in section 5.1.
The number of operations is summarised in the the following bullet points.

- One 2D NUFFT-I to obtain the column and row of the Toeplitz matrices $(\tilde{F}_1^{y}\tilde{F}_1^{y\,*})$ and $(\tilde{F}_1^{x\,*}\tilde{F}_1^{x})$, respectively. This costs $\mathcal{O}(K^xK^ymn(\log m + \log n) + mn)$.
- Construct the two Toeplitz matrices and perform the Kronecker product.
- A Matrix-vector product per iteration of the CG to solve M'_{xy}.
- One 2D NUFFT-II to retrieve the object from M'_{xy}, i.e. $\mathcal{O}(K^xK^ymn(\log m + \log n) + mn)$.

The inverse problem is represented in the figure 4.4.

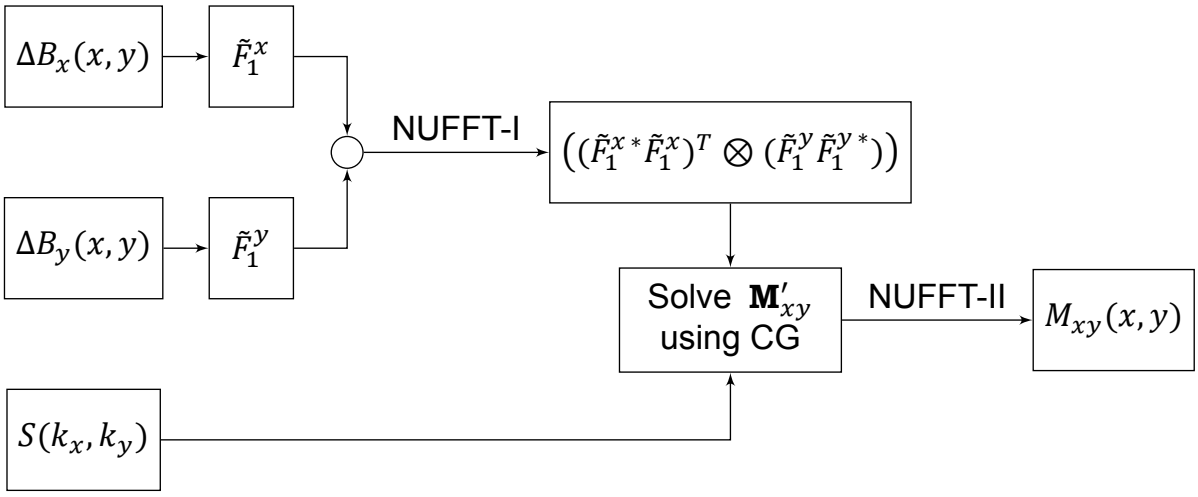

Figure 4.4: Scheme of the inverse problem in 2D, i.e. the procedure to retrieve the object $M_{xy}(\mathbf{x},\mathbf{y})$

5

Algorithms

The algorithms used to obtain the results from chapter 6, 7, 8 and 9 are detailed in this chapter.
First, the Conjugate Gradient (CG) is presented in section 5.1 and second, the nonuniform fast Fourier transform (NUFFT) is presented in section 5.2.

5.1. Conjugate Gradient Method

The Conjugate Gradient (CG) method [31] solves sparse linear systems of the form

$$\mathbf{A}\mathbf{x} = \mathbf{b}. \tag{5.1}$$

Where $\mathbf{A}$ is a symmetric matrix with positive eigenvalues. This guarantees a unique solution $\mathbf{x}_*$. The CG finds the optimal point by minimising the quadratic function

$$\underset{\mathbf{x}}{\text{minimise}} \quad f(\mathbf{x}) = \mathbf{x}^T\mathbf{A}\mathbf{x} - \mathbf{b}^T\mathbf{x} + c \tag{5.2}$$

in which the solution is $\mathbf{A}\mathbf{x} = \mathbf{b}$. The algorithm looks for the minimum by taking steps in the direction using conjugate gradients and minimising each step with a line search. Each new search direction is A-orthogonal to the previous directions, i.e.

$$d_i^T\mathbf{A}d_j = 0, \quad \text{for } i \neq j. \tag{5.3}$$

The Conjugate Gradient method can be seen in algorithm 1.

Algorithm 1 Conjugate Gradient

Starting point x_0
Initialised $d_0 = r_0 = b - Ax_0$
for $i = 0, 1, \ldots$ **do**
  Find step size $\alpha_i = \frac{r_i^T r_i}{d_i^T A d_i}$
  Update the solution $x_{i+1} = x_i + \alpha_i d_i$
  Update the residual $r_{i+1} = r_i - \alpha_i A d_i$
  $\beta_{i+1} = \frac{r_{i+1}^T r_{i+1}}{r_{i+1}^T r_{i+1}}$
  Update search direction $d_{i+1} = r_{i+1} + \beta_{i+1} d_i$
end for

The search directions $\mathbf{d}_i$ are built by conjugation of the residual. The algorithm initialises by setting the search direction and the residual to $\mathbf{d}_0 = \mathbf{r}_0 = \mathbf{b} - \mathbf{A}\mathbf{x}_i$. This is the direction on which the function decreases most quickly. The size of the step is determined by α_i. The size α_i is selected such that it minimises the quadratic function $f(\mathbf{x}_i + \alpha_i\mathbf{d}_i)$. The new point and the residual are updated and the coefficient β is chosen such that $\mathbf{d}_{i+1}$ is conjugated to the previous $\mathbf{d}_i$. The algorithm stops when the norm of the residual is less than a selected tolerance or it reaches the maximum number of iterations.

One dimension For our problem, recall equation (4.11), the matrix $\mathbf{A}$ is $F_1 F_1^*$, the vector $\mathbf{x}$ is $M_x'(\mathbf{x})$ and $\mathbf{b}$ is the MRI signal, $S(\mathbf{k_x})$.

$$\mathbf{Ax} = \mathbf{b} \;\longrightarrow\; (F_1 F_1^*) M_x'(\mathbf{x}) = S(\mathbf{k_x}). \tag{5.4}$$

To compute the matrix $\tilde{F}_1 \tilde{F}_1^*$, only the first column of this matrix is needed since it is a Toeplitz and Hermitian matrix. The first column is obtained multiplying by the first canonical vector $\mathbf{e}_1$, i.e.

$$(\tilde{F}_1 \tilde{F}_1^*)\mathbf{e}_1 = (\tilde{F}_1 \tilde{F}_1^*) \begin{bmatrix} 1 \\ 0 \\ \vdots \\ 0 \end{bmatrix}. \tag{5.5}$$

Moreover, $\tilde{F}_1^* \mathbf{e}_1 = \mathbf{1}$, where $\mathbf{1}$ is a vector of ones. Therefore, only $\tilde{F}_1 \mathbf{1}$ is computed, using a nonuniform Fourier transform of type one.
Afterwards, the Conjugate Gradient method is applied to solve M_x', where $M_x' = (\tilde{F}_1^*)^{-1} M_x$. Therefore, to obtain the desired object M_x, the conjugate of the nonuniform Fourier matrix must be applied. This is done by applying the nonuniform Fourier transform of type two to the conjugate of M_x' and then taking the conjugate of the result.

$$M_x = \tilde{F}_1^* M_x' = \left((\tilde{F}_1^* M_x')^*\right)^* = (M_x'^* \tilde{F}_1)^* = \text{conj}\big(\tilde{F}_1^T \text{conj}(M_x')\big) = \text{conj}\big(\tilde{F}_2 \text{conj}(M_x')\big). \tag{5.6}$$

Two dimensions For the two dimensional problem, equation (4.17) has to be solved using CG.

$$\mathbf{Ax} = \mathbf{b} \;\longrightarrow\; \left((\tilde{F}_1^{x*} \tilde{F}_1^x)^T \otimes (\tilde{F}_1^y \tilde{F}_1^{y*})\right) \mathbf{M}_{xy}' = \mathbf{S}. \tag{5.7}$$

Where $\mathbf{A}$ corresponds to the resulting matrix when applying the Kronecker product, the aim is to solve $\mathbf{x}$, which is $\mathbf{M}_{xy}'$, and $\mathbf{b}$ corresponds to the MRI signal $\mathbf{S}$.
Regarding the matrices $(\tilde{F}_1^y \tilde{F}_1^{y*})$ and $(\tilde{F}_1^{x*} \tilde{F}_1^x)$, they are Hermitian and Toeplitz and therefore only a column or a row needs to be known to construct them. This is achieved multiplying by the canonical matrix $\mathbf{E}_1$.

$$(\tilde{F}_1^y \tilde{F}_1^{y*})\mathbf{E}_1(\tilde{F}_1^{x*} \tilde{F}_1^x) = (\tilde{F}_1^y \tilde{F}_1^{y*}) \begin{bmatrix} 1 & 0 & \cdots & 0 \\ 0 & 0 & \cdots & 0 \\ \vdots & \vdots & \ddots & \vdots \\ 0 & 0 & \cdots & 0 \end{bmatrix} (\tilde{F}_1^{x*} \tilde{F}_1^x). \tag{5.8}$$

Very similar to the 1D case, $\tilde{F}_1^{y*} \mathbf{E}_1 \tilde{F}_1^{x*}$ gives a $mn \times mn$ matrix of ones. Therefore, to obtain the first column of $(\tilde{F}_1^y \tilde{F}_1^{y*})$ and the first row of $(\tilde{F}_1^{x*} \tilde{F}_1^x)$, a 2D NUFFT-I has to be applied to a matrix of ones.
Subsequently, the Kronecker product is perform to obtain $(\tilde{F}_1^{x*} \tilde{F}_1^x)^T \otimes (\tilde{F}_1^y \tilde{F}_1^{y*})$.
The Conjugate Gradient solves $\mathbf{M}_{xy}'$. To retrieve the object, the solution vector is reshaped to an $m \times n$ matrix and conjugated. A 2D NUFFT-II is performed and the conjugate of the result is taken to obtain M_{xy}, i.e.

$$M_{xy} = \text{conj}\left(\tilde{F}_2^y\right) \text{conj}\left(M_{xy}'\right) \tilde{F}_2^x\big). \tag{5.9}$$

5.2. Nonuniform Fast Fourier Transform

The steps taken in the algorithm for the nonuniform fast Fourier transform will be explained in the following subsections. In 5.2.1 for one dimension and in 5.2.2 for two dimensions.

5.2.1. One-dimensional NUFFT

In section 3.3.1, the theoretical base of the one dimensional nonuniform Fourier transform of type one was explained. Regarding how the algorithm is implemented in MATLAB, a brief explanation will follow.
The function takes the time domain vector $\mathbf{c}$ and the nonequispaced frequencies $\boldsymbol{\omega}$ (equation (3.10)) as input arguments and returns the computed values for the frequency domain $\mathbf{f}$. The corresponding input for the nonequispaced frequencies $\boldsymbol{\omega}$ is the magnetic field $\Delta B_x(\mathbf{x})$. Another optional input is the working precision ϵ, which is double by default. Then the parameters for the algorithm and the matrices $D_{\mathbf{v}}$ and $D_{\mathbf{u}}$ are computed.

1. The sequence $\mathbf{s}$ with the closest equispaced frequencies is created, rounding $N\Delta B_x(\mathbf{x})$ to the closest integer. Where N is the number of samples.
2. From $\mathbf{s}$, the new sequence $\mathbf{t}$ is generated. Assigning the values $t_p = N$ to $t_p = 0$, for $0 \leq p \leq N-1$. The $\mathbf{t}$ sequence is used to index the columns of the uniform Fourier matrix F.
3. The perturbation parameter δ ((3.17)) is computed taking the maximum distance between $\mathbf{s}$ and $N\Delta B_x(\mathbf{x})$, i.e. $\delta = |N\Delta B_x(\mathbf{x}) - \mathbf{s}|_\infty$.
4. The integer K is computed following the equation (3.16).

5. With all the previous parameters, the matrices $D_{\mathbf{u}}$ and $D_{\mathbf{v}}$ from equation (3.15) are evaluated using Chebyshev expansions. The columns of these matrices correspond to the vectors $\mathbf{u}_0, \ldots, \mathbf{u}_{K-1}$ and $\mathbf{v}_0, \ldots, \mathbf{v}_{K-1}$.

The last part of the algorithm consists in performing the nonuniform Fourier transform in two steps. These two steps present some difference for the type one and type two. In other words, the first five steps are the same for the NUDFT-I and NUDFT-II. Nevertheless, the sixth and seventh steps differ depending on the type of the nonuniform algorithm and therefore, these steps will be explained separately below.
First the steps for the type one are described:

6. Generate the inverse of the DFT matrix (or the conjugate) with the columns given by the sequence $\mathbf{t}$, multiply each column of the matrix $D_{\mathbf{u}}$ by the time domain vector, and conjugate the result.

$$X = \text{conj}\left(F^* I(:, \mathbf{t}) \text{conj}\left(\left[D_{\mathbf{u}_0}\mathbf{c} | \ldots | D_{\mathbf{u}_{K-1}}\mathbf{c}\right]\right)\right). \tag{5.10}$$

7. Multiply each column of the result of the equation (5.10) by each column of the matrix $D_{\mathbf{v}}$ and performing the sum.

$$\tilde{F}_1\mathbf{c} = \left[D_{\mathbf{v}_0}X_0 | \ldots | D_{\mathbf{v}_{K-1}}X_{K-1}\right]\begin{bmatrix}1\\ \vdots \\ 1\end{bmatrix}. \tag{5.11}$$

The last two steps for the type two NUFFT are described in the following lines.

6. Generate the DFT matrix with the rows given by the sequence $\mathbf{t}$ and multiply each column of the matrix $D_{\mathbf{v}}$ by the time domain vector.

$$X = I(\mathbf{t}, :)F\left[D_{\mathbf{v}_0}\mathbf{c} | \ldots | D_{\mathbf{v}_{K-1}}\mathbf{c}\right]. \tag{5.12}$$

7. Multiply each column of the result of the equation (5.12) by each column of the matrix $D_{\mathbf{u}}$ and performing the sum.

$$\tilde{F}_2\mathbf{c} = \left[D_{\mathbf{u}_0}X_0 | \ldots | D_{\mathbf{u}_{K-1}}X_{K-1}\right]\begin{bmatrix}1\\ \vdots \\ 1\end{bmatrix}. \tag{5.13}$$

The first five steps, where the necessary data to perform the NUDFT is computed, are known as the planning stage, while the last two steps are known as the online stage. The algorithm for the nonuniform fast Fourier transform is represented in the diagram block of figure 5.1.
Only the online stage is taken into account when measuring the time that it takes to perform the approximation of the nonuniform Fourier transform, i.e. K FFT operations. When the NUDFT needs to be performed on more than one vector, the planning stage is carried out only once whereas the online stage is done for each vector.
With respect to the algorithm for the NUFFT-II, it is analogous to the NUFFT-I. The matrix for the nonuniform Fourier transform of type two, is achieved by transposing the matrix of type one. The reader is referred to [30] for more details.

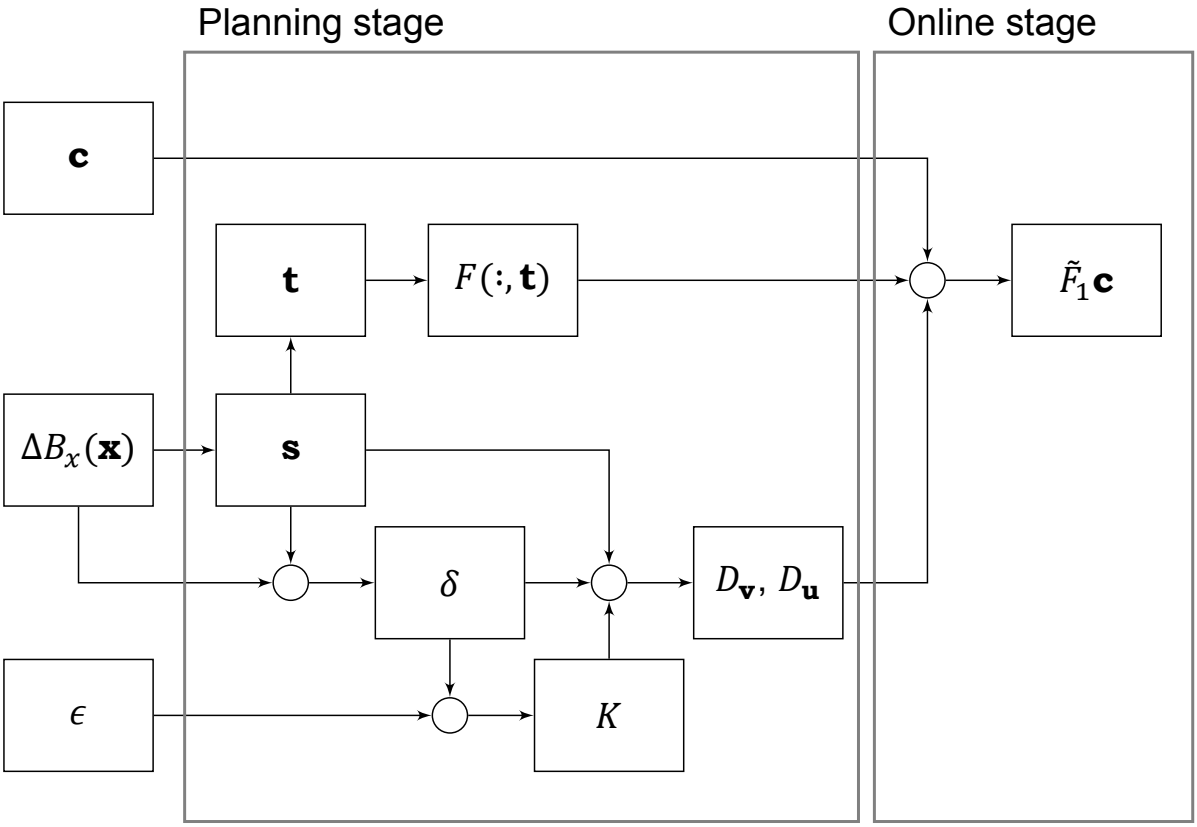

Figure 5.1: Scheme of the nonuniform fast Fourier transform algorithm for one dimension

5.2.2. Two-dimensional NUFFT

The theoretical base of the 2D nonuniform fast Fourier transform algorithm can be found in section 3.4. The first steps of the two-dimensional algorithm are similar to the one dimensional case described in subsection 5.2.1, but repeating the process for the second dimension:

1. The matrices of the magnetic fields ΔB_x and ΔB_y are reshaped as column vectors. Therefore, now $\Delta B_x(\mathbf{r}) \in \mathbb{Q}^{mn\times 1}$ and $\Delta B_y(\mathbf{r}) \in \mathbb{Q}^{mn\times 1}$, where $r_0, \dots, r_{mn-1} \in [0, mn-1]$.
2. The sequences $\mathbf{s^x}$ and $\mathbf{s^y}$ are created, rounding the values of the magnetic fields $\Delta B_x(\mathbf{r})$ and $\Delta B_y(\mathbf{r})$ respectively to the closest point in an equispaced grid.
3. The respective $\mathbf{t}$ sequences are built from $\mathbf{s^x}$ and $\mathbf{s^y}$, assigning zero to the values that are $t_p^x = n$ or $t_q^y = m$.
4. Two perturbation parameters are computed using equation (3.17). The first, δ_x, as the maximum distance between $\mathbf{s^x}$ and $n\Delta B_x(\mathbf{r})$ and the second, δ_y, as the maximum distance between $\mathbf{s^y}$ and $m\Delta B_y(\mathbf{r})$. The maximum distance is calculated taking the infinite norm of the difference.
5. Each rank of the matrix, K_x and K_y, is obtained using the equation (3.16).
6. The matrices $D_{\mathbf{u}}^x$, $D_{\mathbf{u}}^y$ and $D_{\mathbf{v}}^x$, $D_{\mathbf{v}}^y$ from equation (3.25) are calculated with their respective parameters. The columns of these matrices are the vectors $\mathbf{u}_0^x, \dots, \mathbf{u}_{K-1}^x$ for $D_{\mathbf{u}}^x$, $\mathbf{u}_0^y, \dots, \mathbf{u}_{K-1}^y$ for $D_{\mathbf{u}}^y$ and $\mathbf{v}_0^x, \dots, \mathbf{v}_{K-1}^x$ for $D_{\mathbf{v}}^x$, $\mathbf{v}_0^y, \dots, \mathbf{v}_{K-1}^y$ for $D_{\mathbf{v}}^y$.

The previous steps belong to the planning stage mentioned in section 4.2. Now the 2D Fourier transform has to be performed on the object, this is done by multiplying the left and right side of the matrix of the object by the 1D Fourier transform (see equations (3.22) and (3.25)). Four steps are needed for this which are known as the online stage. Two nested *for* loops, with variables r and s, are required to go through all the columns of the matrices of step 6. Therefore, $0 \le r \le K^x - 1$ and $0 \le s \le K^y - 1$.
Like the 1D case, the online stage for the type one and type two NUFFT are different and therefore, these steps will be explained separately. First the ones for the 2D NUFFT-I are described below. These steps are equivalent to perform equation (3.25).

7. Multiply the object by the $D_{\mathbf{u}}$ matrices.

$$DcD = D_{\mathbf{u}_s^y} \cdot \text{diag}(\mathbf{c}) \cdot D_{\mathbf{u}_r^x} \tag{5.14}$$

Recall that $D^x_{\mathbf{u}_r}$ and $D^y_{\mathbf{u}_s}$ are diagonal matrices with the elements of the vectors $\mathbf{u}^x_r$ and $\mathbf{u}^y_s$ as entries, respectively.

8. Left and right multiply by the identity matrices indexed by the $\mathbf{t}$ sequences[1].

$$DcDt = I(:, \mathbf{t^y}) \cdot DcD \cdot I(:, \mathbf{t^x})^T \tag{5.15}$$

9. The FFT is applied from the left and then multiply by $D^y_{\mathbf{u}_s}$

$$DFt = D_{\mathbf{v}^y_s} \cdot F \cdot DcDt \tag{5.16}$$

Where $D^y_{\mathbf{v}_s}$ is a diagonal matrix with the elements of the vector $\mathbf{v}^y_s$ as entries.

10. The last step consists in performing the FFT from the right, multiplying the result by the diagonal matrix $D^x_{\mathbf{v}_r}$ (which has the elements of the vector $\mathbf{v}^x_r$ as entries) and summing.

$$f = f + DFt \cdot F \cdot D^x_{\mathbf{v}_r} \tag{5.17}$$

The last four steps are summarised in the algorithm 2 and a graphic visualisation of the nine steps can be seen in figure 5.1.
Now we proceed to explain the online stage steps for the type two NUFFT, which corresponds of performing equation (3.29).

7. Multiply the time domain matrix c by the $D^x_{\mathbf{v}}$ matrix and perform FFT from the right.

$$Ar = c \cdot D_{\mathbf{v}^x_r} \cdot F. \tag{5.18}$$

8. Repeat the process with the $D^y_{\mathbf{v}}$ matrix and multiplying from the left.

$$As = F \cdot D_{\mathbf{v}^y_s} \cdot Ar. \tag{5.19}$$

9. Index with the $\mathbf{t}^x$ and $\mathbf{t}^y$ sequences[2].

$$ft = I(\mathbf{t}^y, :) \cdot As \cdot I(\mathbf{t}^x, :)^T. \tag{5.20}$$

10. The last step consists in multiplying by the $D_{\mathbf{u}}$ and summing.

$$f = f + D_{\mathbf{u}^y_s} \cdot ft \cdot D_{\mathbf{u}^x_r}. \tag{5.21}$$

These four steps can be seen in the algorithm 3.

Algorithm 2 Online Stage for the 2D NUFFT-I

Initialise f
for $r = 0, 1, \ldots, K^x - 1$ **do**
  Multiplication by D_u matrix $Dc = D^x_{\mathbf{u}_r} .* c(:)$
  for $s = 0, 1, \ldots, K^y - 1$ **do**
    Multiplication by D_u matrix $DcD = Dc .* D^y_{\mathbf{u}_s}$
    Index with $\mathbf{t}$ sequences $DcDt = I(:, \mathbf{t^y}) \cdot DcD \cdot I(:, \mathbf{t^x})^T$
    FFTs and multiply by D_v matrices and sum $f = f + D^y_{\mathbf{v}_s} \cdot \text{fft}\left(D^x_{\mathbf{v}_r} \cdot \text{fft}(DcDt^T)\right)^T$
  end for
end for

[1] This can be done using *accumarray()* function in MATLAB.
[2] This can be done taking the $mt^x_j + t^y_j$ element of the As matrix.

Algorithm 3 Online Stage for the 2D NUFFT-II

Initialise f
for $r = 0, 1, \ldots, K^x - 1$ **do**
  Multiplication by D_v matrix and FFT $Ar = \text{fft}(D^x_{\mathbf{v}_r} \cdot c^T)^T$
  for $s = 0, 1, \ldots, K^y - 1$ **do**
    Multiplication by D_v matrix and FFT $As = \text{fft}(D^y_{\mathbf{v}_s} \cdot Ar)$
    Index with **t** sequences $ft = I(\mathbf{t^y}, :) \cdot As \cdot I(\mathbf{t^x}, :)^T$
    Multiply by D_u matrices and sum $f = f + D^y_{\mathbf{u}_s} \cdot ft \cdot D^x_{\mathbf{u}_r}$
  end for
end for

III

Results and Discussion

6

NUFFT in One Dimension

In this chapter, we will investigate whether the NUFFT algorithm described in the previous chapter 3 and in subsection 5.2.1 can be used to recover the scanned object from the one-dimensional MRI received signal using the functions from Chebfun [5] in MATLAB.
The chapter has been organised in the following way. In the first place, an introduction in section 6.1 to explain the purpose of this chapter is given. The results are showed in section 6.2. The last part of this chapter is concerned with the performance of the NUFFT algorithm and the computational time that it costs, these are sections 6.3 and 6.4 respectively.
Regarding section 6.2, where the results of the research are presented, the outline is summarised below.

- A brief explanation of how the nonuniform fast Fourier transform algorithm works for a certain object and magnetic field is given. In other words, how the $\mathbf{s}$ and $\mathbf{t}$ sequences are generated (steps 1 and 2 of subsection 5.2.1). The value of the parameters δ and K, equations (3.17) and (3.18), which corresponds to steps 3 and 4 of subsection 5.2.1. And last, the construction of the matrices $D_{\mathbf{u}}$ and $D_{\mathbf{v}}$ (step 5 of subsection 5.2.1).
- The MRI signal received is compared to the ideal MRI signal, i.e. the signal that an MRI with an ideal magnetic field would give.
- The object retrieved using the conventional fast Fourier transform algorithm *fft()* and the object retrieved using the nonuniform fast Fourier transform algorithm *nufft()* are compared.
- Finally, a priori information is used to improve the results.

6.1. Introduction

The results that will be shown along this chapter will be focused on the nonuniform Fast Fourier transform algorithm. In order to explain with an example how the *nufft()* from [5] works and the time that it costs.
In this chapter, one iteration of the Conjugate Gradient will be performed. One iteration of the CG results in applying the nonuniform Fourier transform to the signal received.
Looking at the algorithm 1, the first step is to initialised the vector $\mathbf{x}_0$. It is initialised with zeros by default. Therefore, the search direction and the residual are

$$\mathbf{d}_0 = \mathbf{r}_0 = \mathbf{b} - \mathbf{A}\mathbf{x}_0 = \mathbf{b} - \mathbf{A}\mathbf{0} = \mathbf{b}. \tag{6.1}$$

For our particular case, $\mathbf{b} = S(\mathbf{k_x})$, $\mathbf{A} = (\tilde{F}_1\tilde{F}_1^*)$ and $\mathbf{x} = M_x'(\mathbf{x})$ (see figure 4.3). The third step of the CG algorithm is to compute the size of the step α_0, which is a scalar, and then update the solution as follows

$$M_x'(\mathbf{x})_1 = M_x'(\mathbf{x})_0 + \alpha_0\mathbf{d}_0 = \mathbf{0} + \alpha_0 S(\mathbf{k_x}) = \alpha_0 S(\mathbf{k_x}). \tag{6.2}$$

The solution that the CG gives with just one iteration is $M_x'(\mathbf{x})_1 = \alpha_0 S(\mathbf{k_x})$. To retrieve the object, the conjugate of the nonuniform Fourier transform of type one is applied to the solution of the CG. As explained in section 5.1, $\tilde{F}_1^* M_x'$ is done by applying the nonuniform Fourier transform of type two to the conjugate of M_x' and then taking the conjugate of the result, i.e.

$$M_x(\mathbf{x}) = \tilde{F}_1^* M_x' = \tilde{F}_1^* \alpha_0 S(\mathbf{k_x}) \approx \text{conj}\left(\tilde{F}_2 \text{conj}\big(S(\mathbf{k_x})\big)\right). \tag{6.3}$$

In order to simplify the notation, the scalar α_0 is omitted. The algorithm of the nonuniform Fourier transform of type two, described in section 3.5, is analogous to the type one explained in section 5.2, but working with rows instead of columns.

6.2. Retrieving the Object

An object with a square shape will be retrieved using four different magnetic fields, applying the uniform and nonuniform fast Fourier transform algorithm. The results of both algorithms will be compared. The number of samples used for the following examples is $N = 2^6 = 64$. The working precision is double, $\epsilon = 2.22\text{e}{-16}$. The object used can be seen in figure 6.1 and the magnetic fields in figure 6.2.

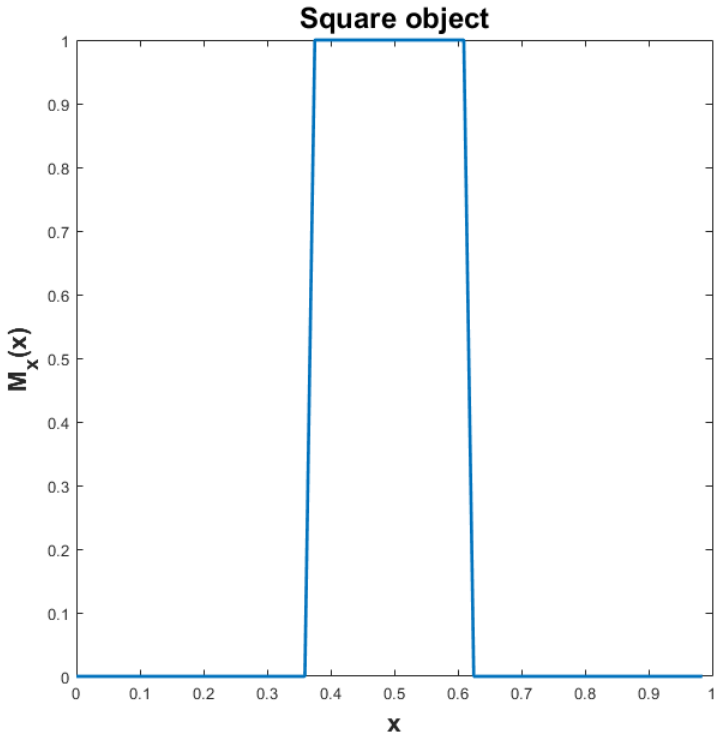

Figure 6.1: Square shaped object used in the experiments

In this section, only the results obtained from the low magnetic fields (the two at the bottom of figure 6.2) will be shown. In order to see the results from the other two magnetic fields, the reader is referred to the appendix A.

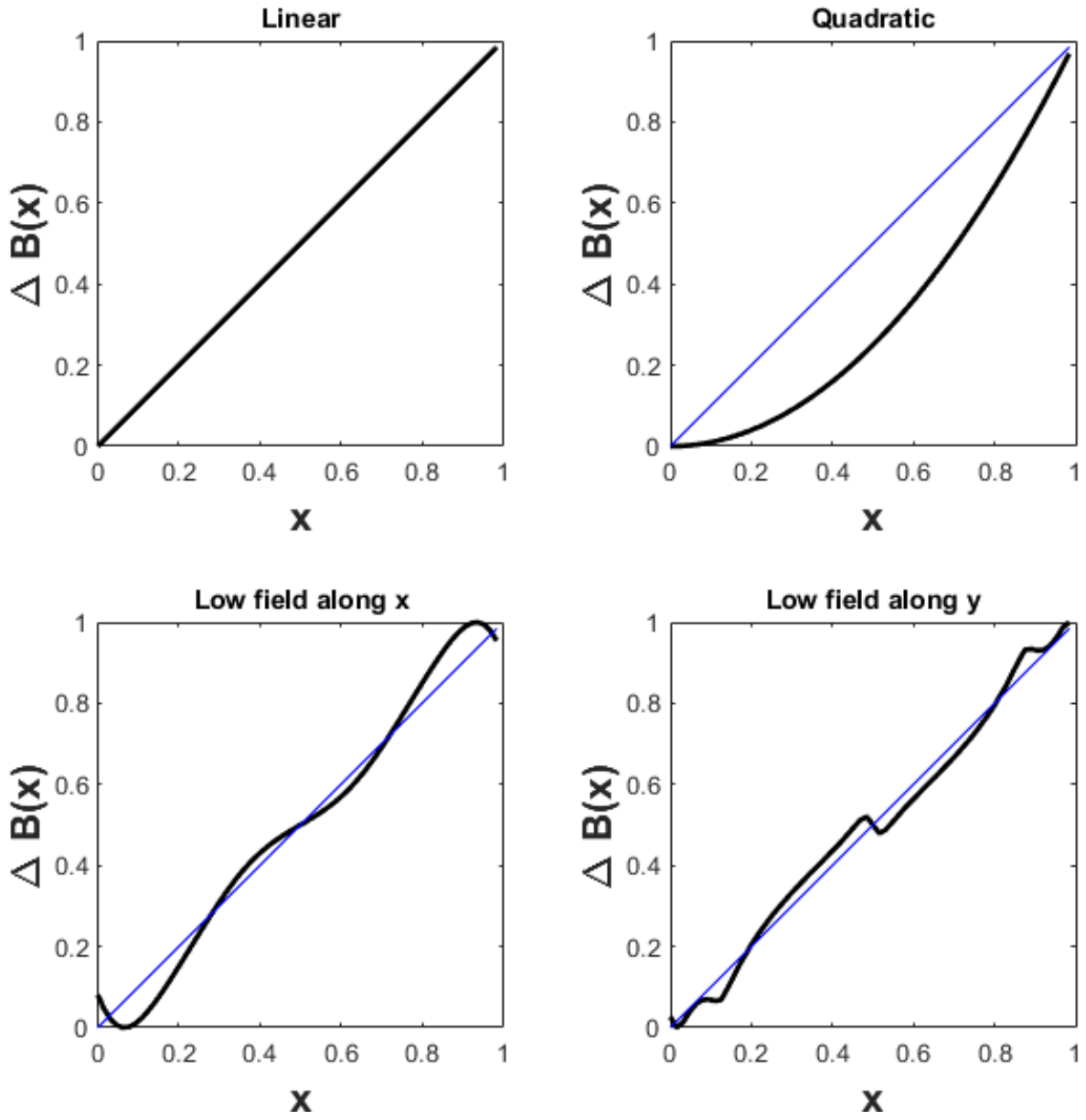

Figure 6.2: Four normalised magnetic fields used. From left to right and top to bottom: linear, quadratic, low gradient field along the x-direction and low magnetic field along the y-direction. The nonlinear fields are compared to the linear case represented with a blue line

6.2.1. Low Magnetic Field

The last two examples are the low magnetic fields, the third and fourth images in figure 6.2. The shapes of these fields were taken from one slice of the gradient maps of the low-field MRI scanner in Leiden University Medical Center [27].

The first field was taken from the gradient field along the x-direction. It presents nonidealities at the edges as two bumps, one going downwards and the second upwards, whereas in the middle part is approximately an ideal linear field. The second was taken from the gradient field along the y-direction. It is very close to the linear field except for the discontinuity at the middle and two peaks at the edges.

The sequences $\mathbf{s}/N$ and $\mathbf{t}/N$ generated are in figure 6.3. The left image corresponds to the low-field along x-direction. Several nonuniform samples are assigned to the same uniform nodes at the beginning and at the end of the field, where the two bumps appear. This also happens at the middle of the field but to a lesser extent. Therefore, this is similar to oversampling. At the right bump, the magnetic field achieves the values $\Delta B_x(x) = 1$, and therefore, the $\mathbf{t}$ sequence adjusts this values to zero.

Regarding the field along the y-direction, many uniform nodes adopt the same values at the peaks in the edges. Its $\mathbf{t}$ sequence assigns one value to zero in the last sample. At the middle part ($x \in [0.4, 0.6]$), where the object is placed, a significant discontinuity arises that will lead to nonidealities in the MRI signal and the object retrieved. The perturbation parameters (equation (3.17)) of the field along x- and y-direction are $\delta_x = 0.4871$ and $\delta_y = 0.4896$

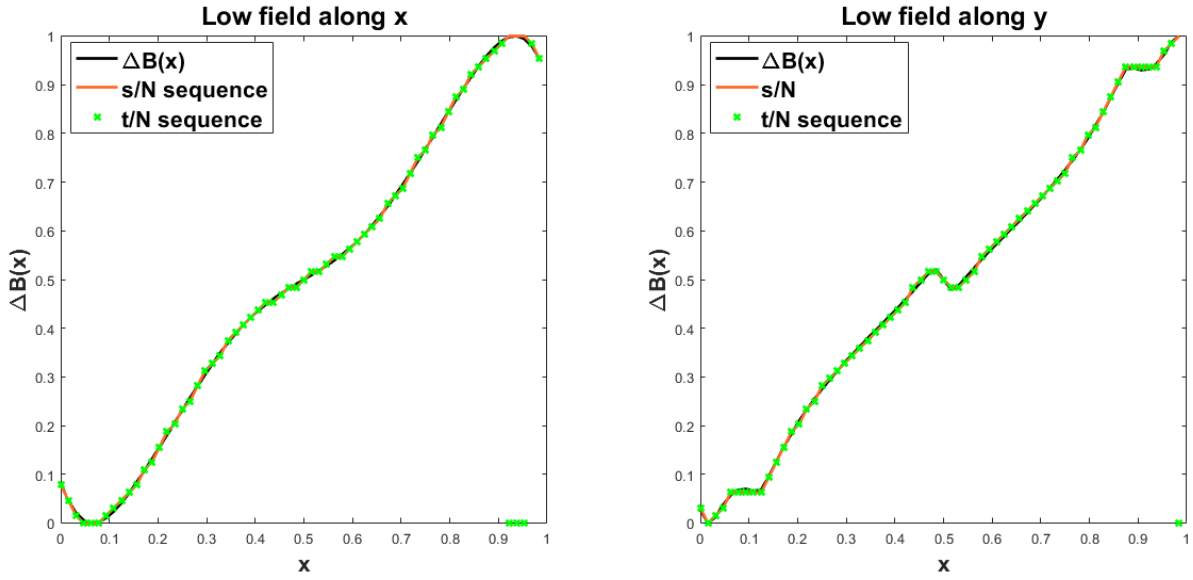

Figure 6.3: Low magnetic fields (second and third images in figure 6.2) and their respective sequences $\mathbf{s}/N$ and $\mathbf{t}/N$

respectively, and the integers $K_x = 15$ and $K_y = 16$. Nonetheless, for both cases the rank of the matrix $D_{\mathbf{u}}$ is less than the required K (see section 6.3 for more details).

Now we will focus in the result of the gradient field along the x-direction. The MRI signal is in figure 6.4. It can be seen that the signal is similar to the ideal but oversampled. This explains the narrow width of the object retrieved using the uniform FFT, left image in figure 6.6.

Another way to understand why the conventional Fourier transform does not calculate the width of the square pulse correctly can be seen looking at the shape of the field in the square, which is not completely linear. The small bump going upwards produces a negative delay while the bump going downwards produces a positive delay, both resulting in a narrowed object. This can be seen in figure 6.5, where the negative and the positive delay are indicated with arrows and a pink and purple dots respectively.

The nonuniform algorithm, right side of figure 6.6, presents the width of the square correctly but has more nonidealities in the flat areas than the ideal case. This can be improved by eliminating half of the highest k-space samples.

Moving to the results of the gradient field along the y-direction, last image of figure 6.2, we start looking at the MRI signal received in figure 6.7. The difference between this signal and the ideal is greater than the one for the previous case, with the field along x-direction. The reason of the degraded quality of the signal is because of the discontinuity in the middle part of the field, that coincides with the object. This can be seen in figure 6.8.

Since many of the samples in this interval are associated to the same value of the magnetic field, the signal is ambiguously encoded and leads to accentuated peaks in the object reconstruction. With a nonbijective encoding, any frequency value may be associated to multiple locations in the image domain and thus the exact ideal object cannot be retrieved.

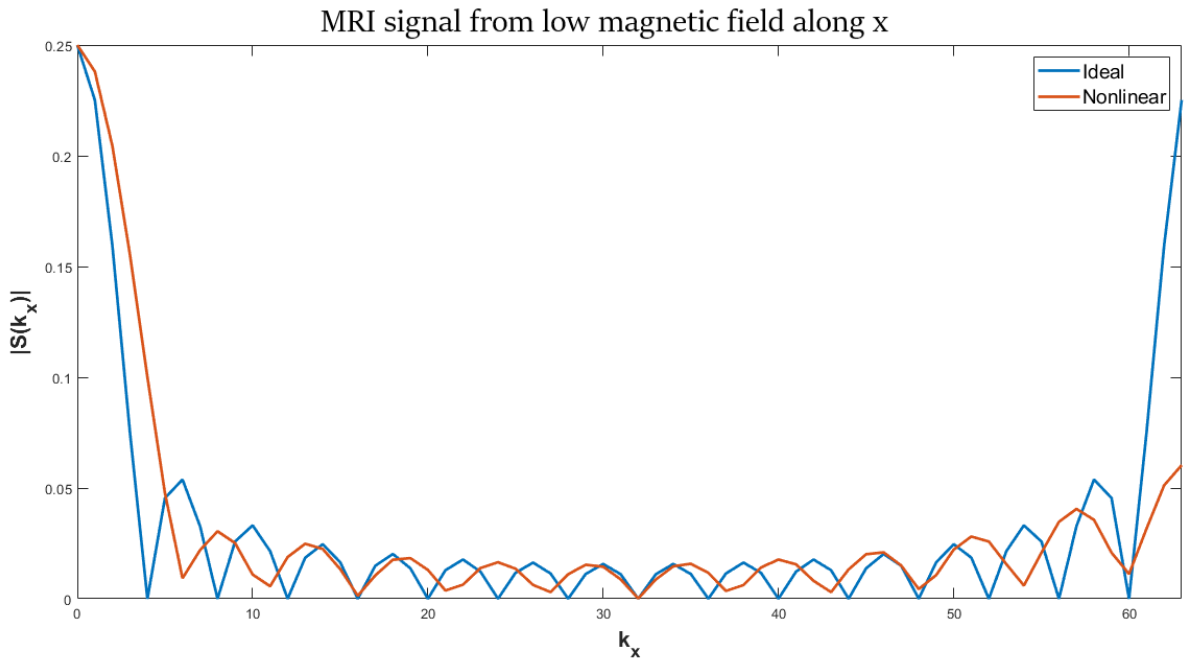

Figure 6.4: Received MRI signals from a square object in a low magnetic field along x-direction (third image in figure 6.2) compared to the ideal MRI signal, i.e. the signal received when applying the uniform *fft()*

The left image of figure 6.9 shows the object retrieved using the uniform FFT. The shape of the square is completely lost. As explained before, this is due to the significant nonideal shape of the field over the object.

Like the previous case with the quadratic field, the MRI signal presents conjugate symmetry. Therefore, eliminating half of the k-space samples and applying a Hamming window to the MRI signal gives the results seen in figure 6.10. The left image correspond to the gradient field along x-direction, and the right image corresponds to the gradient field along y-direction.

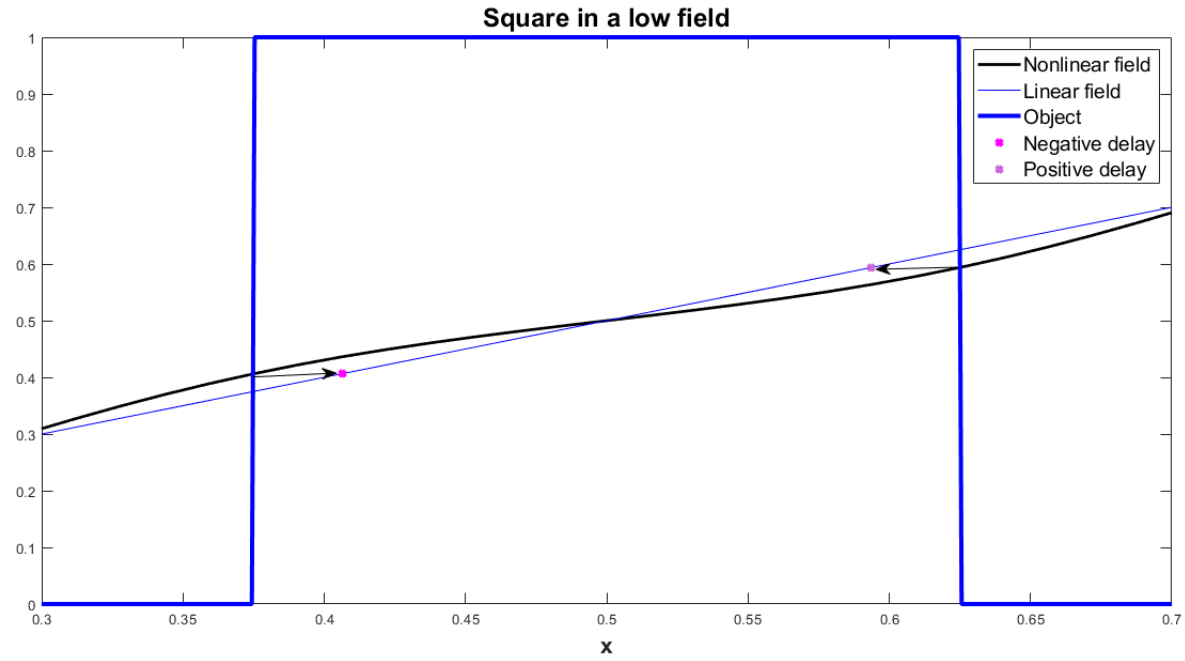

Figure 6.5: Both delays that the low magnetic field (third image in figure 6.2) produces when retrieving the object using the *fft()*

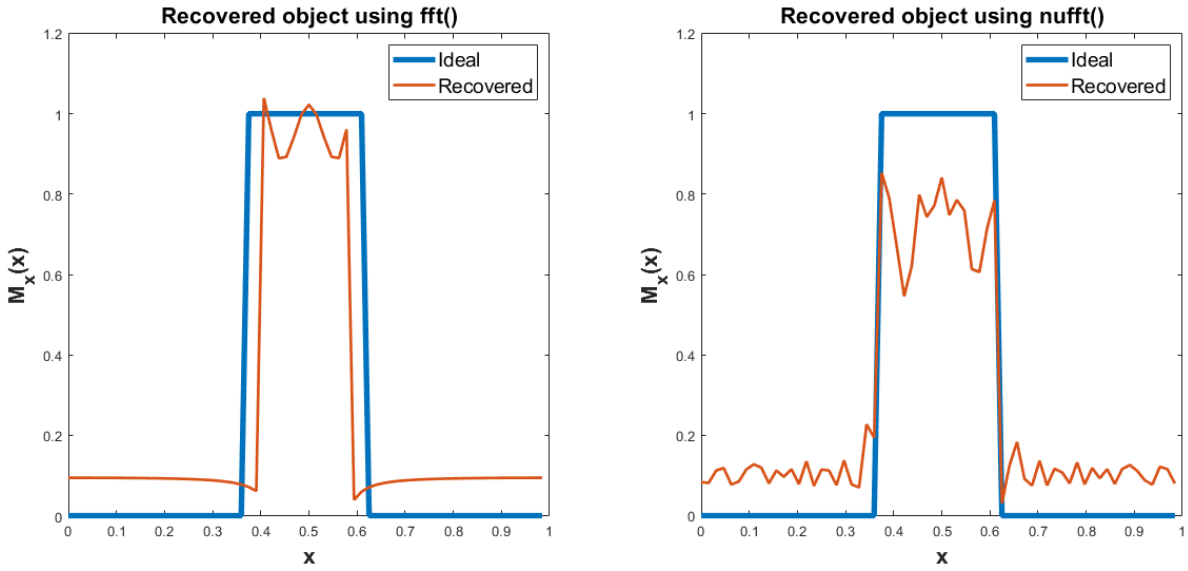

Figure 6.6: To the left, recovered square pulse from a low magnetic field, third image in figure 6.2, using the Fourier transform algorithm, *fft()*. To the right, same object recovered using the nonuniform Fourier transform algorithm, *nufft()*. Both cases are compared to the ideal object

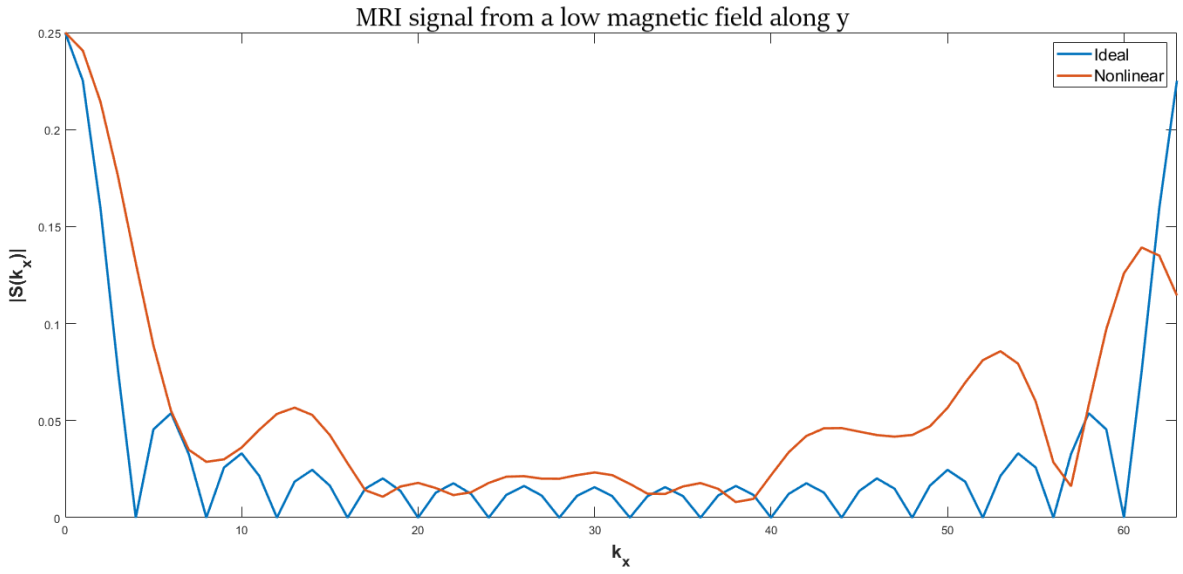

Figure 6.7: Received MRI signals from a square object in a low magnetic field along y-direction (fourth image in figure 6.2) compared to the ideal MRI signal, i.e. the signal received when applying the uniform *fft()*

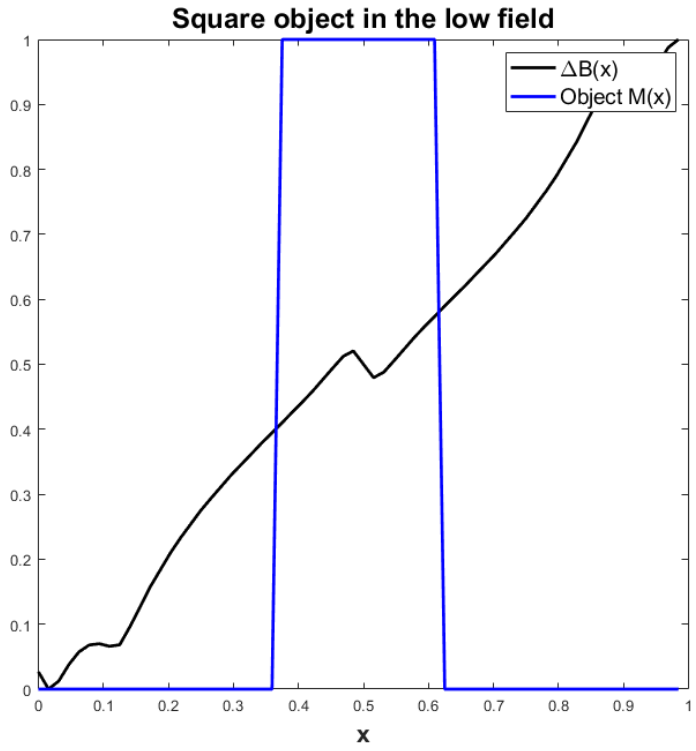

Figure 6.8: Low magnetic field along y-direction (fourth image in figure 6.2) and the ideal square object

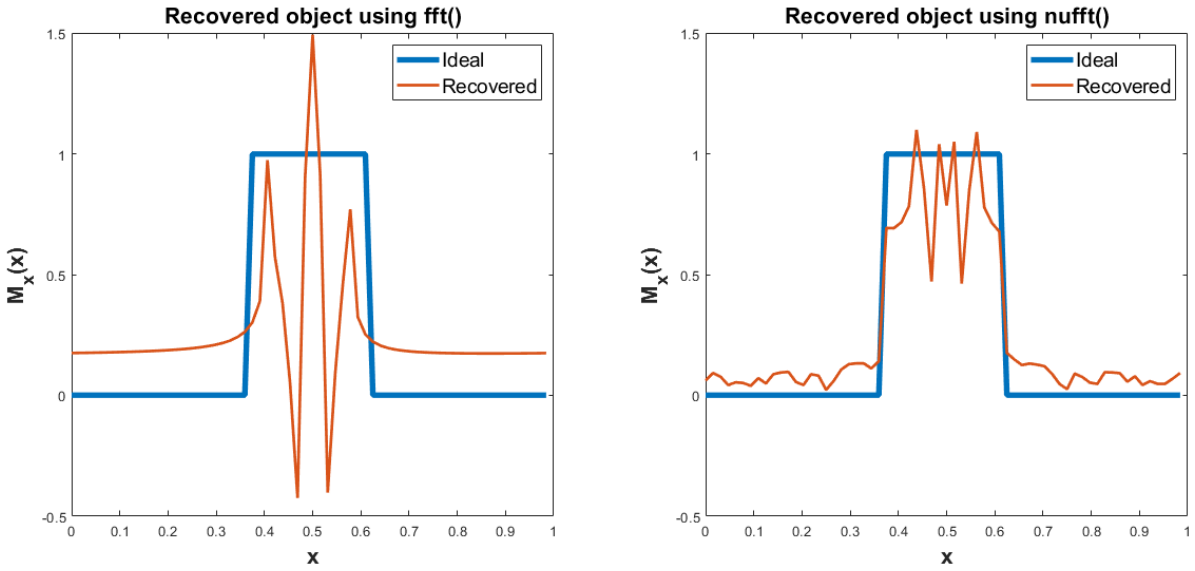

Figure 6.9: To the left, recovered square pulse from a low magnetic field, fourth image in figure 6.2, using the Fourier transform algorithm, *fft()*. To the right, same object recovered using the nonuniform Fourier transform algorithm, *nufft()*. Both cases are compared to the ideal object

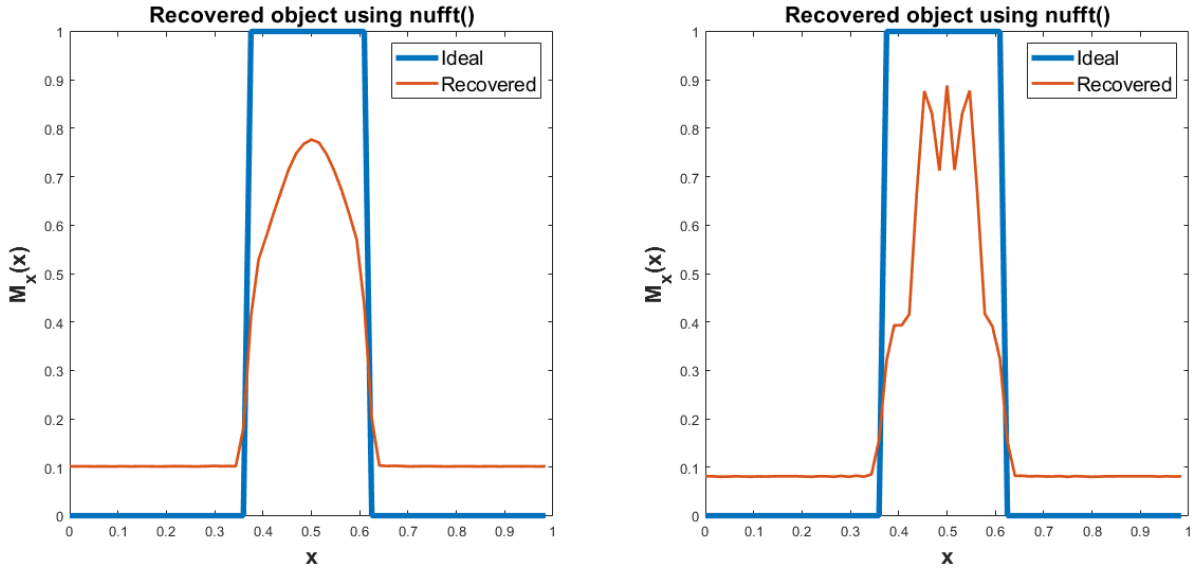

Figure 6.10: To the left, recovered square pulse from a low gradient field along x-direction (third image in figure 6.2) using the *nufft()*, half of the k-space samples and a Hamming window. To the right, same object recovered from a low magnetic field along y-direction, using the *nufft()*, half of the k-space samples and a Hamming window. Both cases are compared to the ideal object

6.3. NUFFT Performance with Different Values of *K*

In order to improve the quality of the object retrieved, one can think that lowering the working precision would help. Looking at equation (3.18), it can be seen that the smaller ϵ is, the higher K is and the more FFT operations are done in the nonuniform algorithm, i.e. $KN \log N$, and therefore, more accurate results. On the other hand, if this number is reduced, the number of operations decreases and therefore, the performance would worsen.
Nevertheless, it was seen in section 6.2 that the rank of the matrix $D_{\mathbf{u}}$ was less than the required K computed. This means that some of the columns of this matrix are linear combinations of each other and then these could be eliminated. Note that the columns of $D_{\mathbf{u}}$ correspond to the vectors $\mathbf{u}_0, \dots, \mathbf{u}_{K-1}$.
Moreover, the corresponding columns of the matrix $D_{\mathbf{v}}$ can be removed as well. In this section, the integer K will be fixed to study whether the number of columns of the matrices $D_{\mathbf{v}}$ and $D_{\mathbf{u}}$ can be reduced and therefore, save computational time.
The Singular Value Decomposition (SVD) [38] is used to determine the rank of the matrix $D_{\mathbf{u}}$. The number of nonzero singular values equals the rank of the matrix. The SVD consists in factorising the complex matrix $D_{\mathbf{u}}$ as

$$D_{\mathbf{u}} = \mathbb{U}\Sigma\mathbb{V}^* \tag{6.4}$$

Where the diagonal matrix Σ contains the singular values $\sigma_1, \dots, \sigma_i, \dots, \sigma_K$, where σ_1 is the biggest. These entries are real and non-negative. The singular values that are $\sigma_i < 0.02\sigma_1$ are set to zero. The criteria to determine which singular values are close to zero and which singular values are nonzero was chosen empirically.
Figure 6.11 shows the singular values of the matrix $D_{\mathbf{u}}$ corresponding to the low-field along the x-direction. The singular values from the 5th to the 15th are close to zero and this is were the threshold for the criteria is set. The singular values corresponding to the quadratic field and the low-field along the y-direction are analogous to the low-field along the x-direction and their figures will no be shown.

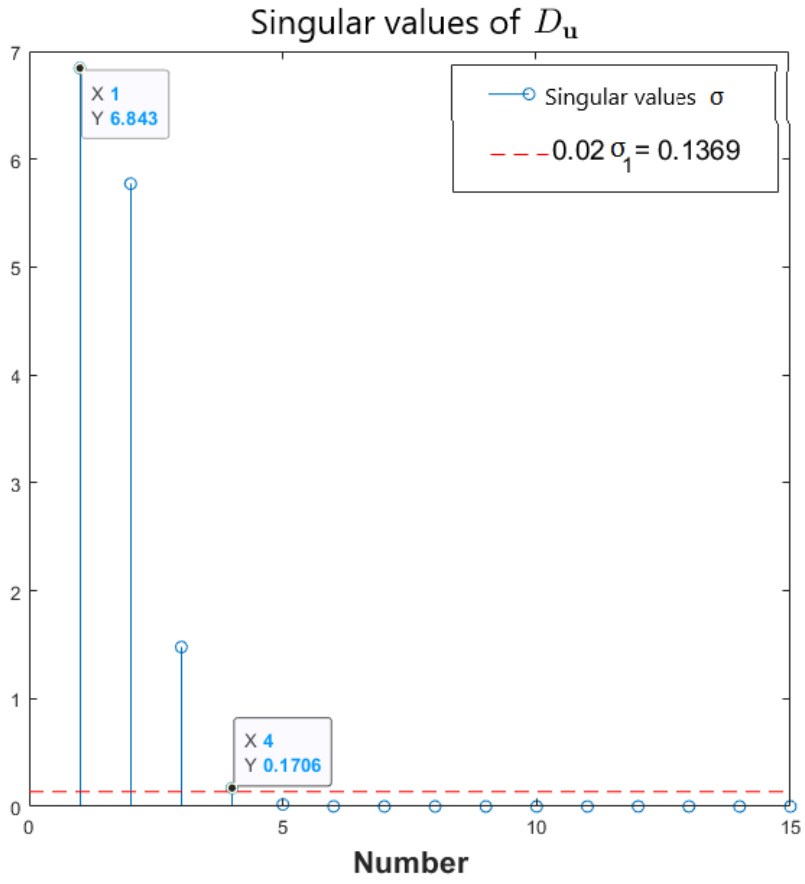

Figure 6.11: Singular values of the matrix $D_{\mathbf{u}}$ corresponding to the low gradient field along x-direction (third image in figure 6.2)

Following this explanation, the rank of the matrix $D_{\mathbf{u}}$ of the the quadratic field and the two low magnetic fields of previous section 6.2 is $K = 4$ for all the cases. In order to prove that the algorithm works similarly with a $K = 4$, some figures will be shown below. The technique of removing half of the k-space samples and windowing the

signal $S(\mathbf{k_x})$ that was applied in the previous section 6.2 to improve the object retrieved is avoid in the following experiments, so that the effect of varying K can be better visualised.
First we focus on the example of the square in the low gradient field along x-direction (third image of 6.2). In figure 6.12, the object retrieved using the nonuniform Fourier transform algorithm with $K = 1$, $K = 2$ and $K = 4$ is shown. When the approximation matrix A_K has rank one, $K = 1$, the object differs from the one when $K = 15$. The object retrieved starts to look alike when the nonuniform Fourier matrix is approximated with a two-rank matrix ($K = 2$). When $K = 4$, the *nufft()* reaches the same quality as in the $K = 15$ case (left image of figure 6.14) and thus the number of operations can be reduced by almost four times.

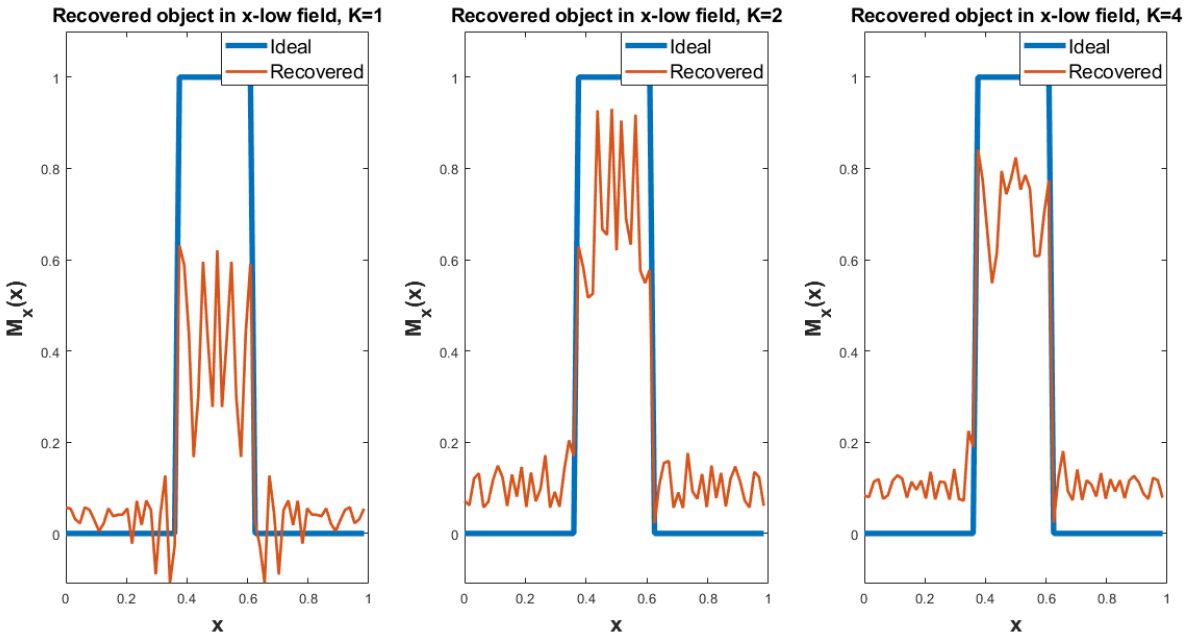

Figure 6.12: From left to right, square object in a low gradient field along x-direction (third image in figure 6.2) retrieved using *nufft()* with $K = 1$, $K = 2$ and $K = 4$

The second example is the square object in the low gradient field along y-direction (fourth image of 6.2). Figure 6.13 shows the cases with $K = 1$, $K = 2$ and $K = 4$. The results are the same as the previous case and with just a four rank matrix we achieved the same performance as with $K = 16$ (right image of figure 6.14).
In order to see another example with the quadratic magnetic field, the reader is referred to subsection A.2.1.

It was empirically checked that using the criteria $\sigma_i \geq 0.02\sigma_1$ to truncate the matrices $D_{\mathbf{u}}$ and $D_{\mathbf{v}}$ to the number of nonzero singular values was appropriate. Moreover, note that the parameter K is computed in the step 3 in section 5.2.1, which is part of the planning stage. Therefore, it is computed only once and it does not depend on the object that is being scanned. Just the magnetic field is required in order to obtain the optimal value of K. Since we already know that $K = 4$ for the quadratic and low-fields is enough, this value can be fixed for the following experiments.

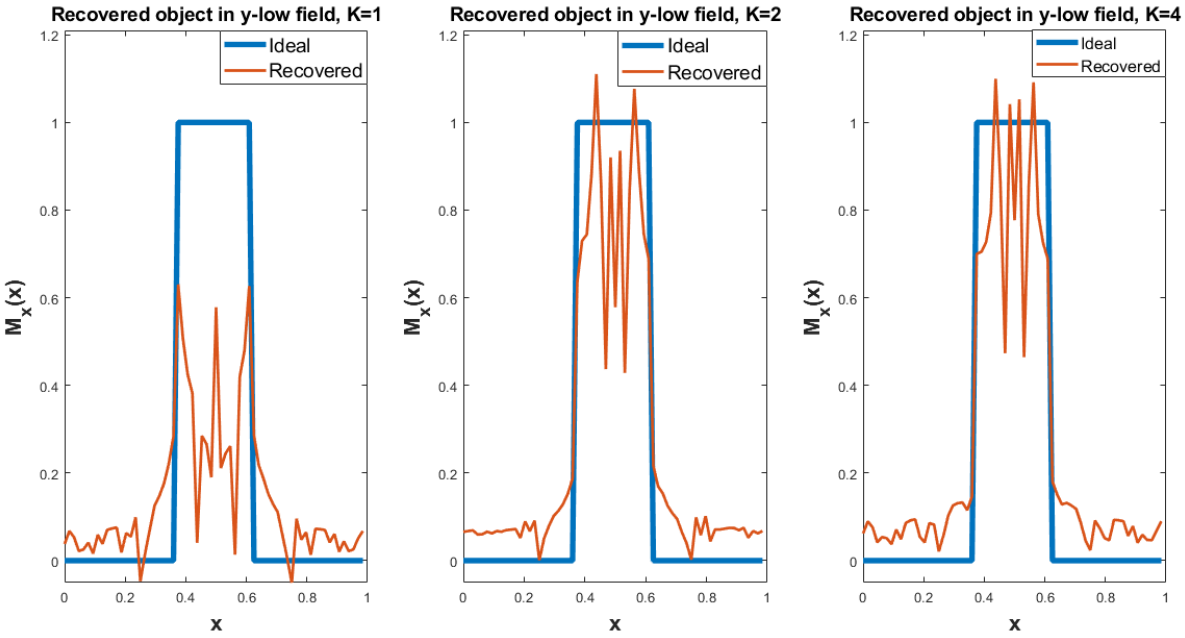

Figure 6.13: From left to right, square object in a low gradient field along y-direction (fourth image in figure 6.2) retrieved using *nufft()* with $K = 1$, $K = 2$ and $K = 4$

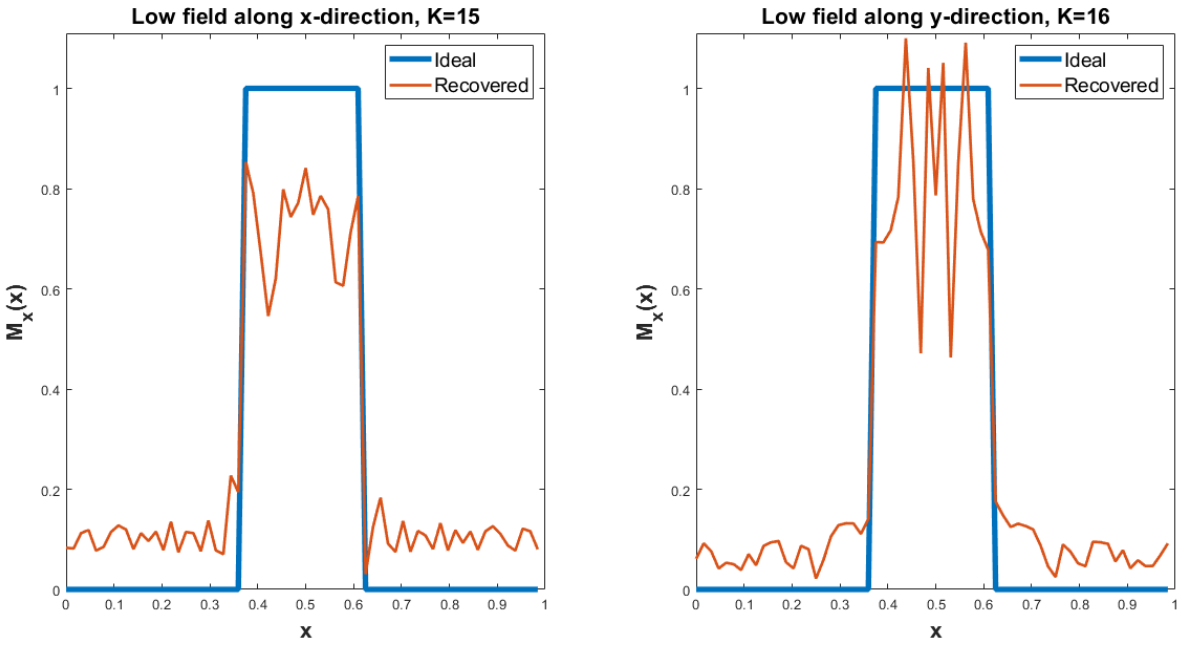

Figure 6.14: From left to right, square object retrieved from a low gradient field along x-direction (third image in figure 6.2), and from a low gradient field along y-direction (fourth image in figure 6.2), using *nufft()* with $K = 15$ and $K = 16$ respectively

6.4. Time Costs

The following experiments are focused on the time spent on the nonuniform algorithm with respect to the uniform case. The measurements were carried out in a laptop with the following characteristics: Operative system is Windows 10, 64 bits, version 1903. The CPU is Intel® Core™ i7-4510U at 2GHz. The RAM memory is DDR3, 16GB.
The dependence on some parameters such as the number of samples or the working precision will be shown in subsection 6.4.1. Then the time to implement the approximation of the nonuniform algorithm will be measured in subsection 6.4.2.

6.4.1. Parameter Dependence

The computational time of the nonuniform algorithm changes when modifying some parameters such as the number of samples N and the working precision ϵ, on which the integer K to select the rank of the approximation matrix depends (equation (3.16)).
The time values in tables 6.1 and 6.2 are computed with the average of ten thousand iterations. The time measured for the *nufft()* includes the whole algorithm process, these are from step 1 to 7, described in section 5.2.1.
Table 6.1 shows the time spent computing the conventional *fft()*. Each column corresponds to a different number of samples, from left to right: 64, 1024 and 16384 respectively. The more samples used, the more time spent computing the FFT.
The time costs are higher when the samples are not equally spaced. This is when the object is placed in a low magnetic field. The time costs grow as the K parameter increases (i.e. working precision decreases). This is represented in table 6.2.
Table 6.3 shows the ratio $\frac{\text{time spent on } nufft()}{\text{time spent on } fft()}$. It goes from 45 times when $N = 2^{14}$ and $K = 7$ to 235 times when $N = 2^6$ and $K = 16$. Note that the time costs from this table do not correspond to the computational cost $\mathcal{O}(KN \log N)$, because, as said before, the whole process of the nonuniform algorithm is measured.

Table 6.1: Time [ms] spent on *fft()* algorithm, depending on the number of samples N

	$N = 2^6$	$N = 2^{10}$	$N = 2^{14}$
Time [ms]	0.0071	0.024	0.3021

Table 6.2: Time [ms] spent on *nufft()* algorithm, depending on the number of samples N and the working precision ϵ in a low magnetic field

Working precision	$N = 2^6$	$N = 2^{10}$	$N = 2^{14}$
$\epsilon = 9.8\text{e}{-4}, \quad K = 7$	0.65	1.43	13.51
$\epsilon = 1.2\text{e}{-7}, \quad K = 10$	0.74	1.70	20.5
$\epsilon = 2.22\text{e}{-16}, \quad K = 16$	0.90	2.13	28.57

Table 6.3: Time ratio spent on *nufft()* algorithm in a low-field with respect to time spent on *fft()*, depending on the number of samples N and the working precision ϵ

Working precision	$N = 2^6$	$N = 2^{10}$	$N = 2^{14}$
$\epsilon = 9.8\text{e}{-4}, \quad K = 7$	169	62.5	44.72
$\epsilon = 1.2\text{e}{-7}, \quad K = 10$	193	70.83	67.86
$\epsilon = 2.22\text{e}{-16}, \quad K = 16$	235.2	88.75	94.57

6.4.2. NUDFT Algorithm Implementation

This section focuses on the time that the operation $\tilde{F}_2\mathbf{c}$ (equation (3.15)) takes. In other words, measuring the time of the online stage, which are steps six and seven of section 5.2.1.

The sequences $\mathbf{s}$, $\mathbf{t}$ and the parameters δ, K are assumed to be known, and the matrices $D_{\mathbf{v}}$ and $D_{\mathbf{u}}$ are already computed. The magnetic field is the gradient field along x-direction, third image in figure 6.2, and the object is the square in figure 6.1.
The time that the operation $\tilde{F}_2\mathbf{c} = (A \circ F)\mathbf{c} \approx (A_K \circ F)\mathbf{c}$ takes for different values of K can be visualised in figure 6.15. The integer $K = 1$ refers to the uniform Fourier transform, i.e. just one FFT is done. The other three values, $K = 7, K = 10$ and $K = 16$, are calculated with equation (3.16) and they correspond to half, single and double precision respectively. Recall that this operation costs K FFTs, i.e. $\mathcal{O} = KN \log N$. For a low number of samples, around $N = 2^6$, the curves for the different K values are very close. When the number of samples increases, the curves start to separate.

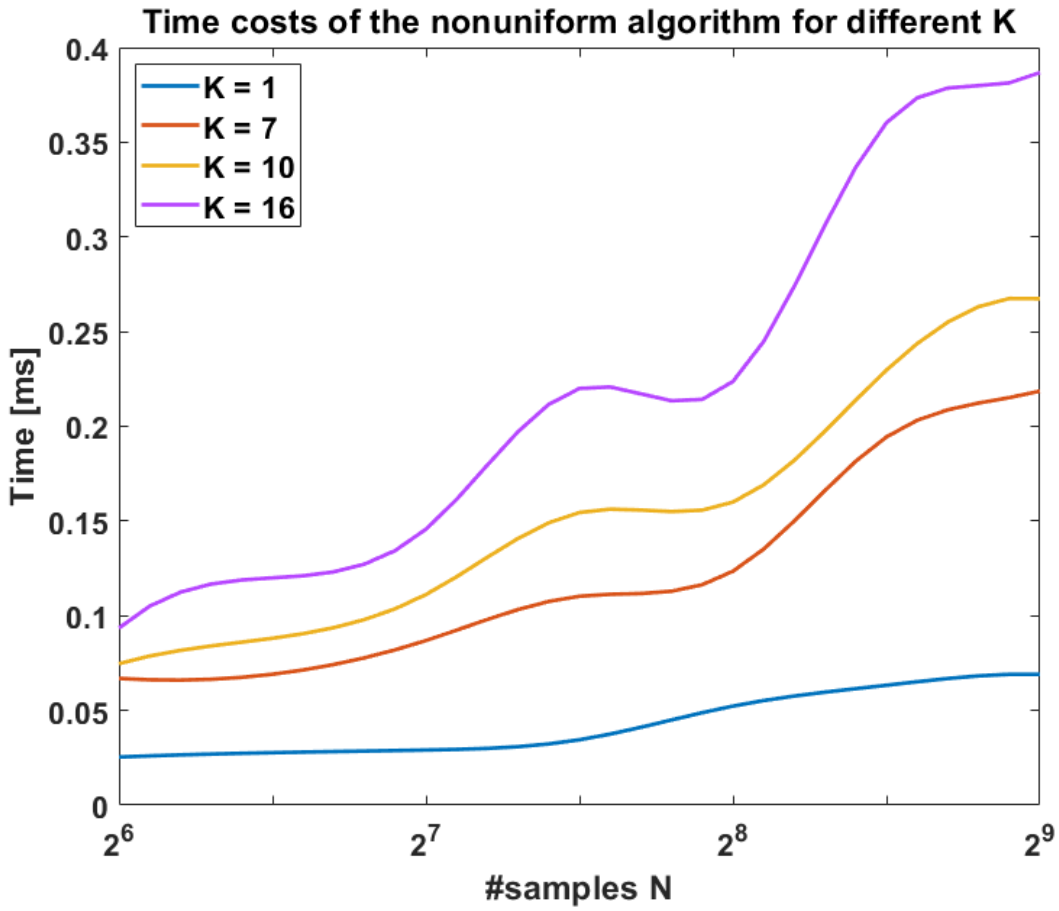

Figure 6.15: Time [ms] spent on the uniform FFT ($K = 1$) and on the NUFFT for $K = 7$, $K = 10$ and $K = 16$, with different number of samples N

Figure 6.16 shows the time spent when $K = 16$ and when $K = N$, where N is the number of samples. Mentioned figure represents how much time is saved when matrix A in equation (3.15) is approximated to a low rank matrix. It can be seen in this figure that the higher the number of samples, the more computational time is saved. For instance, when the number of samples is 2^8, using the approximation matrix takes around sixteen times less than computing the whole matrix. The results are identical because the rank of the two approximation matrices is the same, as explained in section 6.3.

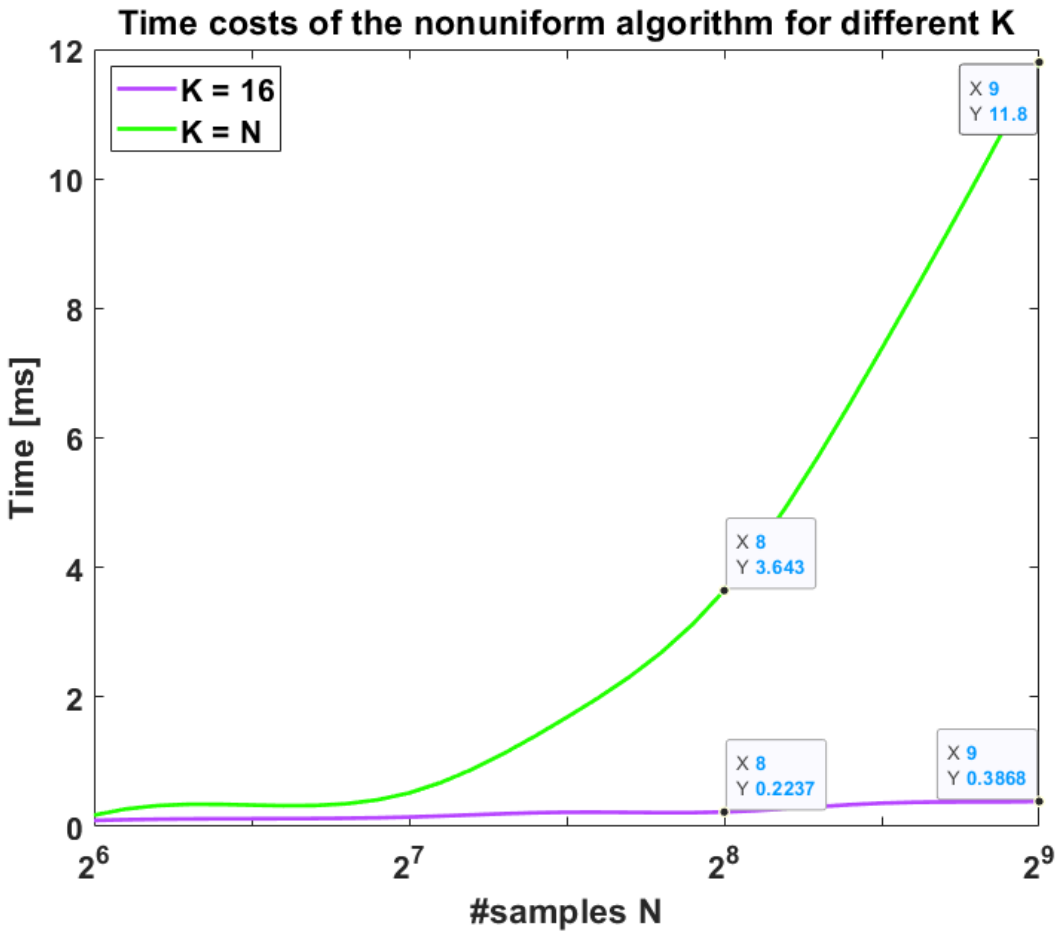

Figure 6.16: Time [ms] spent on the NUFFT for $K = 16$ and $K = N$ and different number of samples N

7

CG and NUFFT in one dimension

In this chapter, an iterative solver, the Conjugate Gradient method, will be employed in order to retrieve the object from the low-field MRI in one dimension.
The structure will be the following. In section 7.1, a brief introduction is given. In section 7.2, the results of this iterative algorithm are shown. In the next section 7.3, the performance of the Conjugate Gradient throughout the iterations and its convergence will be analysed.

7.1. Introduction

The results that will be seen in the following sections of this chapter are focused on the performance of the Conjugate Gradient method on our particular problem of retrieving an object from a nonlinear field.
The aim is to retrieve the object M_x from the one dimensional MRI signal, i.e. $S(\mathbf{k_x}) = \tilde{F}_1 M_x(\mathbf{x})$. Since the field is not linear, an inverse Fourier transform cannot be applied and the CG method is used.
The Conjugate Gradient method is explained in sections 4.2.2 and 5.1. The CG solves for M'_x in

$$(F_1 F_1^*) M'_x(\mathbf{x}) = S(\mathbf{k_x}) \tag{7.1}$$

Where the object is obtained by applying an NUFFT-II to the solution of the CG, i.e.

$$M_x = \text{conj}\big(\tilde{F}_2 \text{conj}(M'_x)\big) \tag{7.2}$$

.

7.2. Retrieving the Object

The results in this section are obtained using the Conjugate Gradient and the nonuniform Fourier transform algorithms explained in chapter 5 in an MRI signal from a square object, figure 6.1, in the last two fields of figure 6.2. These are the fields from one slice of the gradient maps of the low-field MRI scanner in Leiden University Medical Center, described in [27]. The number of samples used is $N = 64$ and the working precision is double, i.e. $\epsilon = 2.22\text{e}{-16}$, $K \approx 16$. The number of iterations of the Conjugate Gradient is fixed to $R = 50$.
Subsection 7.2.1 shows the results from the field that the gradients along the x-direction create in the low-field scanner, third image in figure 6.2, and subsection 7.2.2 shows the results from the field created from the gradients along the y-direction, last image in figure 6.2. The reader is referred to subsection A.2.2 to see the results from the quadratic field, second image in figure 6.2.

7.2.1. Low Magnetic Field along x-direction

Figure 7.1 shows the results of applying the CG in the signal from the field created by the gradients along x-direction in the low-field MRI. The square is properly recovered.
In the left image of figure 7.2, the object recovered from a signal with half of the k-space samples can be visualised. With just one iteration of the Conjugate Gradient, the result with half of the k-space improved (left image of figure 6.10). Nevertheless, when there are more iterations, the performance of the CG is better with the full k-space.
Why the performance is worse when the upper half of the k-space is eliminated is understood looking at equation (4.11). The CG solves for M'_x and then the nonuniform Fourier transform has to be applied in order to retrieve the object, i.e.

$$M_x = \text{conj}\big(\tilde{F}_2 \text{conj}(M'_x)\big) \tag{7.3}$$

The nonuniform matrix $\tilde{F}_2$ is a tall matrix of size $N \times N/2$, where N is the number of samples, since the right half of the columns are removed in order to eliminate half of the k-space (recall that $\tilde{F}_1 = \tilde{F}_2^T$). This leads to an overdetermined system of equations, with more equations than unknowns. Moreover, eliminating the upper half of the k-space samples is equivalent to low-pass filtering the signal. The high frequencies which contain the details are eliminated and only the low frequencies are kept. The signal is dominated by low-frequencies that give the overall shape of the object [13]. Therefore, although the number of iterations of the CG can be increased, this will not give a better solution.
Regarding the right image of figure 7.2, it shows the result when the approximation matrix A_K of the nonuniform Fourier transform is lowered[1] from rank $K = 15$ to the rank $K = 4$. Taking the four highest singular values corresponds to low-pass filtering the signal. As said before, the details were in the high frequencies and therefore, increasing the number of iterations of the CG will not improve the solution of the right image of figure A.12.

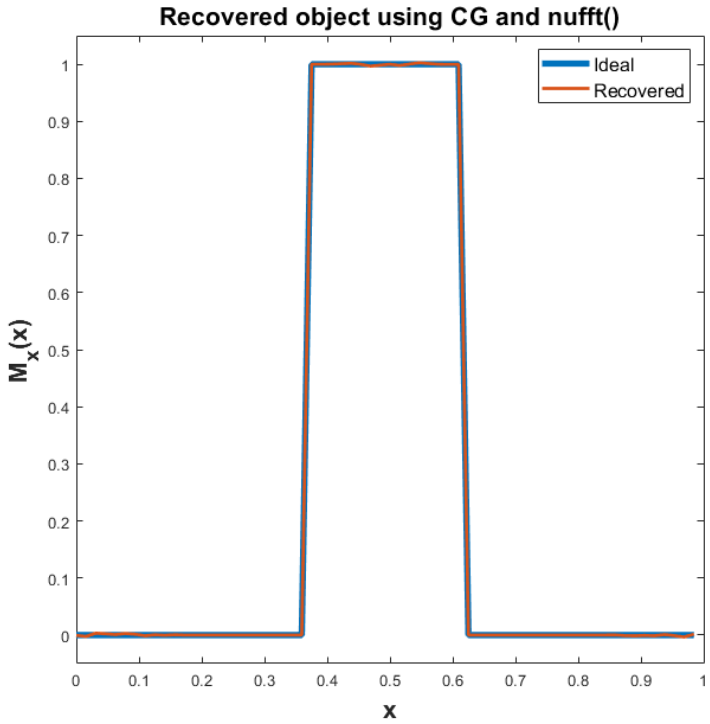

Figure 7.1: Object recovered $M_x(x)$ from a low-field along x-direction (third image of figure 6.2) using 50 iterations of the CG and the NUFFT

[1] See section 6.3 for more details.

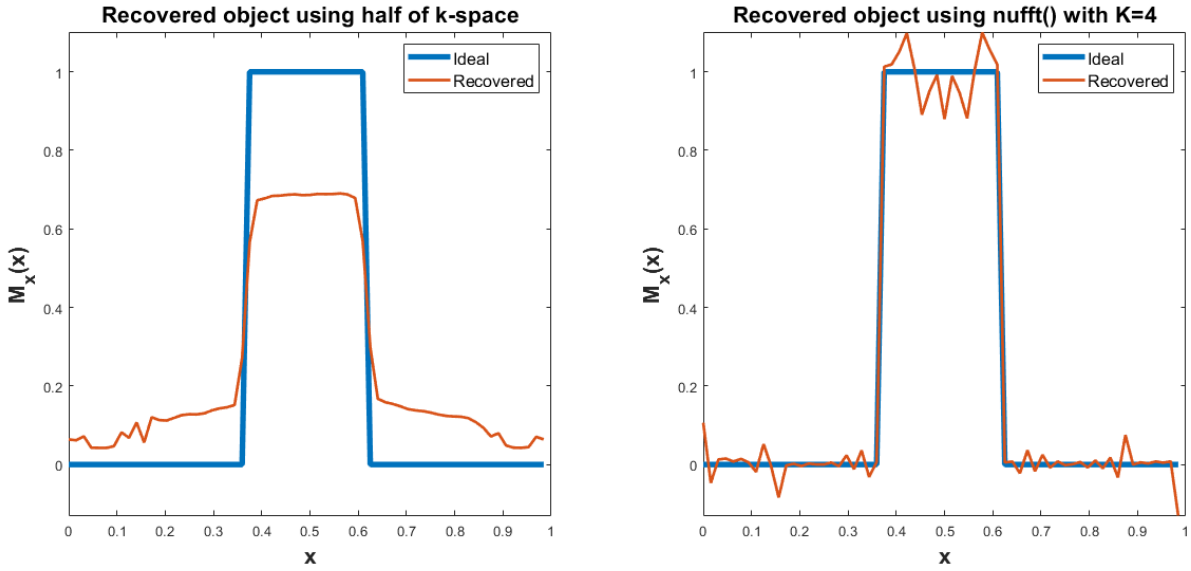

Figure 7.2: Object recovered $M_x(x)$ from a low-field along x-direction (third image of figure 6.2) using 50 iterations of the CG and the NUFFT. To the left, half of the k-space samples were used. To the right, the *nufft()* with $K = 4$ was used

7.2.2. Low Magnetic Field along y-direction

Figure 7.1 shows the results of applying the CG in the signal from the low-field along y-direction. The square is properly recovered.

In the left image of figures 7.4, the result of using half of the k-space is visualised. Like the previous case in subsection 7.2.1, the object recovered differs from the ideal, due to the same reason. Similar results are obtained when the rank of the approximation matrix is reduced to $K = 4$. This can be seen in the right image of figure 7.4.

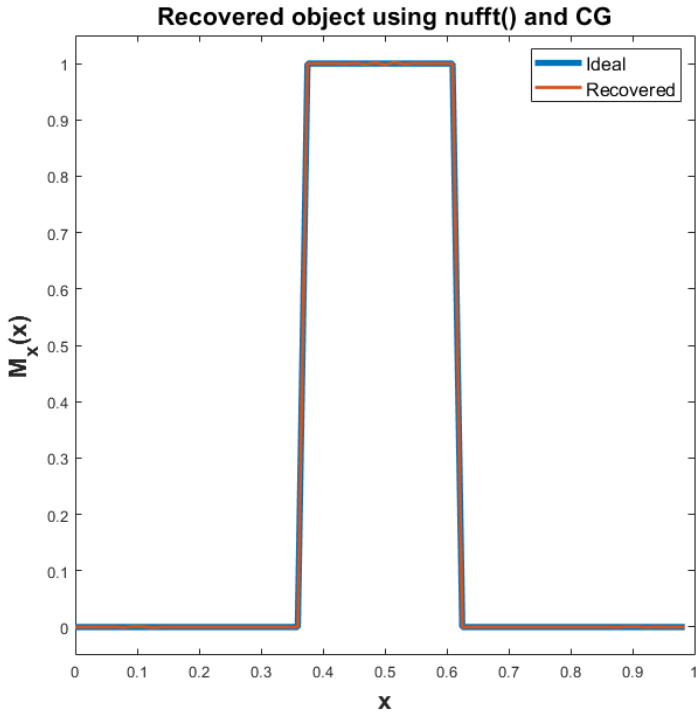

Figure 7.3: Object recovered $M_x(x)$ from a low-field along y-direction (fourth image of figure 6.2) using 50 iterations of the CG and the NUFFT

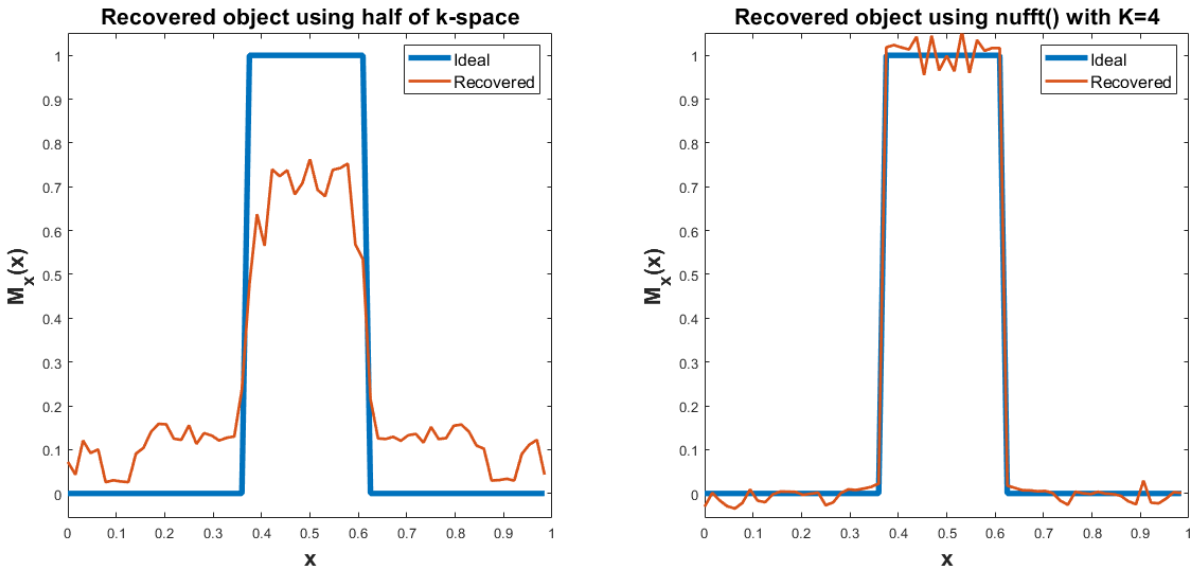

Figure 7.4: Object recovered $M_x(x)$ from a low-field along y-direction (fourth image of figure 6.2) using 50 iterations of the CG and the NUFFT. To the left, half of the k-space samples were used. To the right, the *nufft()* with $K = 4$ was used

7.3. Performance through Iterations

In the previous section 7.2, the number of iterations of the Conjugate Gradient method was fixed to $R = 50$. Computational time can be saved if this number is reduced. Nevertheless, decreasing the number of iteration R results in a worse performance of the algorithm and in a less accurate solution. Therefore, in this section, the trade-off between computational time and accuracy will be studied, focusing on the low-fields.
First two terms are defined, these are residual and error. The residual determines how far we are from the correct value of the signal $S(\mathbf{k_x})$. It is divided by the L2-norm of the signal to obtain the relative residual, i.e.

$$r_{\text{rel}} = \frac{\|\mathbf{S} - \left(\tilde{F}_1 \tilde{F}_1^*\right) \mathbf{M}'_x\|_2}{\|\mathbf{S}\|_2}. \tag{7.4}$$

The error represents how much the solution of the algorithm differs from the ideal object. It is divided by the L2-norm of the ideal object to compute the relative error as

$$e_{\text{rel}} = \frac{\|\mathbf{M}_x^{\text{ideal}} - \mathbf{M}_x^{\text{retrieved}}\|_2}{\|\mathbf{M}_x^{\text{ideal}}\|_2}. \tag{7.5}$$

In the following subsections 7.3.1 and 7.3.2 the convergence of the residual and the error will be seen.

7.3.1. Convergence of the Residual

This subsection is focused on the convergence of the Conjugate Gradient looking at the residual. Moreover, the convergence of the full k-space case will be compared to the one for half of the k-space and when using a lower K rank matrix. These cases were explained in the previous section 7.2.

Figure 7.5 shows the relative residual, equation (7.4), when performing 25 iterations to 60. The left image corresponds to the low magnetic field that the gradients along the x-direction generate, this is the third image of figure 6.2, and $K = 15$. The right image corresponds to the low magnetic field along the y-direction, which is the last image of figure 6.2, and $K = 16$. The indicated points show the residuals when doing 30, 40 and 50 iterations of the CG. The difference of the residuals from 30 to 40 iterations is bigger than the difference between 40 and 50. From 50 iterations on, the residual stabilises.

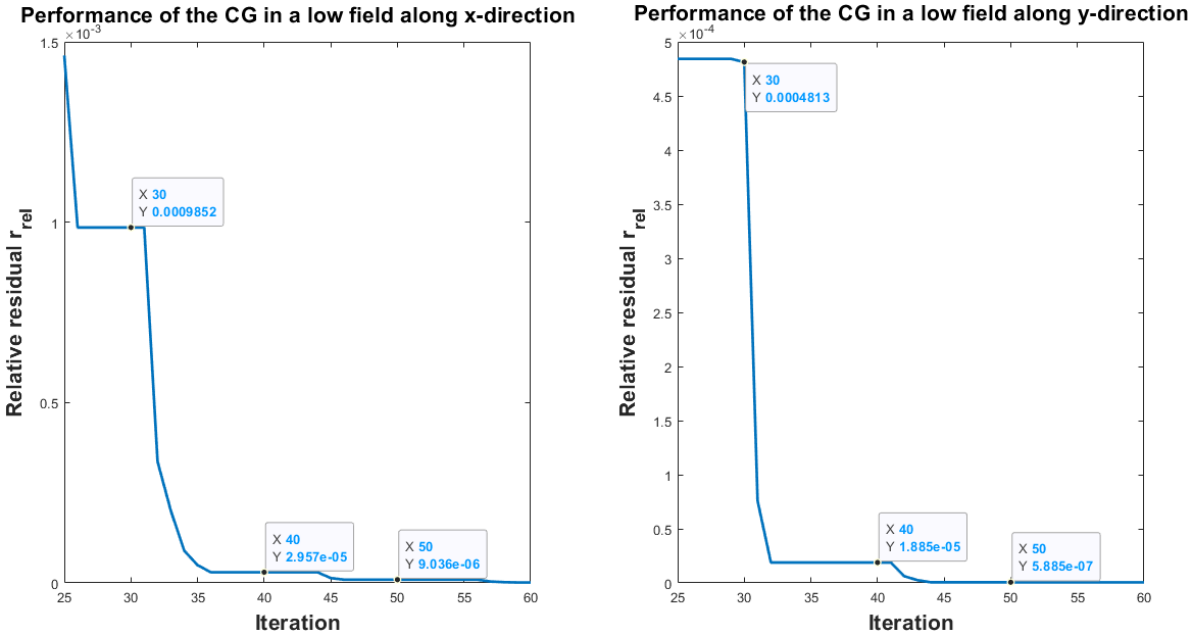

Figure 7.5: Relative residual computed from 25 to 60 iterations of the Conjugate Gradient method. The left image corresponds to the low-field along x-direction and the right image to the low-field along y-direction

The reconstructions corresponding to 30, 40 and 50 CG iterations can be seen in the images of the next figures, from left to right respectively. Figure 7.6 is for the low-field along x-direction and figure 7.7 is the low-field along the y-direction.
By visual inspection, the difference between the three cases with different number of iterations is not very notable. The greater differences are at the beginning and at the end, around $x_i \in [0, 0.2]$ and $x_i \in [0.8, 1]$, where some peaks can be seen in the background. Moreover, the object retrieved from the field along the x-direction (figure

7.6) presents noise in the flat area of the square, at $x_i \in [0.4, 0.6]$. The peaks in the background and the noise in the square are attenuated when the number of iterations increases. Nevertheless, the number of iterations can be reduced to $R = 30$ without a great loss of accuracy.

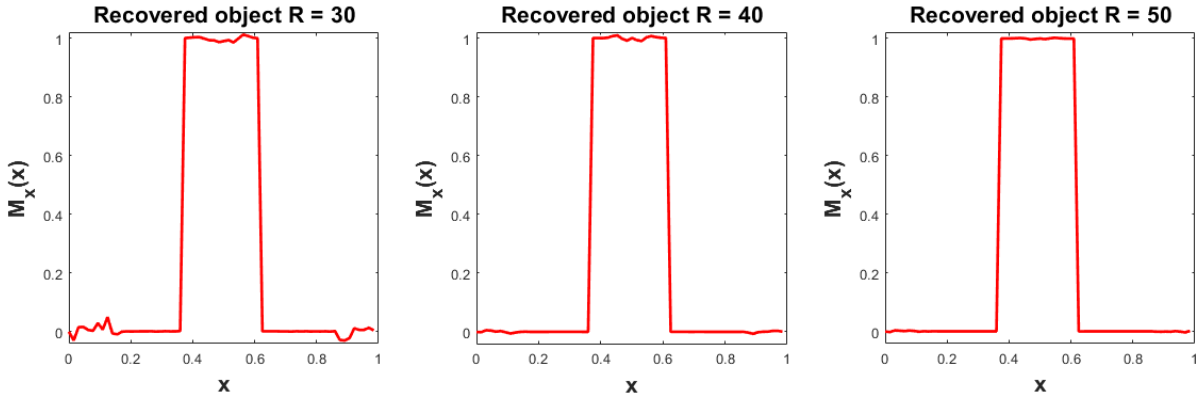

Figure 7.6: Object recovered $M_x(\mathbf{x})$ from a low-field along x-direction (third image of figure 6.2) using a different number of iterations R of the CG and $K = 15$. From left to right, 30, 40 and 50 iterations

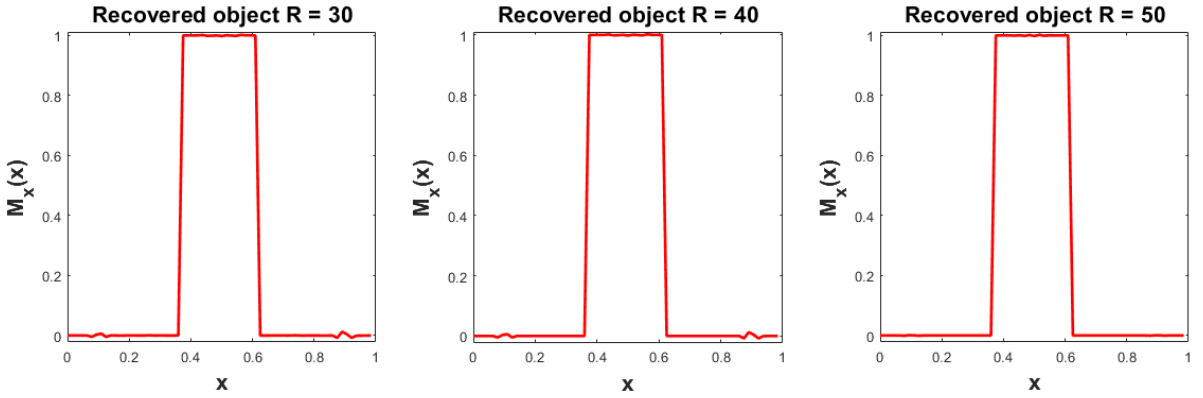

Figure 7.7: Object recovered $M_x(\mathbf{x})$ from a low-field along y-direction (last image of figure 6.2) using a different number of iterations R of the CG and $K = 16$. From left to right, 30, 40 and 50 iterations

Figure 7.8 shows the residual, from one iteration to one hundred. In addition, the residual calculated for the half k-space case and when $K = 4$ in the *nufft()* can be visualised in this figure. The left image shows the residual for the low field along x-direction and the right image the field along y-direction. In each image there are three curves: (1) blue corresponds to full k-space and $K = 15$ for field along x-direction or $K = 16$ for field along y-direction, (2) red corresponds to half k-space and $K = 15$ for field along x-direction or $K = 16$ for field along y-direction, and (3) yellow represents full k-space and small rank $K = 4$ for both fields.
For both fields, the half k-space case converges faster than the other two. Nevertheless, recall that the CG gives the solution to M_x'. To recover the object M_x, a NUFFT-II has to be applied and it was seen in the previous section 7.2 that the results worsen. Therefore, although the half k-space converges faster, it does not give a better solution than the full k-space.
Regarding the nonuniform Fourier transform algorithm with the integer K fixed to 4, the residual does not converge to zero in either of the fields. The residual stabilises after 12 iterations in the field along x-direction and in 20 in the field along y-direction. Moreover, the case of $K = 4$ is very similar to the full k-space when the number of iterations is smaller than 8 in both cases. Therefore, if the number of iterations of the CG is below 8, it is convenient to use $K = 4$ instead of $K = 15$ or $K = 16$ to save operations since the performance is the same.

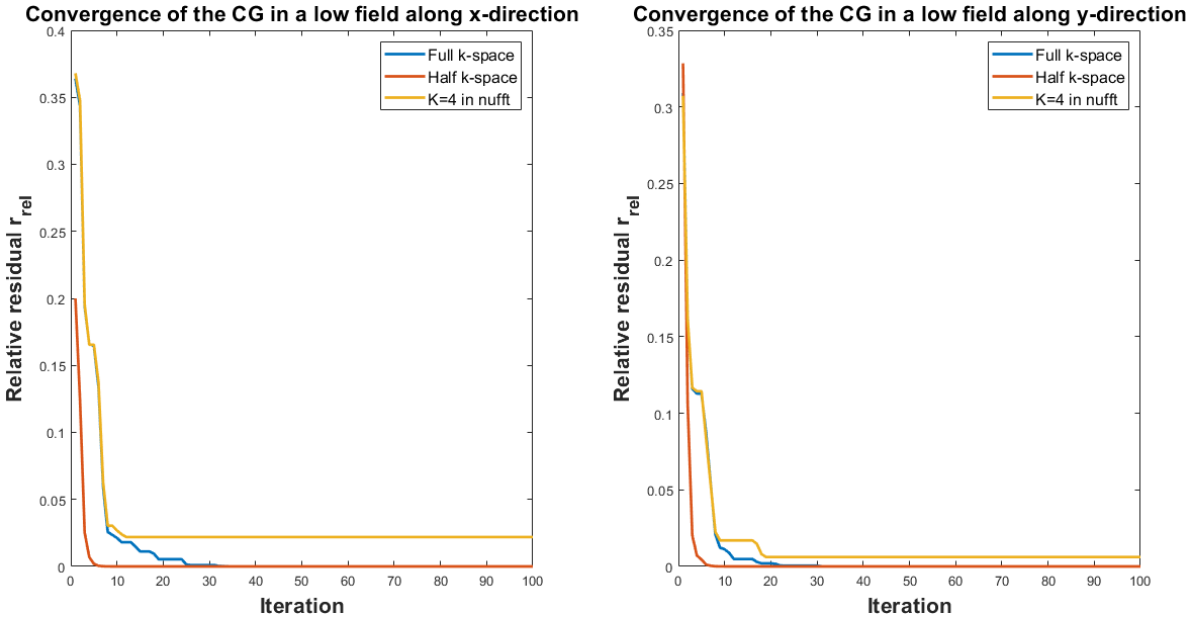

Figure 7.8: Relative residual computed from 1 to 100 iterations of the Conjugate Gradient method. The left image corresponds to the low-field along x-direction and the right image to the low-field along y-direction

7.3.2. Convergence of the Error

This subsection is focused on the convergence of the error, i.e. how much the object retrieved differs from the ideal object (equation (7.5)). Like the previous subsection 7.3.1, the convergence of the error of the full k-space case will be compared to the one for half of the k-space and when using a lower K rank matrix.

The value of the error for the low-field along the x-direction, third image of figure 6.2, through the iterations is visualised in the left image of figure 7.9. The convergence of the error for the low-field in the y-direction, fourth image of figure 6.2, is represented in the right image of figure 7.9. In each image there are three curves: (1) blue corresponds to full k-space and $K = 15$ for field along x-direction or $K = 16$ for field along y-direction, (2) red corresponds to half k-space and $K = 15$ for field along x-direction or $K = 16$ for field along y-direction, and (3) yellow represents full k-space and small rank $K = 4$ for both fields.

The error of the full k-space case converges to zero after fifty iterations in both fields. The error when fixing the integer K to a small number is similar to the full k-space if the number of iterations is small. Nevertheless, after 8 iterations in the field along the x-direction and after 17 in the field along the y-direction, the error stabilises and does not converge to zero. Therefore, if the number of iterations is small, reducing the integer $K = 15$ or $K = 16$ to $K = 4$ would save computational time giving the same results.

Figure 7.10 shows the object retrieved when the number of iterations is at the limit when the full k-space case and the reduced K case start to differ. In other words, when the maximum number of iterations is set to $R = 8$ in the low-field along x (left image of the figure 7.10), and when the maximum number of iterations is set to $R = 17$ in the low-field along y-direction (right image of the figure 7.10).

As explained in the previous sections 7.2 and 7.3.1, the worst performance is given by the half k-space case. The error does not converge to zero and it stabilises after $R \approx 5$ iterations in both fields.

To summarised this section 7.3, in order to obtain the best performance when employing CG is to use the full k-space. If the number of iterations is small, the rank can be lowered to $K = 4$. Otherwise, if the number of iterations increases, the rank must be higher such as $K = 16$.

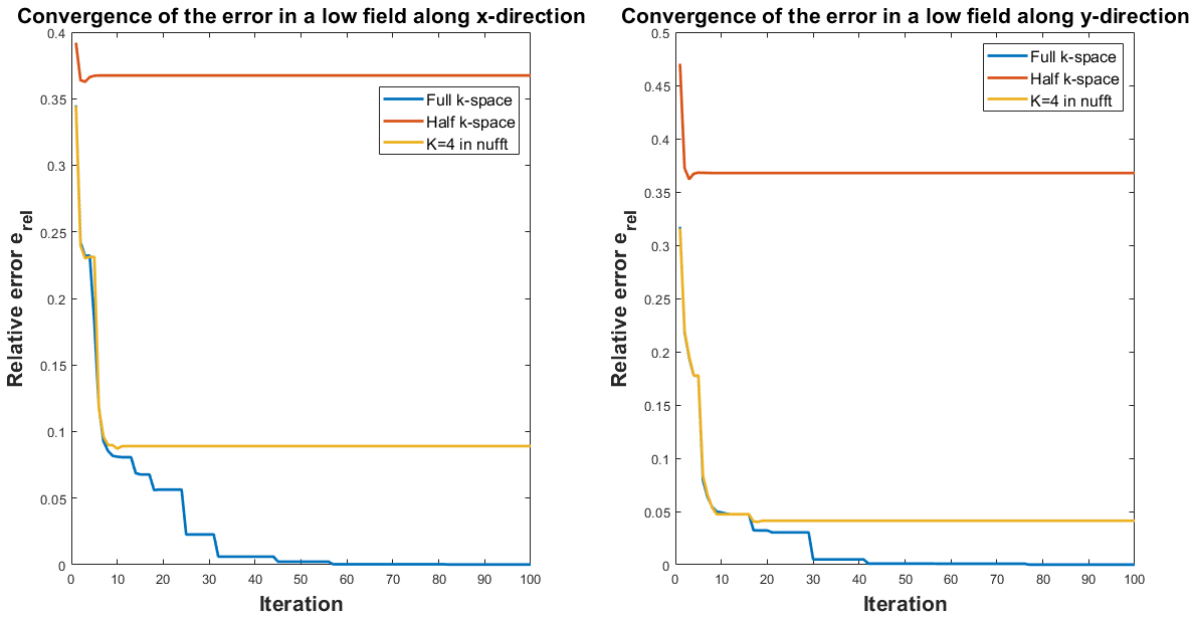

Figure 7.9: Relative error computed from 1 to 100 iterations. The left image corresponds to the low-field along x-direction and the right image to the low-field along y-direction

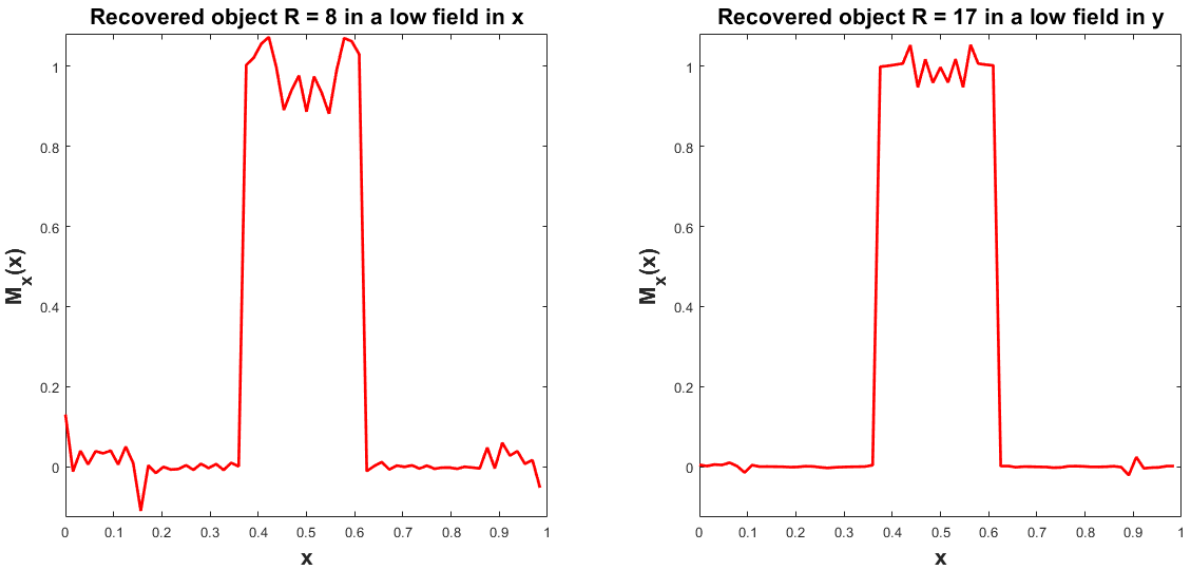

Figure 7.10: To the left, recovered object $M_x(\mathbf{x})$ from a low-field along x-direction using $R = 8$ iterations of the Conjugate Gradient and the rank of the nonuniform Fourier matrix is $K = 4$. To the right, recovered object $M_x(\mathbf{x})$ from a low-field along y-direction using $R = 17$ iterations of the Conjugate Gradient and the rank of the nonuniform Fourier matrix is $K = 4$

8

NUFFT in Two Dimensions

This chapter focuses on one iteration of the Conjugate Gradient method, which is equivalent to directly apply the nonuniform fast Fourier transform algorithm described in chapter 3 to the two-dimensional received signal. Thus, it is expected to obtain poor quality results, as it was seen in chapter 6 for one dimension. The main objective in this chapter is to measure the time costs of the mentioned algorithm.
The chapter has been organised in the following way. It starts with an introduction in section 8.1. In section 8.2, the results of using the 2D NUFFT are presented and discussed. Section 8.3 shows the performance of the algorithm varying the working precision. The fourth section 8.4 is concerned with the time costs of the 2D nonuniform fast Fourier transform.
Regarding section 8.2, where the results of the research are presented, the outline is summarised below.

- A brief explanation of how the nonuniform fast Fourier transform algorithm works for a square object and a low magnetic field is given. In other words, how the $\mathbf{s}$ and $\mathbf{t}$ sequences are generated (steps 1, 2 and 3 of subsection 5.2.2). The value of the parameters δ and K, equations (3.17) and (3.18), which corresponds to steps 4 and 5 of subsection 5.2.2. And last, the construction of the matrices $D_{\mathbf{u}}$ and $D_{\mathbf{v}}$ (step 6 of subsection 5.2.2).
- The object retrieved using the conventional 2D fast Fourier transform algorithm *fft2()* and the object retrieved using the nonuniform fast Fourier transform algorithm *nufft2()* are compared.
- Finally, a priori information is used to improve the results.

8.1. Introduction

The results that will be shown along this chapter will be focused on the two-dimensional nonuniform Fast Fourier transform algorithm. It will be explained how the 2D NUFFT algorithm based on [5] works and the time that it costs will be measured.
In this chapter, one iteration of the Conjugate Gradient will be performed. One iteration of the CG is equivalent to apply the 2D NUFFT-II to the conjugate of the received signal and then take the conjugate of the result, see section 7.1 for more details. In other words, this is

$$M_{xy} = \text{conj}\left(\tilde{F}_2^y \text{conj}\left(S(k_x, k_y)\right)\tilde{F}_2^x\right). \tag{8.1}$$

The algorithm of the 2D nonuniform Fourier transform of type two was described in sections 3.6 and 5.2.2.

8.2. Retrieving the Object

Figure 8.1 show the low magnetic fields generated from the gradients along the x- and y-direction from the low-field scanner of LUMC. They are used on the object of figure 8.2. The number of samples is $m \times n = 64 \times 64$ and the working precision is double, $\epsilon = 2.22\text{e}{-16}$.

Since the object scanned is real, its Fourier transform presents conjugate symmetry and half of the k-space could be estimated. In order to try to improve the quality of the object retrieved, we will check whether eliminating some samples of the k-space gives better results, as it was done in section 6.2 with one dimension. Figure 8.3 represents the samples that will be remove with the pink colour.

The reader is referred to the appendix B to see more 2D examples with different fields.

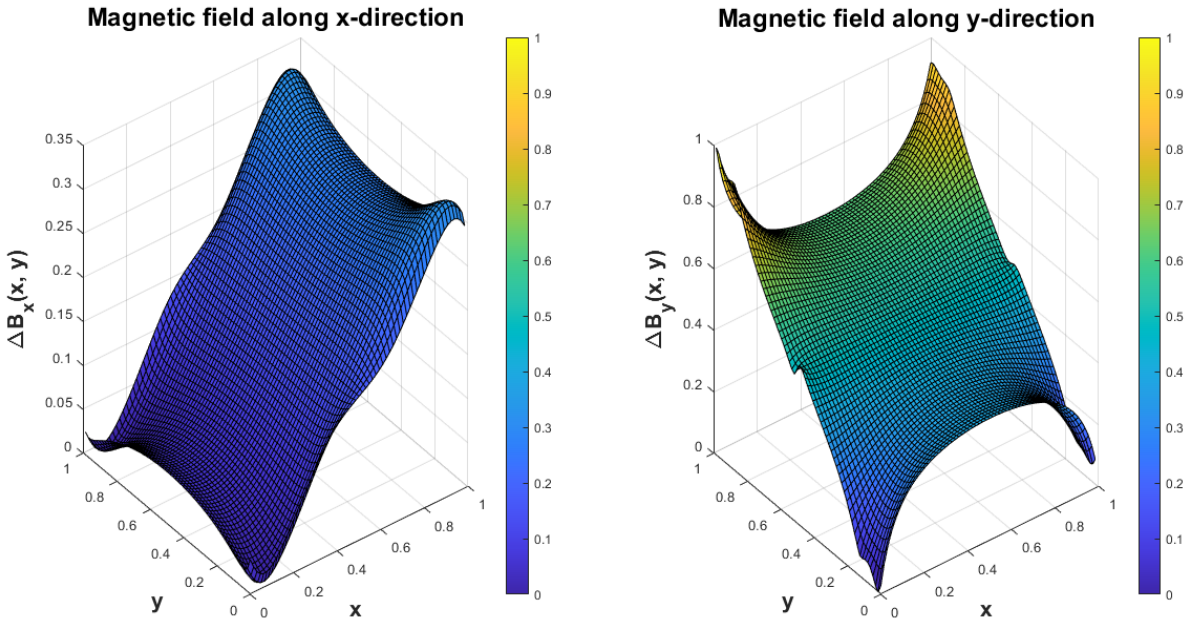

Figure 8.1: Gradient fields from LF-MRI LUMC scanner in both x- and y-directions

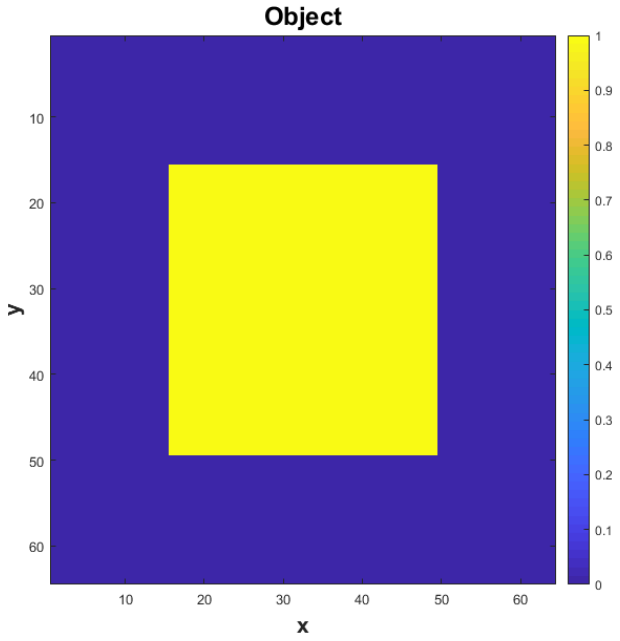

Figure 8.2: Square shaped object that is used in different magnetic fields

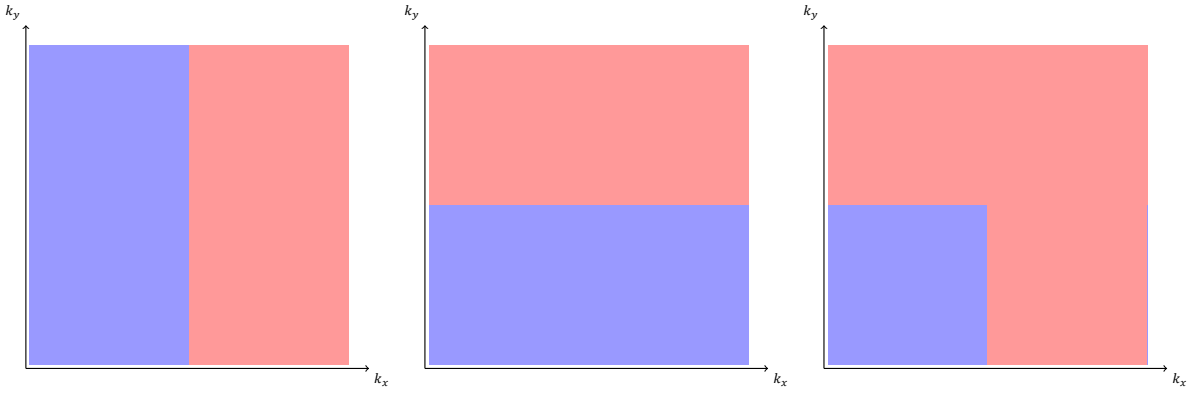

Figure 8.3: Removing k-space samples. The pink part represents the samples eliminated, from left to right, (1) upper half of k_x-space, (2) upper half of k_y-space and (3) both upper halves of k_x- and k_y-space, i.e. only a quarter of the k-space samples remains

8.2.1. Low Magnetic Field

The gradient fields ΔB_x or ΔB_y shown in figure 8.1 are not constant in any direction. These are the only fields that present this characteristic among all the example fields that are presented in the appendix B.
Figure 8.4 shows the x and y **t** sequences. Their respective **s** sequences are equal except for a node in the gradient field along the y-direction, at $(x = 0, y = 1)$. The perturbation parameters are $\delta^x = 0.4999$ and $\delta^y = 0.4998$, and both give $K = 14$. We will see in section 8.3 whether this integer can be reduced.

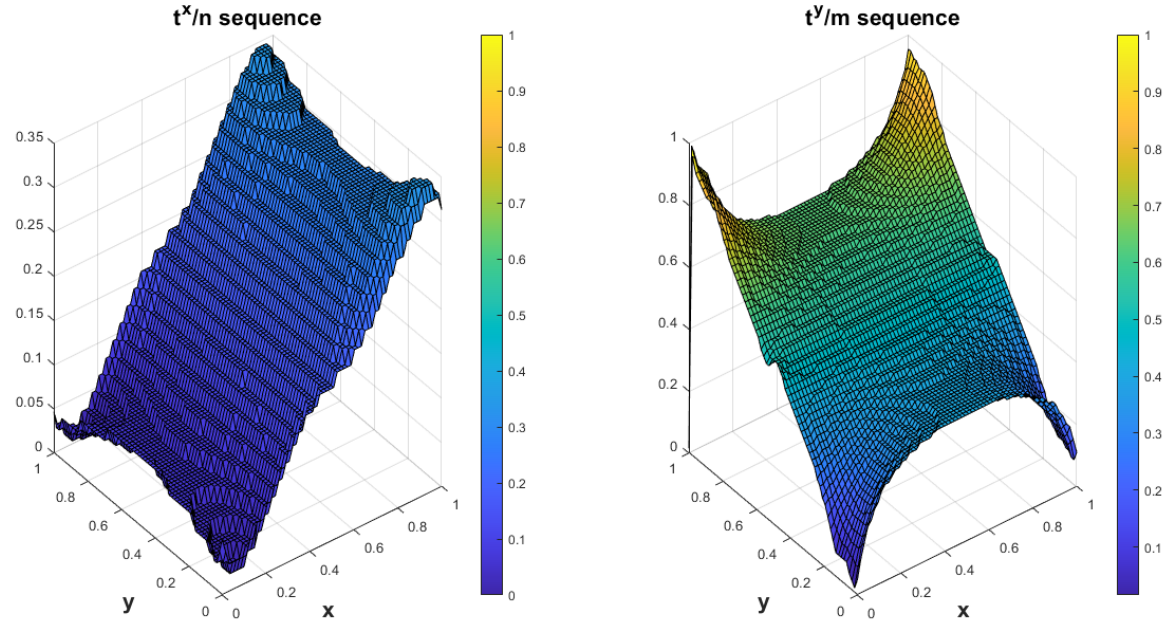

Figure 8.4: Sequences t^x/n and t^y/m generated from the low gradient fields of figure 8.1

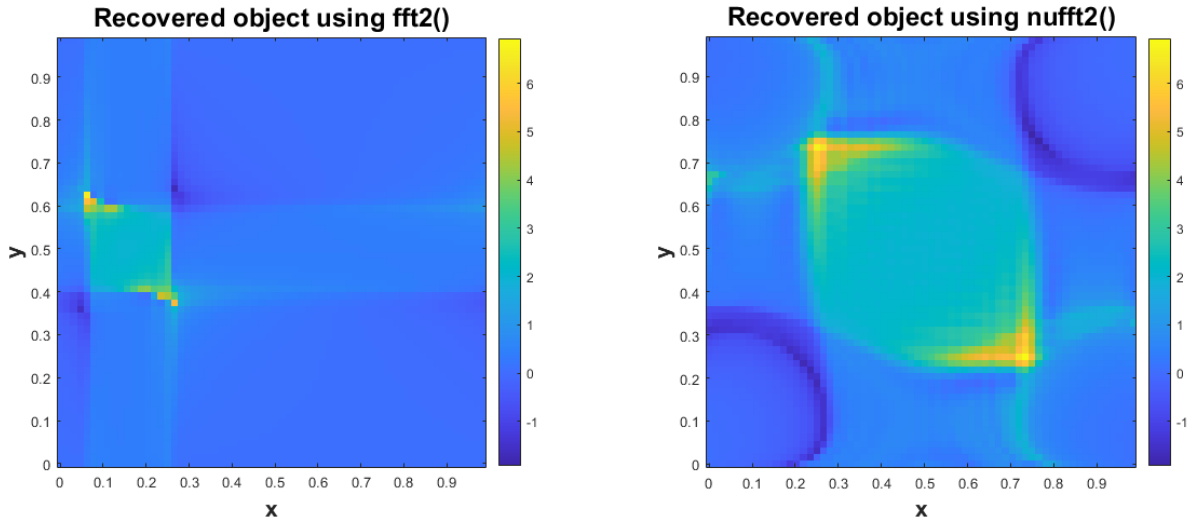

Figure 8.5: To the left, recovered square object from the magnetic fields of the LF-MRI of LUMC (figure 8.1) using the Fourier transform algorithm, *fft2()*. To the right, same object recovered using the nonuniform Fourier transform algorithm, *nufft2()*

The two images of figure 8.5 represent the object retrieved from the low magnetic fields using the *fft()* and *nufft()*, respectively.
Focusing on the left image of figure 8.5, the conventional Fourier transform displaces the object to the left in the x-direction and shrinks the square in both x- and y-directions. The object is moved to the left, to the interval $x \in [0.8, 0.25]$, because the highest value of the magnetic field ΔB_x is $\Delta B_x(r_i) \approx 0.35$. This means that the field is under the linear plane and it introduces a spatial delay.

Regarding the reduction of the size of the square in the y-direction, it is due to the shape of the ΔB_y field right on the square (figure 8.6). The amplitude of the field in this part is in the interval $\Delta B_y(r_i) \in [0.4, 0.6]$ and this is where the retrieved object is placed using the uniform FFT. The same happens with the width of the square along x-direction.

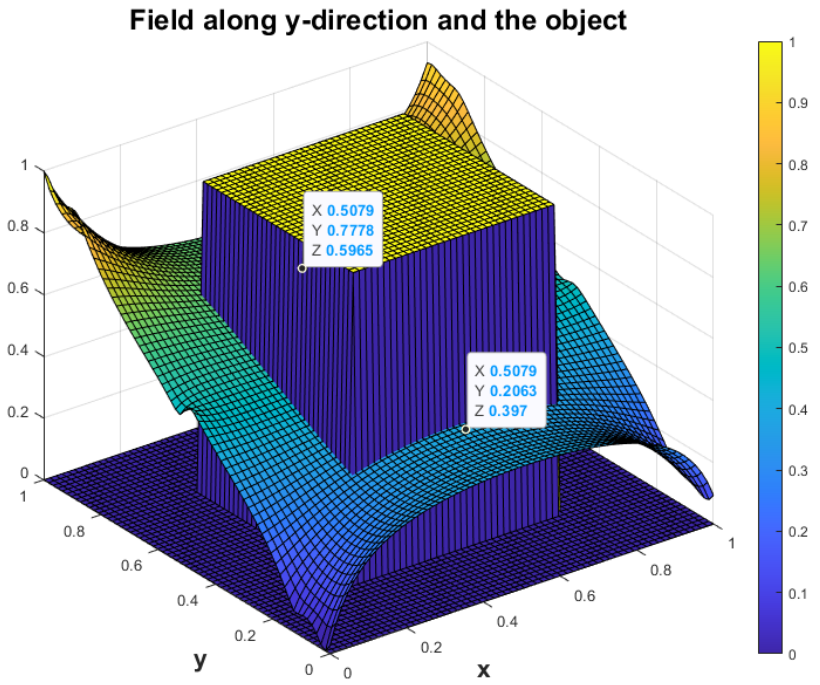

Figure 8.6: Low gradient field along y-direction (right image of figure 8.1) and the ideal object

Respecting the nonuniform Fourier transform, right image of figure 8.5, the results show the square rounded. Note that there are no horizontal lines because the y-field on the object is more linear than the case with the y-field approximation in section B.3. On the other hand, now four small circles appear in the background at the four corners of the object retrieved. These circles are due to the arc shape of the fields. In the x-field the arc can be seen in the line $x = 0$ and in the line $x = 1$, while in the y-field these arcs can be seen in the line $y = 0$ and the line $y = 1$.
The next figure 8.7 shows the object retrieved eliminating the higher frequencies in the k-space. Nevertheless, this technique does not improve the results.

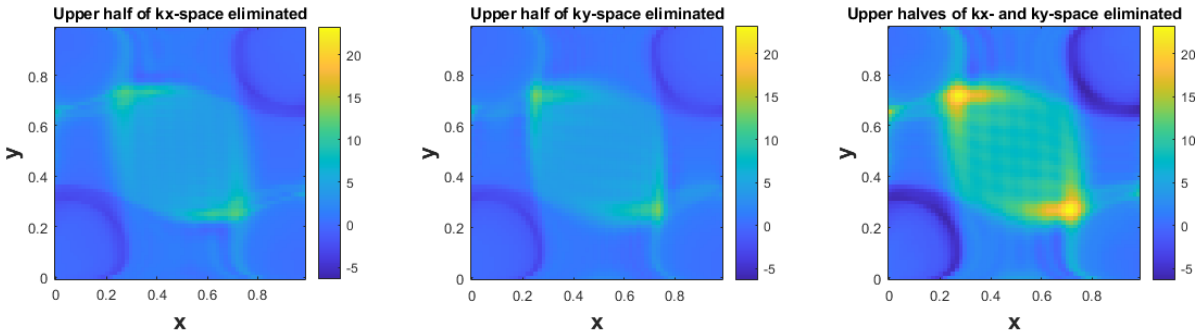

Figure 8.7: Recovered square object from a low magnetic field (figure 8.1) using the *nufft2()* and eliminating the high frequencies in the k-space as explained in figure 8.3

8.3. NUFFT Performance with Different Values of *K*

This section will follow the same process as section 6.3 with one dimension. For more details the reader is referred to that section.

The rank of the matrix $D_{\mathbf{u}}$ is found performing the singular value decomposition and following the same criteria of setting the singular values that $\sigma_i < 0.02\sigma_1$ to zero, where σ_1 is the biggest singular value and $0 \leq i \leq K-1$.
The full k-space was used in order to observe that in fact, with a small integer K, the object retrieved is very similar to the one using a higher K.
The computed rank for the matrices $D_{\mathbf{u}}^x$ and $D_{\mathbf{u}}^y$ is $K^x = K^y = 4$. The results can be seen in figure 8.8. The central image and right image correspond to the ranks $K^x = K^y = 4$ and $K^x = K^y = 14$, respectively, and there is no difference noticeable. Whereas the difference between these two images and the left one are significant. Therefore, the rank of the matrix could be reduced from $K^x = K^y = 16$ to $K^x = K^y = 4$. Note that for the image on the left, where $K^x = K^y = 1$, the colourbar does not correspond to the colourbars of the central and right images ($K^x = K^y = 4$ and $K^x = K^y = 14$).

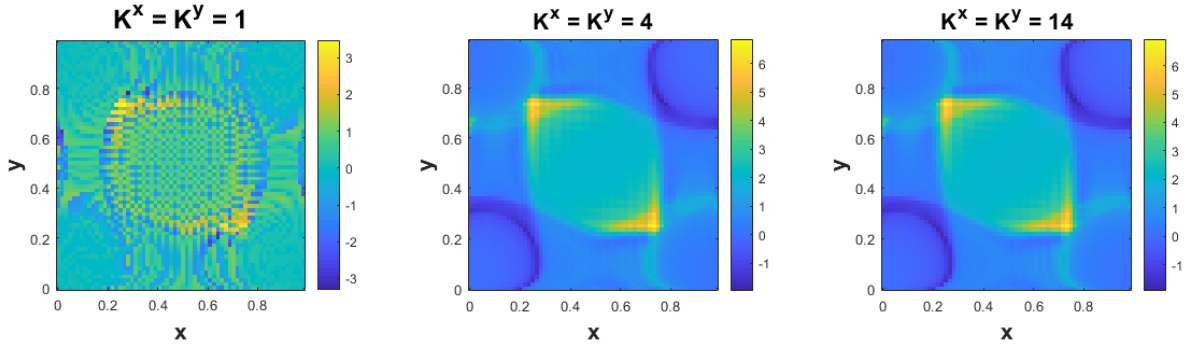

Figure 8.8: From left to right, square object retrieved in a low-field using *nufft()* with $K^x = K^y = 1$, $K^x = K^y = 4$ and $K^x = K^y = 14$

8.4. Time Costs

In this section, the time spent on the two-dimensional nonuniform Fourier algorithm will be measured and compared to the uniform case. The analysis is carried out in the same machine as in the one dimensional case, in section 6.4.
First, the parameter dependence will be shown in section 8.4.1 and second, the online stage of the 2D NUFFT in section 8.4.2.

8.4.1. Parameter Dependence

In this section, the number of samples $m \times n$ and the working precision ϵ, which is related to the rank K (equation 3.16) of the approximation matrices, will be modified in order to measure the computational time dependence.
The time values in tables 8.1 and 8.2 are computed with the average of ten thousand iterations. The time measured for the nonuniform fast Fourier transform algorithm *nufft2()* includes the whole algorithm process, these are steps 1 to 10, described in section 5.2.2.
Table 8.1 shows the time spent computing the conventional fast Fourier transform in two dimensions, i.e. *fft2()*. Each column corresponds to a different number of samples, from left to right: 16×16, 32×32 and 64×64 respectively. The more samples used, the more time spent computing the FFT.
The time costs are higher when the samples are not equally spaced. This is when the object is placed in the low magnetic field of figure 8.1. The time costs grow as the K parameter increases (i.e. working precision decreases). This is represented in table 8.2.
Table 8.3 shows the ratio $\frac{\text{time spent on } nufft2()}{\text{time spent on } fft2()}$ which goes from 170 times, when $m \times n = 16 \times 16$ and $K^x = K^y = 7$, to 795 times, when $m \times n = 64 \times 64$ and $K^x = K^y = 16$. Note that the time costs from this table do not correspond to the computational cost $\mathcal{O}(K^x K^y mn(\log m + \log n) + mn)$, because the whole process of the nonuniform algorithm is measured and not just the online stage.

Table 8.1: Time [ms] spent on *fft2()* algorithm, depending on the number of samples $m \times n$

	$m \times n = 16 \times 16$	$m \times n = 32 \times 32$	$m \times n = 64 \times 64$
Time [ms]	0.0163	0.0268	0.0622

Table 8.2: Time [ms] spent on *nufft2()* algorithm, depending on the number of samples $m \times n$ and the working precision ϵ in a low magnetic field

Working precision	$m \times n = 16 \times 16$	$m \times n = 32 \times 32$	$m \times n = 64 \times 64$
$\epsilon = 9.8\text{e}{-4}, \quad K^x = K^y = 7$	2.7745	5.3068	11.3512
$\epsilon = 1.2\text{e}{-7}, \quad K^x = K^y = 10$	5.8124	8.8249	21.0430
$\epsilon = 2.22\text{e}{-16}, \quad K^x = K^y = 16$	11.0895	18.2427	49.4273

Table 8.3: Time ratio spent on *nufft2()* algorithm in a low-field with respect to time spent on *fft2()*, depending on the number of samples $m \times n$ and the working precision ϵ

Working precision	$m \times n = 16 \times 16$	$m \times n = 32 \times 32$	$m \times n = 64 \times 64$
$\epsilon = 9.8\text{e}{-4}, \quad K^x = K^y = 7$	170	198	182
$\epsilon = 1.2\text{e}{-7}, \quad K^x = K^y = 10$	357	329	338
$\epsilon = 2.22\text{e}{-16}, \quad K^x = K^y = 16$	675	681	795

8.4.2. NUDFT Algorithm Implementation

The time that the online stage for the 2D case takes is analysed in this subsection. The online stage corresponds to the steps 7, 8 9 and 10 of section 5.2.2. Therefore, the sequences $\mathbf{s}$ and $\mathbf{t}$, the parameters δ and K, and the matrices $D_{\mathbf{u}}$ and $D_{\mathbf{v}}$, are already computed for both x- and y-directions.

We focus on the time that applying the two-dimensional approximation matrix takes, i.e. equation (3.25). This corresponds to $\mathcal{O}(mn(\log m + \log n) + mn)$ operations as seen in section 3.4. Where n is the number of samples in the x-direction and m is the number of samples in the y-direction.

Figure 8.9 shows the time in milliseconds spent performing the online stage, for different K (equation (3.18)) and different number of samples. Note that the x-axis shows the total number of samples, i.e. mn and $m = n$. The K values $K^x = K^y = 7$, $K^x = K^y = 10$ and $K^x = K^y = 16$ are chosen so that they match half, single and double precision respectively. The case when $K^x = K^y = 1$ is equivalent to performing the uniform FFT. It is difficult to see how much time the nonuniform takes over the uniform FFT, therefore we will zoom in the interval of $[2^4 \times 2^4,\ 2^5 \times 2^5]$ samples.

The left image of figure 8.10 shows the time spent in the nonuniform FFT when $K = 7$, i.e. half precision, with respect to the uniform FFT. For instance, when there are 16×16 samples, the time ratio nonuniform/uniform is 19.6. Whereas when there are 32×32 samples, it is 20.6. Therefore, the nonuniform case takes around twenty times the uniform with $[2^4 \times 2^4,\ 2^5 \times 2^5]$ samples.

The right image of figure represents the time spent in the nonuniform FFT when $K^x = K^y = 16$ and when $K^x = n$, $K^y = m$. This correspond to the time saved when applying an approximation of the nonuniform matrix. For instance, when the number of samples is 32×32, the approximation algorithm takes around 2.7 less computational time.

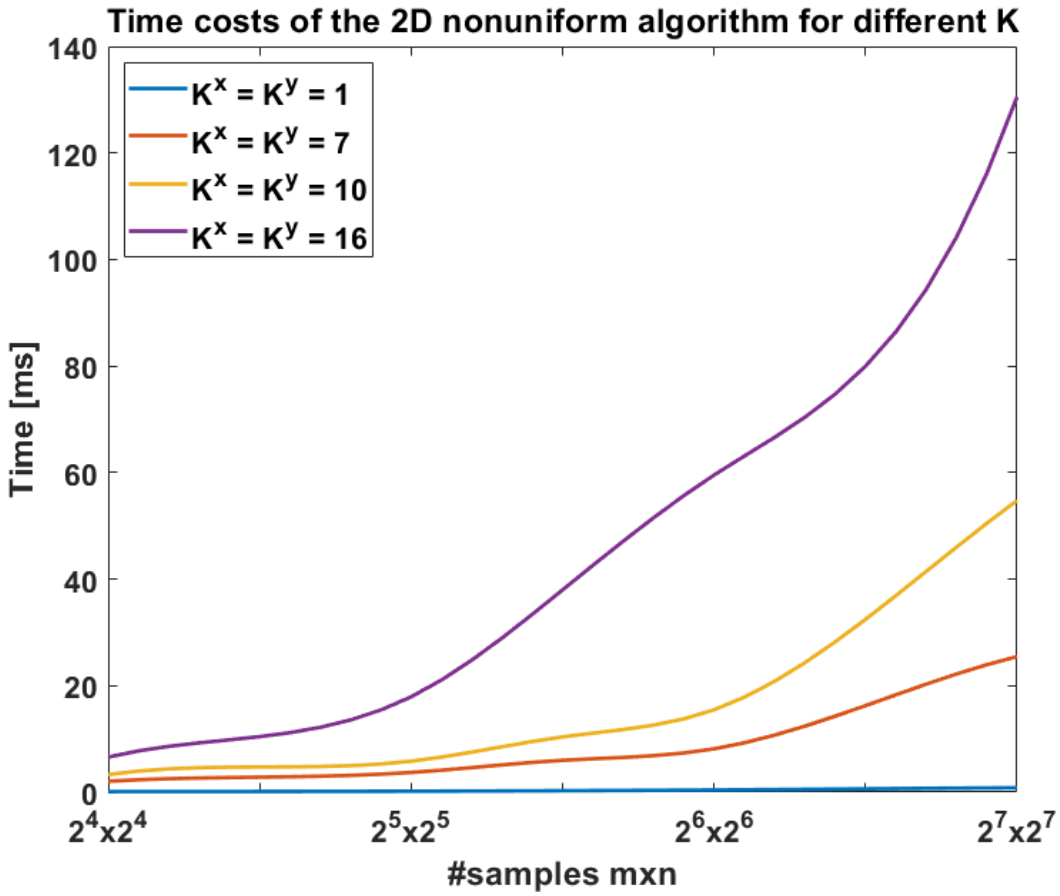

Figure 8.9: Time [ms] spent on the uniform 2D FFT ($K^x = K^y = 1$) and on the 2D NUFFT for $K^x = K^y = 7$, $K^x = K^y = 10$ and $K^x = K^y = 16$, with different number of samples mxn

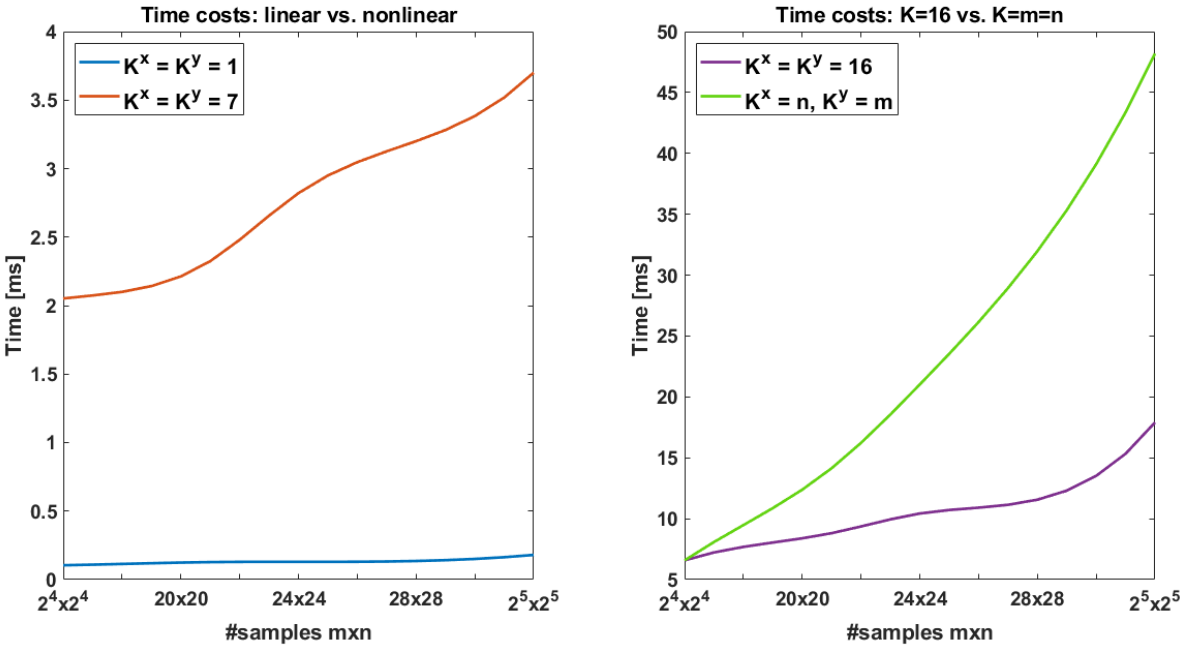

Figure 8.10: To the left, time [ms] spent on the linear 2D FFT versus the 2D NUFFT for $K^x = K^y = 7$. To the right, time spent on the nonlinear FFT with $K^x = K^y = 16$ versus $K^x = n$, $K^y = m$

9

CG and NUFFT in Two Dimensions

In this chapter, we will investigate whether the Conjugate Gradient method along with the two-dimensional nonuniform fast Fourier transform algorithm can be used to recover the scanned object from the two-dimensional MRI received signal.
The chapter begins with an introduction in section 9.1. In section 9.2, the results of this iterative algorithm are shown and discussed. The last section 9.3 will examine the performance of the Conjugate Gradient for our particular problem throughout the iterations and its convergence will be analysed.

9.1. Introduction

The results that will be seen in the following sections of this chapter are focused on the performance of the Conjugate Gradient method.
The aim is to retrieve the object M_{xy} from the two dimensional MRI signal, i.e. solve M_{xy} in

$$S(k_x, k_y) = \tilde{F}_1^y M_{xy}(x, y) \tilde{F}_1^{x\,T}. \tag{9.1}$$

Since the field is not linear, an inverse Fourier transform cannot be applied to the signal to obtain the object. However, the CG method is used to retrieve the desired object.
The Conjugate Gradient method is explained in sections 4.2.2 and 5.1. The CG solves for M'_{xy} in

$$\mathbf{S} = \left((\tilde{F}_1^{x\,*} \tilde{F}_1^x)^T \otimes (\tilde{F}_1^y \tilde{F}_1^{y\,*})\right) \mathbf{M}'_{xy}. \tag{9.2}$$

And the object is obtained by applying an NUFFT-II to the solution of the CG conjugated and taking the conjugate of the result, i.e.

$$M_{xy} = \text{conj}\left(\tilde{F}_2^y \,\text{conj}(M'_{xy}) \tilde{F}_2^{x\,T}\right). \tag{9.3}$$

9.2. Retrieving the Object

The results in this section are obtained using the Conjugate Gradient and the nonuniform Fourier transform algorithms explained in chapter 5 in an MRI signal from a square object, figure 8.2, in the low magnetic fields of figure 8.1. These are the fields from the low-field MRI scanner in Leiden University Medical Center [27].
The number of samples used is $m \times n = 64 \times 64$ and the working precision is double, i.e. $\epsilon = 2.22\text{e}{-16}$, $K \approx 16$. The number of iterations of the Conjugate Gradient is fixed to $R = 500$.

9.2.1. Low Magnetic Fields

Figure 9.1 shows the ideal object and the object retrieved using 500 iterations of the Conjugate Gradient method. Note that the colours of the ideal object have been changed so that they match the colourbar of the object retrieved and both images can be easily compared.
The object retrieved differs from the ideal. The shape of the square is rounded and the background presents some noise. Nevertheless, the result of using several iterations of the CG improves the object retrieved. Comparing the right image of figure 9.1 with the right image of figure 8.5, where just one iteration of the CG was used, many differences are noticeable. The circles in the background of the $R = 1$ case disappear, and the shape of the square looks more similar to the ideal in the $R = 500$ case.

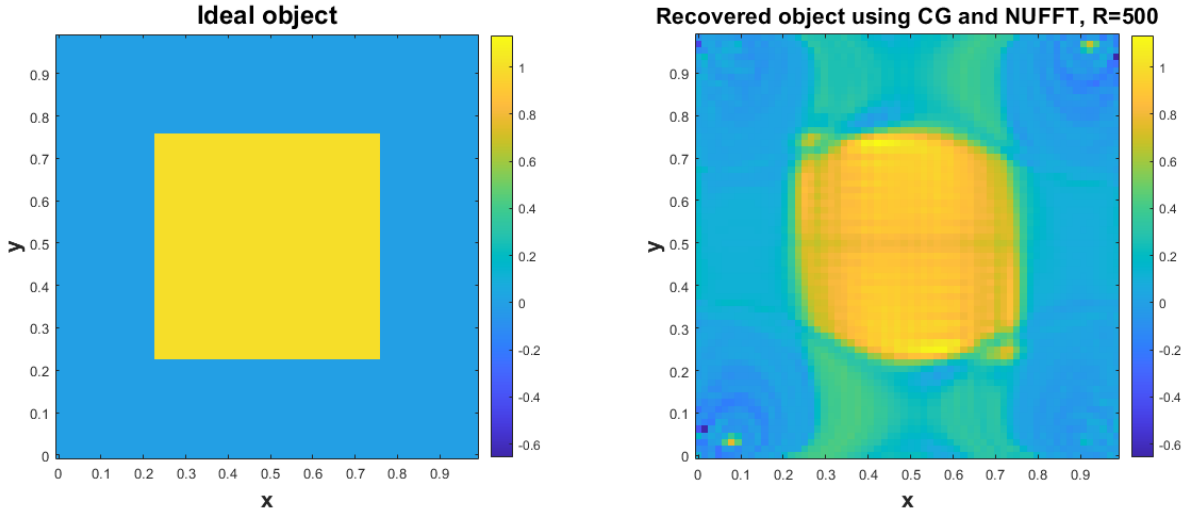

Figure 9.1: To the left, ideal object. To the right, retrieved object using the NUFFT and $R = 500$ iterations of the CG from the gradient fields from LF-MRI LUMC scanner, figure 8.1

9.3. Performance through Iterations

In the previous section 9.2, the number of iterations of the Conjugate Gradient method was fixed to $R = 500$. Computational time is proportional to this number, since increasing the number of iterations will take more time and decreasing the number will save it. Nevertheless, in exchange for time, the accuracy of the retrieved object is affected. It has previously been observed in section 7.3 that both the residual and the error stabilise after a certain number of iterations. Therefore, in this section we will try to find when the Conjugate Gradient can be considered stable, focusing on the low-fields of figure 8.1.

The residual and the error are rewritten for the nomenclature of the 2D case in the following lines. The relative residual is defined as

$$r_{\text{rel}} = \frac{\|\mathbf{S} - \left((\tilde{F}_1^{x*}\tilde{F}_1^{x})^T \otimes (\tilde{F}_1^{y}\tilde{F}_1^{y*})\right)\mathbf{M}'_{xy}\|_2}{\|\mathbf{S}\|_2}, \tag{9.4}$$

and the relative error is computed as

$$e_{\text{rel}} = \frac{\|\mathbf{M}_{xy}^{\text{ideal}} - \mathbf{M}_{xy}^{\text{retrieved}}\|_2}{\|\mathbf{M}_{xy}^{\text{ideal}}\|_2}. \tag{9.5}$$

In the following subsections 9.3.1 and 9.3.2 the convergence of the residual and the error will be seen respectively.

9.3.1. Convergence of the Residual

The residual (equation (9.4)) represents how far the Conjugate Gradient is from the correct value of the signal $S(k_x, k_y)$.

In figure 9.2 the residual of the CG can be seen from one to one thousand iterations, when retrieving the square object from the low-fields. It can be seen that in the first hundred iterations the residual drops drastically and afterwards the rate of convergence decreases. The right image of figure 9.2 zooms in the $R \in [0, 100]$ interval of iterations where the rate of convergence is the fastest.

In the previous section 9.2, the number of iterations was $R = 500$ and this corresponds to a $r_{rel} \approx 0.006$. Performing a thousand iterations gives a residual of $r_{rel} \approx 0.0045$. This means that in the last 500 iterations the residual decreases 25%, whereas in the first 500 it decreases 99.4%.

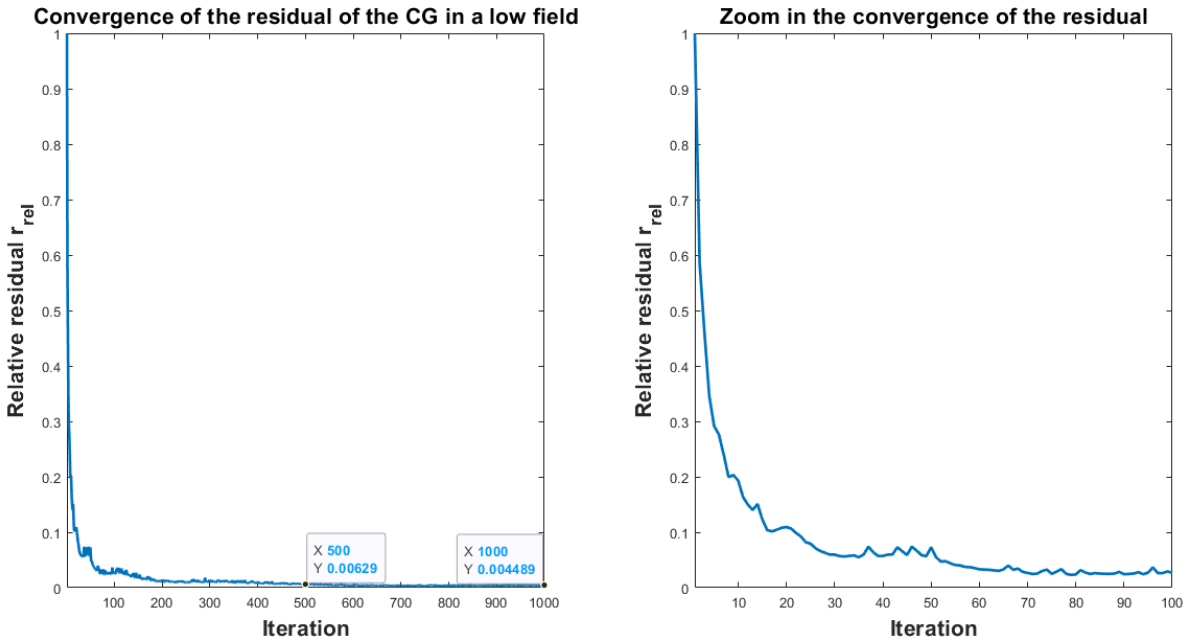

Figure 9.2: To the left, relative residual computed from 1 to 1000 iterations of the Conjugate Gradient method retrieving the square from a low-field. To the right, zoom in the interval $[1, 100]$ iterations

9.3.2. Convergence of the Error

The error (equation (9.5)) measures the difference between the ideal object and the object retrieved.
The curve of the convergence of the error when retrieving the square object from a low-field can be seen in figure 9.3, from one to one thousand iterations of the CG. In a similar way as in the residual, the error decreases fast at the beginning and it stabilises when the number of iterations increases.
The number of iterations of the example of the previous section 9.2 was $R = 500$, which means a relative error of $e_{rel} \approx 0.41$. In the interval from seven hundred to a thousand iterations, the error stagnates to a value of $e_{rel} = 0.4026$. Therefore, is not worth to perform more than seven hundred iterations.
Figure 9.4 shows the object retrieved $M_{xy}(x, y)$ when the number of iterations is $R = 100$, $R = 500$ and $R = 1000$. It can be seen that the difference between the objects is greater between the $R = 100$ and $R = 500$ cases than the $R = 500$ and $R = 1000$ cases. The differences can be appreciated in the uniformity of the background and interior of the object.

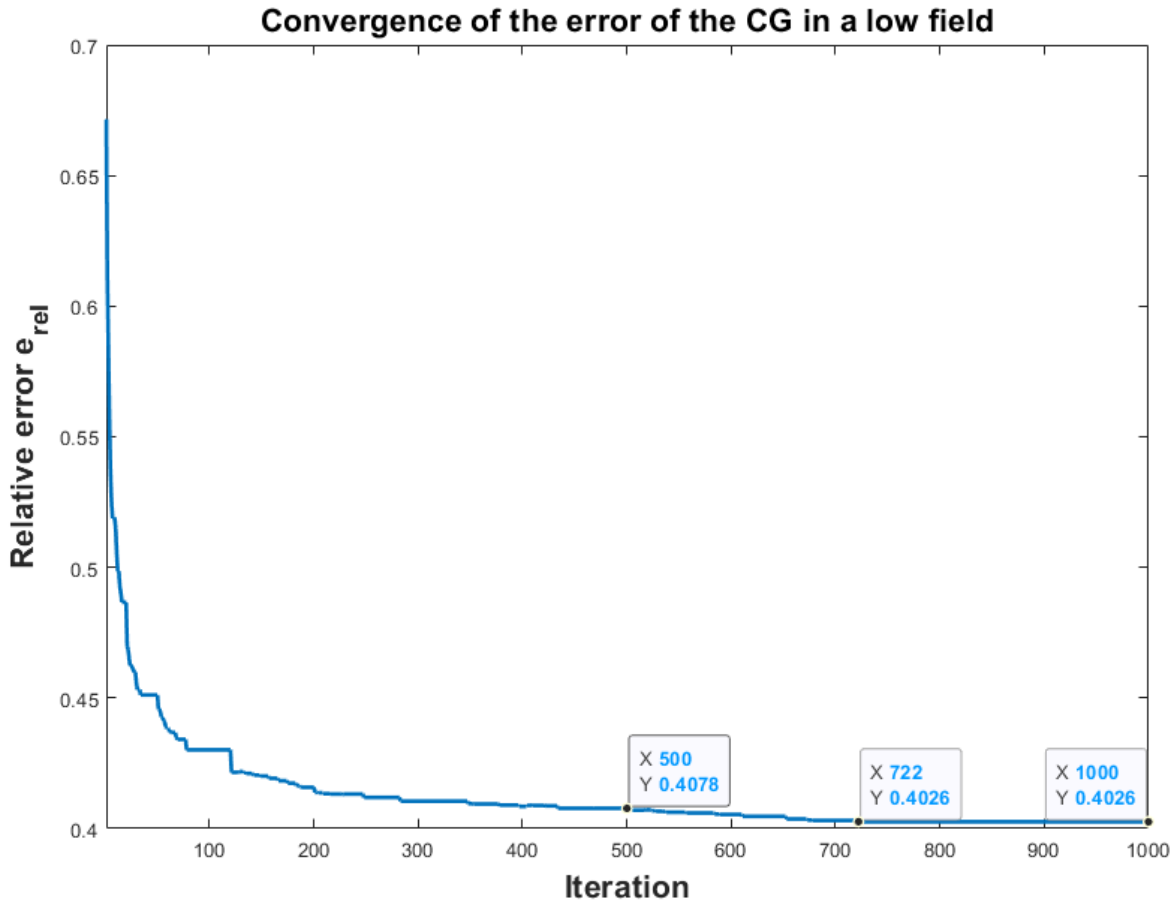

Figure 9.3: Relative error computed from 1 to 1000 iterations of the Conjugate Gradient method retrieving the square from a low-field

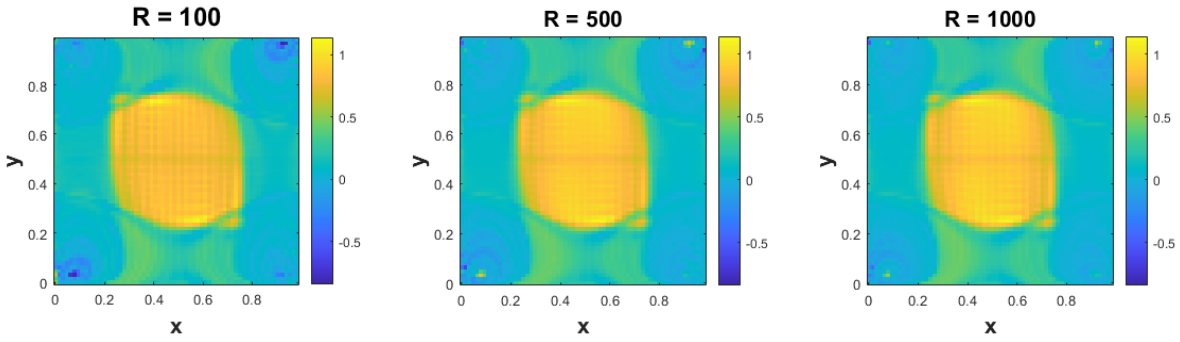

Figure 9.4: Object recovered M_{xy} from a low-field using different number of iterations R of the CG. From left to right, $R = 100$, $R = 500$ and $R = 1000$ iterations

10

Conclusions and Future Work

10.1. Conclusions

The purpose of this thesis was to implement a fast algorithm to retrieve the objects scanned in a low-field magnetic resonance imaging (LF MRI) machine. The motivation of this research was settled in the introduction. A low-field MRI is a safe and cheap alternative to other detection devices such as Computed Tomography or High-Field MRI. Cheap, because the low-field machine is constructed out of economical materials and it does not require costly maintenance. Safe, because it does not use ionising radiation, which is hazardous for humans and in particular for the children. The disadvantage of the low-field MRI is that it produces images of relatively poor quality and as a result, the processing of these images becomes complicated and time-consuming. The solution to this problem is to speed up the image processing with little loss of quality, using a nonuniform fast Fourier transform.
In the first part of the report, the basic knowledge was consolidated. First, the form of the signal that the low-field machine generates and second, the explanation of the mathematical principles that the nonuniform fast Fourier transform algorithm is based on.
The second part gives an overview of the procedure followed in the research, stating the problems that are solved. In addition, the algorithms used in the experiments are detailed for both one and two dimensions. These two algorithms employed are the nonuniform fast Fourier transform (NUFFT) and the Conjugate Gradient (CG).
In the last part of the report, the results are presented, first in one dimension and then in two dimensions, and just applying the nonuniform fast Fourier transform algorithm and then adding the Conjugate Gradient.
It was showed that using just one iteration of the Conjugate Gradient is equivalent to directly apply the nonuniform Fourier transform algorithm to the signal received from the LF MRI. It was seen how this algorithm worked for the particular case of the low-field gradients from the Leiden University Medical Center and in addition, its performance was compared to the conventional fast Fourier transform algorithm. The time costs of the nonuniform algorithm were measured for different cases and compared to the uniform fast Fourier transform.
We have tried to improve the quality of the object retrieved using a priori information: eliminating half of the k-space samples gave better results. Besides trying to enhance the quality of the image, we have attempted to further speed up the nonuniform algorithm by increasing the working precision without loss of quality. The results of eliminating half of the k-space and increasing the working precision were promising with just one iteration of the CG. Nevertheless, when the number of CG iterations is high, these two approaches worsen the results. It was concluded that the best option was to use the full k-space and if the number of iterations of the CG is low, it is convenient to use a higher working precision in order to save computational time. However, when the number of iterations is larger, above ten iterations approximately, the quality of the object retrieved worsens significantly and therefore, a smaller working precision must be used.
Regarding the results obtained when employing the Conjugate Gradient along with the nonuniform Fourier transform algorithm, a noticeable improvement was observed. The convergence of the residual and the error was studied and analysed in order to find an optimum value of iterations.

10.2. Future Work

Below, a list of suggestions to further develop the experiments of this thesis will be given.

- A priori info was used in order to improve the results. We know that the objects scanned are real and therefore, they present conjugate symmetry in the Fourier domain. This means that we only need half of the k-space since the other half can be estimated. Other aspects could be useful such as knowing the exact place of the object that is being scanned. For example, if the object is a brain, we know that it will be

placed in the middle and that it will present approximately a round shape. Therefore, the background can be estimated using this information and noise could be eliminated.

- The performance of the nonuniform Fourier transform was checked on basic objects, such as the square. It was mentioned at the beginning of this report that the aim was to detect hydrocephalus in children. Now the next step is to test the NUFFT in real experiments.
- There is existing software for one dimension for all the types of NUFFT, direct and inverse, provided by [5]. Regarding the two-dimensions, only the direct type two NUFFT was available in [5]. In this thesis, the missing NUFFTs were developed. Unfortunately, for the three-dimensional case, the software is still lacking.
- It was seen that the shape of the low-fields (e.g. the two bumps at the edges of the gradient field along x-direction) caused problems retrieving the image. An interesting experiment could consist in removing these nonideal areas and estimate the missing samples with an interpolation. Moreover, it was seen that the nonidealities were accentuated when the object was placed on them, so moving the object in order to avoid these nonideal areas of the gradient fields could be tested as well.

A

One Dimension

The following figures are more examples from section 6.2. The square object (figure A.1) is retrieved from a linear magnetic field and from a quadratic magnetic field, left and right images of figure A.2 respectively.

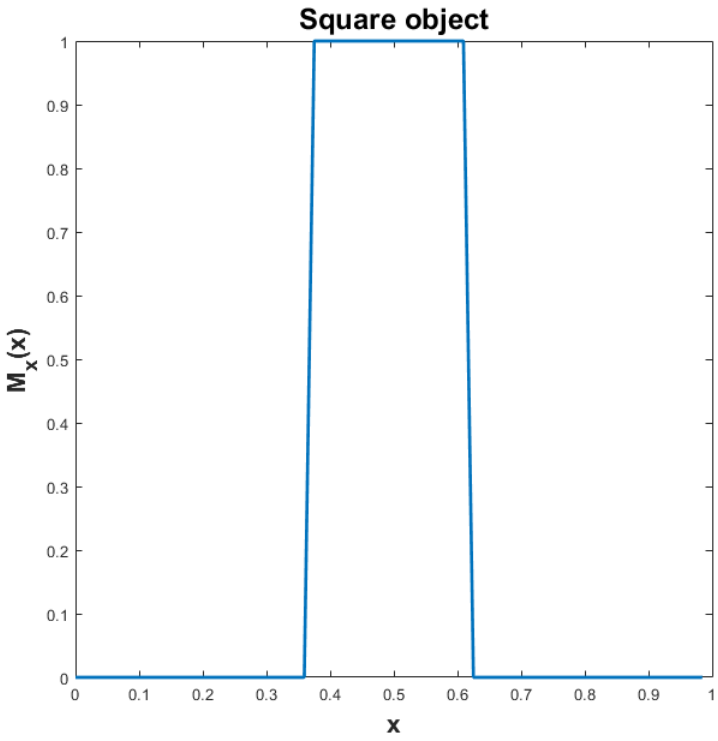

Figure A.1: Square shaped object used in the experiments

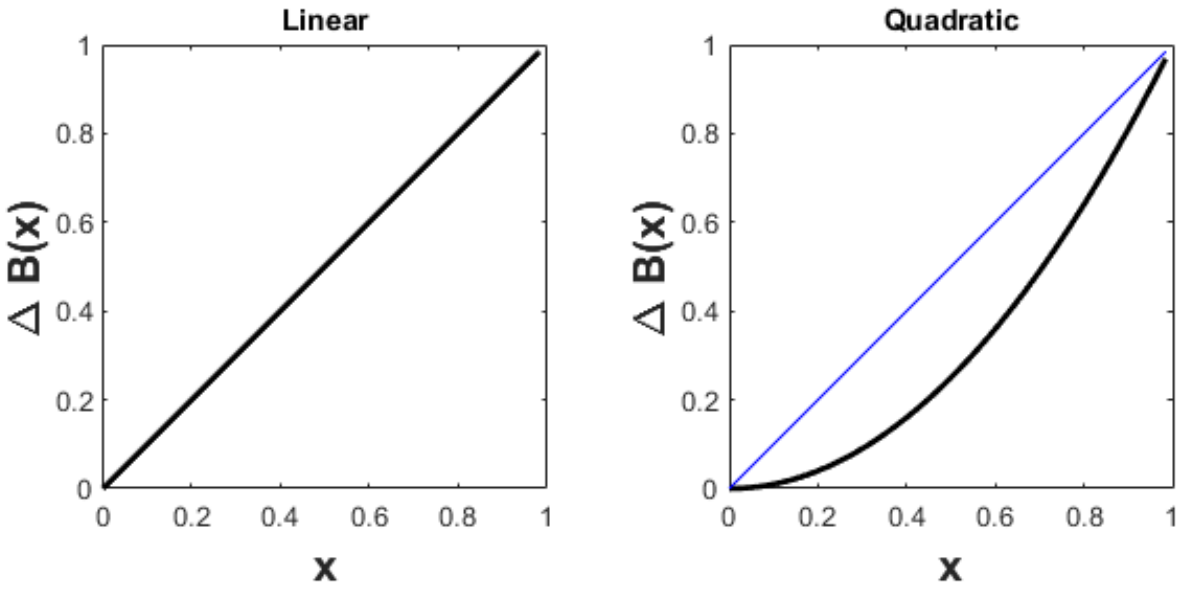

Figure A.2: To the left, linear magnetic field. To the right, quadratic magnetic field. The quadratic field is compared to the linear case represented with a blue line

A.1. Linear Magnetic Field

The field used in this section is linear (left image of figure A.2), i.e. the samples $\Delta B_x(\mathbf{x})$ are equispaced. Looking at the first two steps of section 5.2.1, the sequences $\mathbf{s}$ and $\mathbf{t}$ are equal to $\Delta B_x(\mathbf{x})$ and therefore, any adjustment is done. At step three, the computed perturbation parameter is zero. The value of this parameter is set to a number very close to zero in order to avoid a division by 0 in equation (3.16). In consequence, the integer results in $K = \max(3, 0) = 3$ and the matrices $D_{\mathbf{v}}$ and $D_{\mathbf{u}}$ present three columns. In particular, matrix $D_{\mathbf{u}}$ is of the form

$$D_{\mathbf{u}} = \begin{bmatrix} 1 & 0 & 0 \\ \vdots & \vdots & \vdots \\ 1 & 0 & 0 \end{bmatrix} \tag{A.1}$$

Since only the first column of this matrix has nonzero elements and $I(\mathbf{t}, :)$ is the identity matrix, equations (5.10) and (5.11) can be simplified to just applying the uniform Fourier transform to the MRI signal.
Therefore, $\tilde{F}_2$ in this case is the uniform Fourier matrix and no approximation is required, i.e.

$$M_x(\mathbf{x}) = \left(\tilde{F}_2 S(\mathbf{k_x})^*\right)^* = (IFS(\mathbf{k_x})^*)^* = F^* S(\mathbf{k_x}). \tag{A.2}$$

This means that both uniform Fourier transform and nonuniform Fourier transform algorithms give the same results. In addition, the conjugate of the uniform Fourier matrix is in fact the inverse matrix and the object is retrieved perfectly. This can be seen in the left and right images of figure A.3.

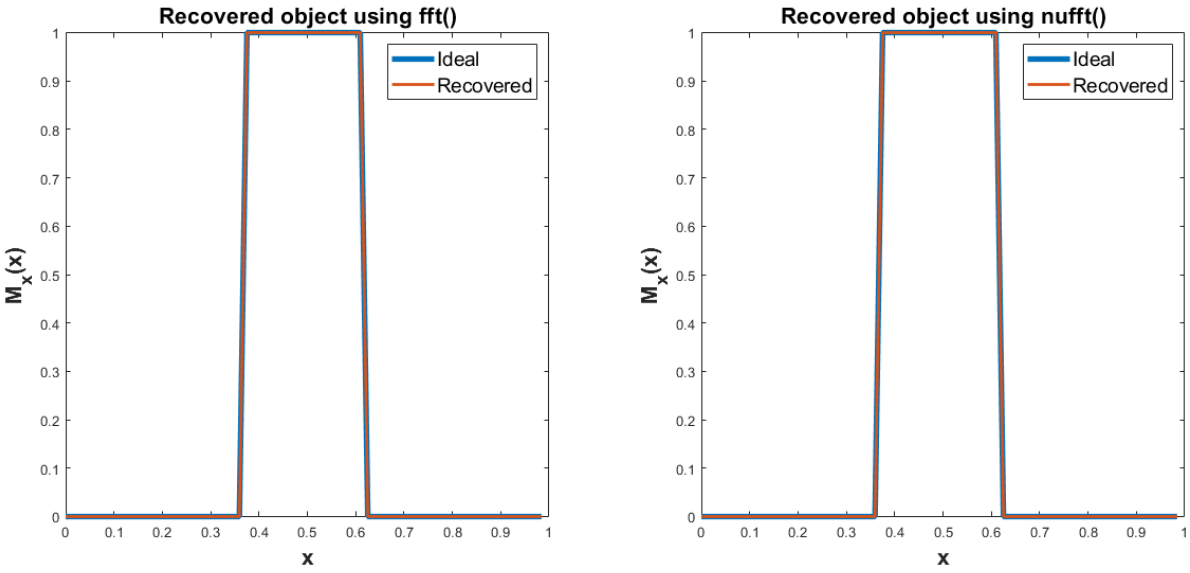

Figure A.3: To the left, recovered square pulse from a linear magnetic field, first image in figure A.2, using the Fourier transform algorithm, *fft()*. To the right, same object recovered using the nonuniform Fourier transform algorithm, *nufft()*. Both cases are compared to the ideal object

A.2. Quadratic Magnetic Field

A quadratic magnetic field (second image in figure A.2) is applied to the square object. The magnetic field, $\Delta B_x(\mathbf{x})$, and the sequence $\mathbf{s}/N$ differ as seen in figure A.4. In the interval $x \in [0, 0.4]$, several close nonequispaced samples are assigned to the same uniform node. This resembles spatial oversampling. Whereas in the interval $x \in [0.6, 1]$, the nonuniform samples are assigned to uniform nodes that are not adjacent, i.e. there are gaps. This is equivalent to spatial aliasing or undersampling.
Regarding the $\mathbf{t}$ sequence, it is equal to the $\mathbf{s}$ sequence since there are no values $\Delta B_x(x_j) = 1$ for $0 \leq j \leq N-1$. Note that the $\mathbf{t}/N$ sequence is represented with crosses instead of a continuous line so that it does not cover the $\mathbf{s}/N$ sequence.

The value for the perturbation parameter is $\delta = 0.4844$ (recall that $\delta = |N\Delta B_x(\mathbf{x}) - \mathbf{s}|_\infty$) and the condition of equation (3.17) holds. The corresponding integer for double precision is $K = 15$ and therefore, matrices $D_{\mathbf{v}}$ and $D_{\mathbf{u}}$ have fifteen columns. Although for this case the rank of $D_{\mathbf{u}}$ is less than 15 and therefore, the approximation could be achieved with a smaller integer K, the value of K will not be modified. The value of the integer K is modified and discussed in section 6.3. The results of lowering K for the quadratic magnetic field are shown in the following subsection A.2.1.
The MRI signal received is shown in figure A.5, compared to the ideal MRI signal that is obtained when applying the uniform DFT to the ideal object of figure A.1.
At high frequencies, there are distortions in the signal, due to the values of the quadratic field in the interval $x \in [0.6, 1]$. These values are too separated, as explained before, resembles undersampling. When undersampling, harmonics appear at high frequencies. This adds noise to the MRI signal at high k-space samples and thus degrading the quality of the retrieved object.
Focusing on figure A.6, this time the *fft()* function places the object to the left. This result can be understood by taking a look at the Fourier transform properties, where a multiplication in frequency corresponds to a shift in the time domain, i.e.

$$y(n - n_0) \quad \leftrightarrow \quad Y(k)\mathrm{e}^{-in_0 k}. \tag{A.3}$$

The corresponding equation (A.3) to our signals in the x-space image domain and the k-space frequency domain results in

$$M_x\big(x - Q(x)\big) \quad \leftrightarrow \quad S(k_x)\mathrm{e}^{-iQ(x)k_x}. \tag{A.4}$$

In this case, the displacement is not a constant value but a quadratic function, namely

$$Q(x) = \Delta B_x(x)_{\text{quadratic}} - \Delta B_x(x)_{\text{linear}}, \tag{A.5}$$

which is represented in the second image of figure A.7.

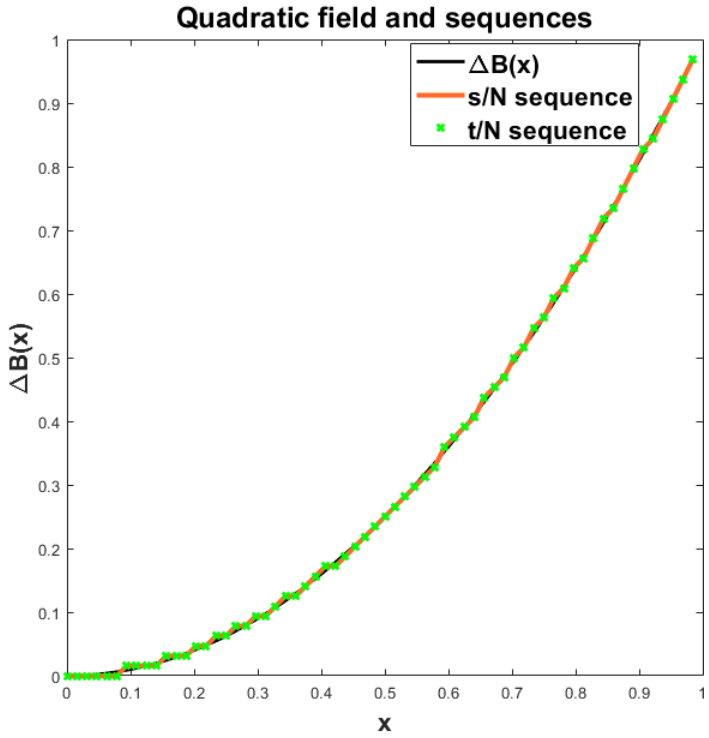

Figure A.4: Quadratic magnetic field (second image in figure A.2) and its sequences $\mathbf{s}/N$ and $\mathbf{t}/N$

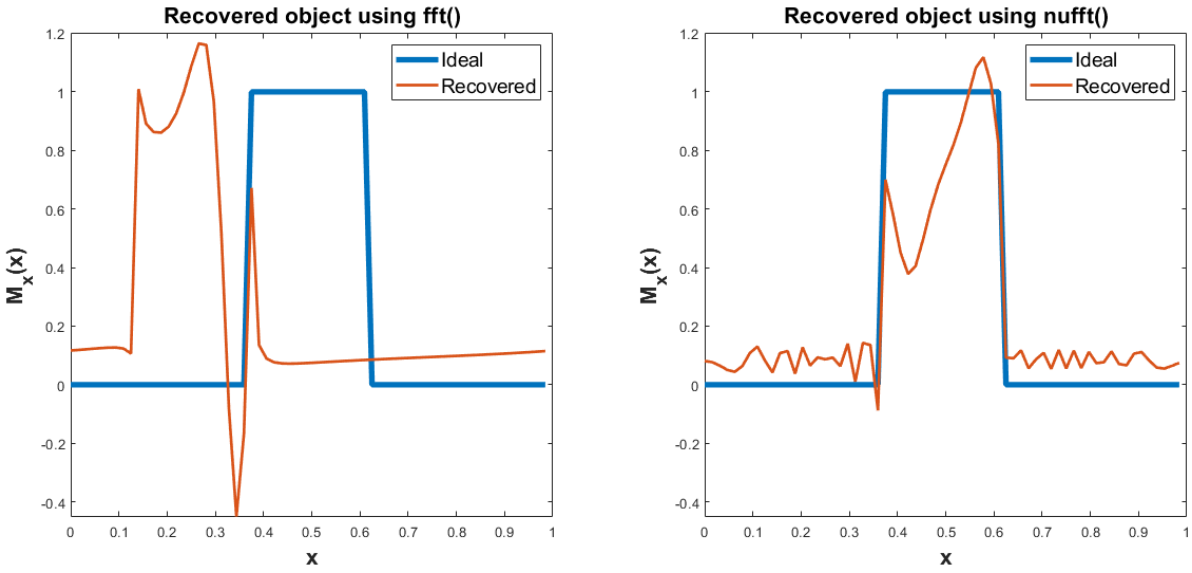

Figure A.6: To the left, recovered square pulse from a quadratic magnetic field (second image in figure A.2), using the Fourier transform algorithm, *fft()*. To the right, same object recovered using the nonuniform Fourier transform algorithm, *nufft()*. Both cases are compared to the ideal object

The first image of figure A.7 shows the quadratic magnetic field with respect to the linear field. The arrows show the spatial delay that the quadratic magnetic field represents with respect to the linear field at the central value $x = 0.5$, which is

$$Q(0.5) = \Delta B_x(0.5)_{\text{quadratic}} - \Delta B_x(0.5)_{\text{linear}} = 0.25 - 0.5 = -0.25. \tag{A.6}$$

This means that the recovered square object presents a displacement of 0.25 to the left using the *fft()*, first image of figure A.6. On the other hand, the *nufft()* locates the square correctly but, like the *fft()*, presents amplitude distortion in the flat areas of the object.

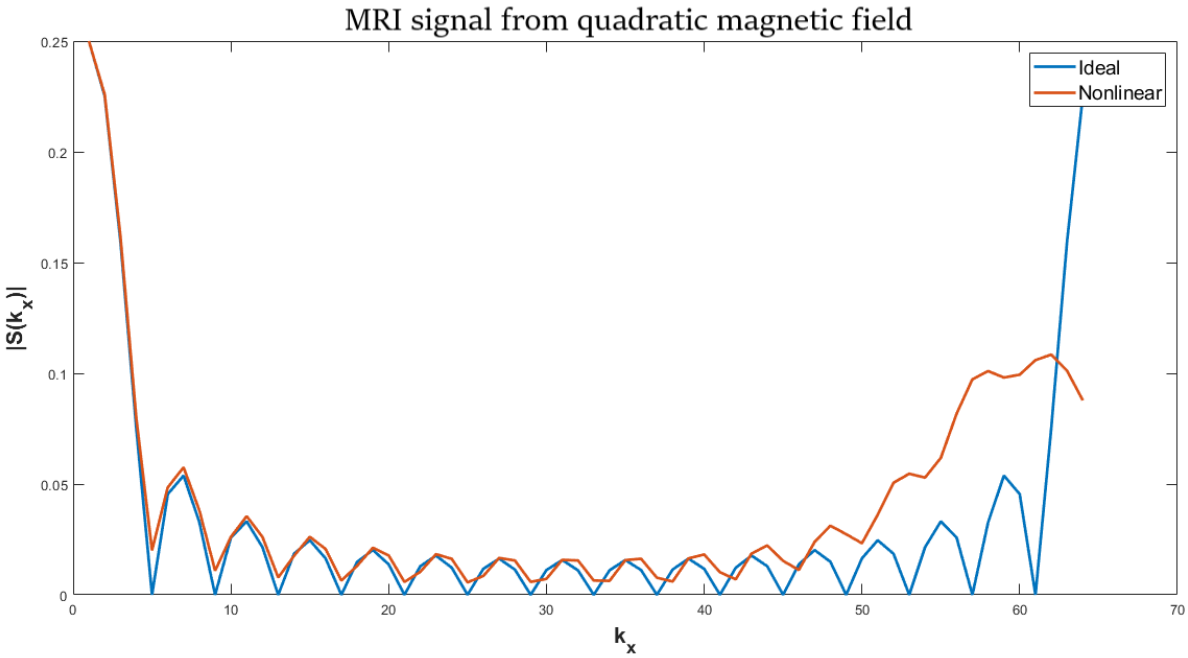

Figure A.5: Received MRI signal from a square object in a quadratic magnetic field (second image in A.2) compared to the ideal MRI signal, i.e. the signal received when applying the uniform *fft()*

To eliminate the amplitude distortions, we look again at the MRI signal of figure A.5. Since the Fourier transform is performed on a real object, the resulting signal presents conjugate symmetry. Therefore, half of the k-space can be estimated. The MRI signal received is similar to the ideal at low frequencies. Nonetheless, they start to differ when $k_x > N/2 = 32$. Removing the upper half of the k-space samples leads to figure A.8, which shows a better performance in both linear and nonlinear cases.
Nonetheless, eliminating half of the k-space samples leads to distortions at the edges of the square due to the Gibbs ringing artefact. The Gibbs phenomenon can be attenuated applying a window to the MRI signal. The objects that present a smooth shape are less affected with the Gibbs phenomenon and therefore, better results in the recovered objects are obtained. Figure A.9 shows the result of the *nufft()* when a Hamming window is applied to the MRI signal of the square object in a quadratic magnetic field.

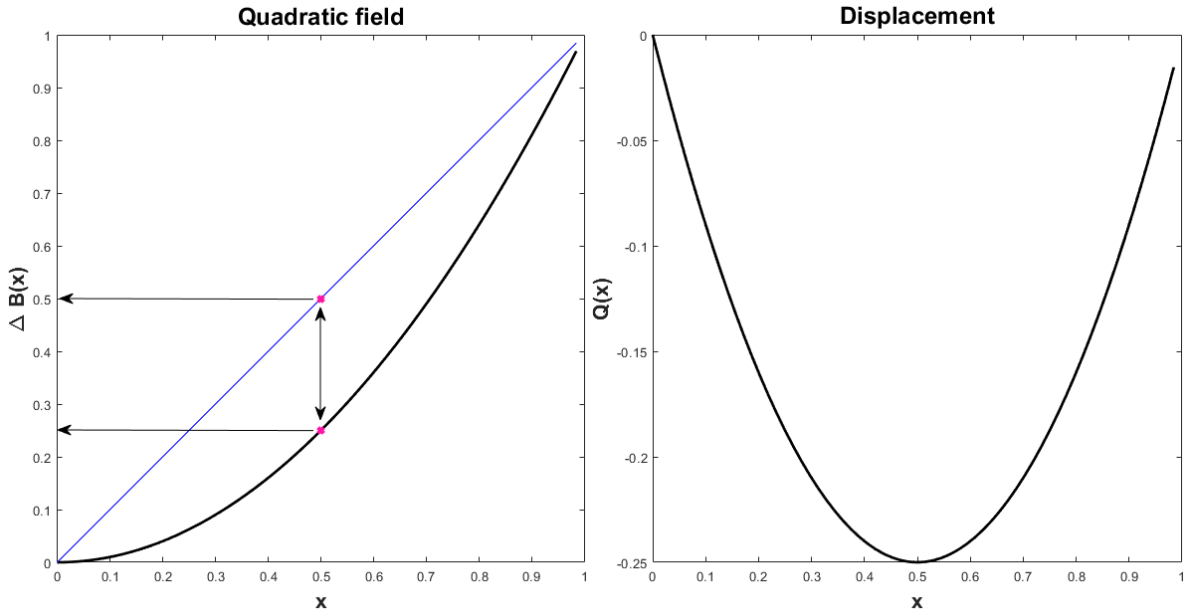

Figure A.7: To the left, quadratic magnetic field (black) and linear magnetic field (blue). The arrows point at the central value $\Delta B_x(x) = 0.5$ and they show the displacement of the quadratic field w.r.t. the linear. To the right, value of the space delay of the quadratic field $Q(x)$ at every x-location

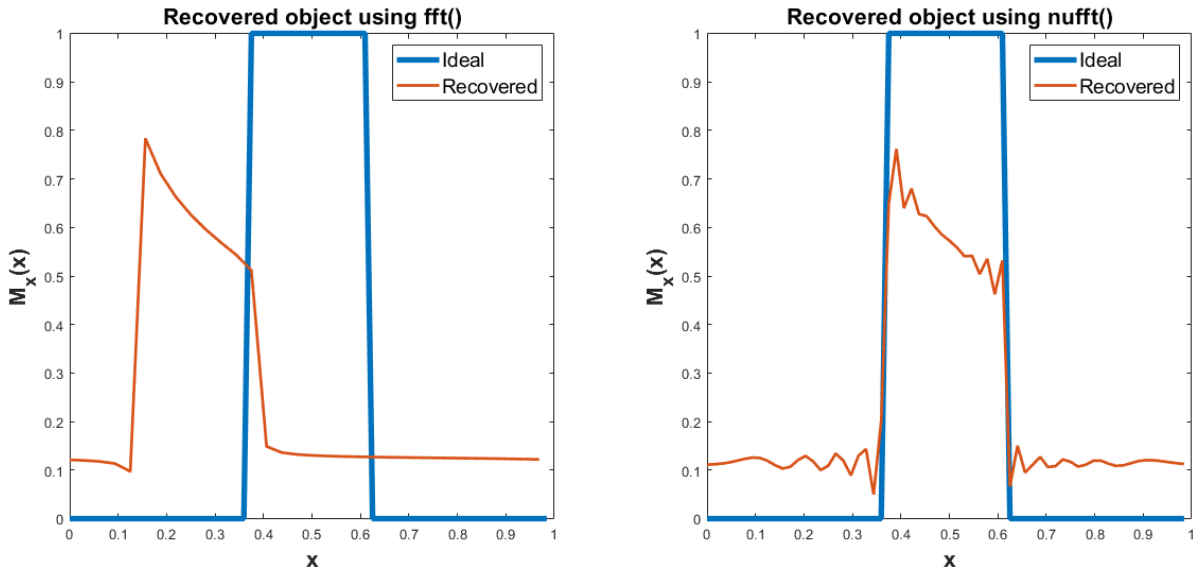

Figure A.8: To the left, recovered square pulse from a quadratic magnetic field (second image in figure A.2) using the *fft()* and half of the k-space samples. To the right, same object recovered using the *nufft()* and half of the k-space samples. Both cases are compared to the ideal object

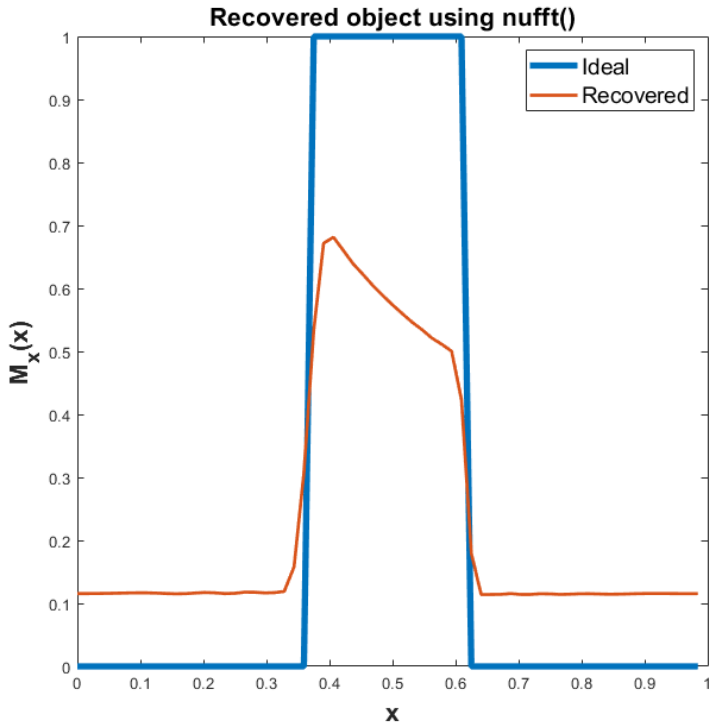

Figure A.9: Recovered square pulse from a quadratic magnetic field (second image in figure A.2) using the *nufft()*, half of the k-space samples and applying a Hamming window to the MRI signal. It is compared to the ideal object

A.2.1. NUFFT Performance with Different Values of *K*

As mentioned before, the value of the rank of the approximated matrix A_K was $K = 15$ for double precision. The result can be seen in the right image of figure A.6. Figure A.10 represents the recovered object using the *nufft()* with $K = 1$, $K = 2$ and $K = 4$ respectively.
With just one $\mathbf{u}$ vector ($K = 1$) the object differs from the one for $K = 15$. The object retrieved starts to look alike when the nonuniform Fourier matrix is approximated with two $\mathbf{u}$ vectors ($K = 2$). Looking at the third image, it can be seen that with a four rank approximation matrix ($K = 4$) the object is the same as to the one retrieved with $K = 15$ (right image of figure A.6). Therefore, the number of operations could be reduced by almost four times when using a quadratic magnetic field.

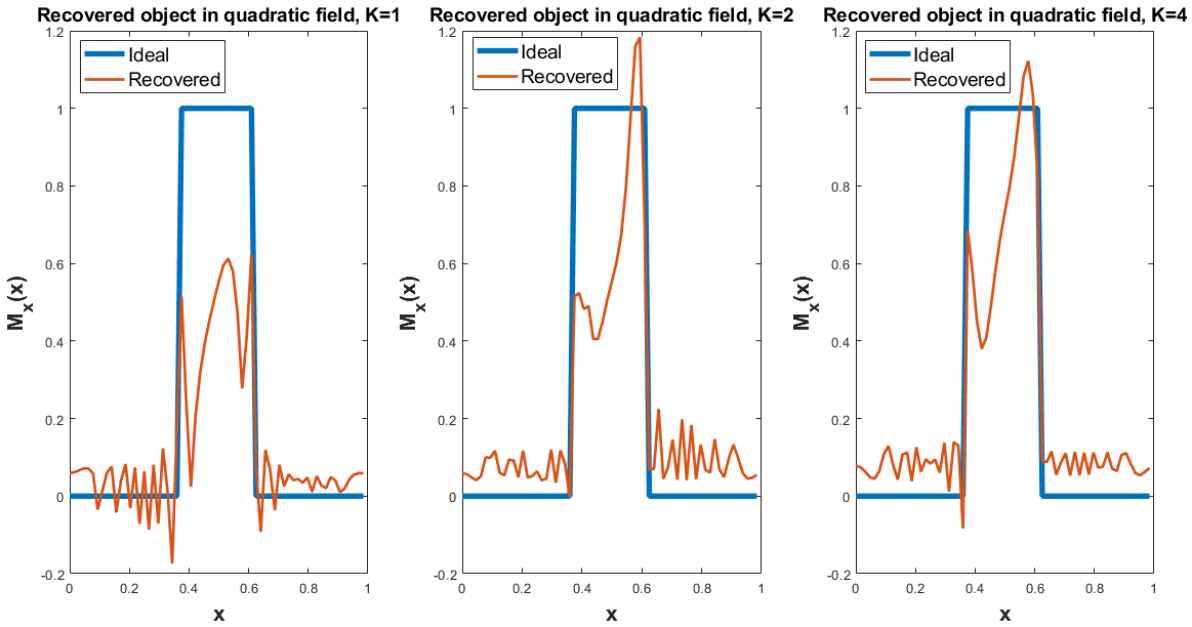

Figure A.10: From left to right, square object in a quadratic field (second image in figure A.2) retrieved using *nufft()* with $K = 1$, $K = 2$ and $K = 4$

A.2.2. Results Using CG and NUFFT

The result of the MRI signal from the quadratic field after applying 50 iterations of the conjugate gradient can be seen in figure A.11. The shape of the square is recovered but there is noise in the left background of the square. As the number of iterations is increased, the noise in the background disappears.
In the left image of figure A.12, the object recovered from a signal with half of the k-space can be visualised. The result is worse than the one with full of the k-space. The explanation of this loss of quality in the result can be found in 7.2.1.
The right image of figure A.12 shows the result when the approximation matrix A_K of the nonuniform Fourier transform is fixed to the rank $K = 4$. See subsection 7.2.1 for more details.

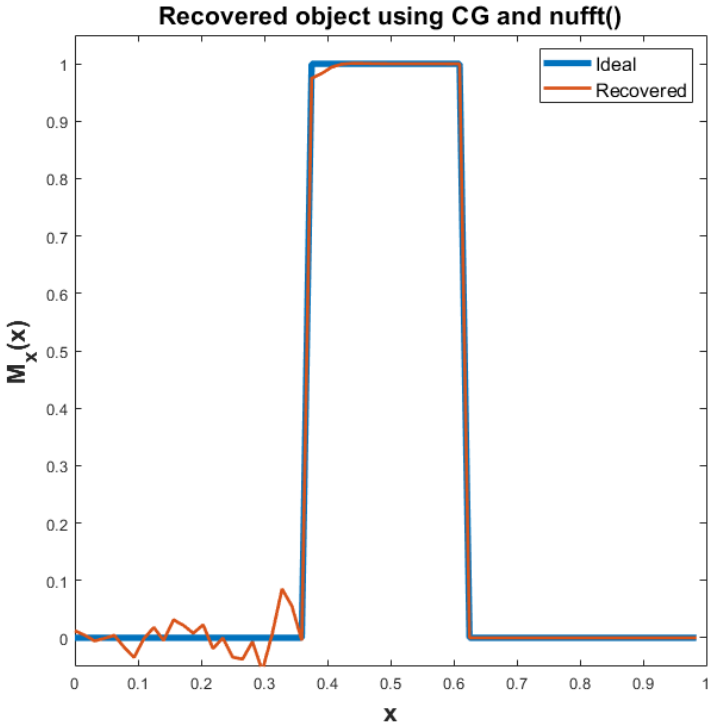

Figure A.11: Object recovered $M_x(x)$ from a quadratic field (second image of figure A.2) using 50 iterations of the CG and the NUFFT

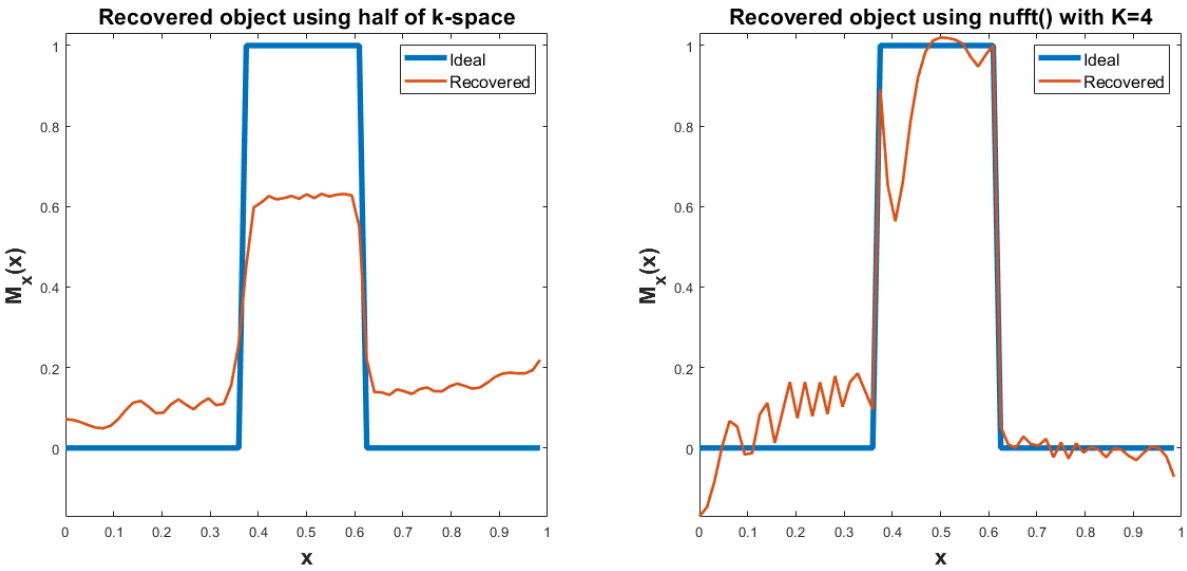

Figure A.12: Object recovered $M_x(x)$ from a quadratic field (second image of figure A.2) using 50 iterations of the CG and the NUFFT. To the left, half of the k-space samples were used. To the right, the *nufft()* with $K = 4$ was used

B

Two Dimensions

The following results are more examples from section 8.2. The square object (figure 6.1) is retrieved from different magnetic fields. Figures B.2 to B.4 represent these magnetic fields.
The fields of figure B.2 are linear and they are used in section B.1. In figure B.3, the fields are quadratic and they are used in section B.2. In the last figure B.4, the fields are a low-field approximation and they are used in section B.3. The number of samples is 64×64 and the working precision is double, $\epsilon = 2.22\text{e}{-16}$.

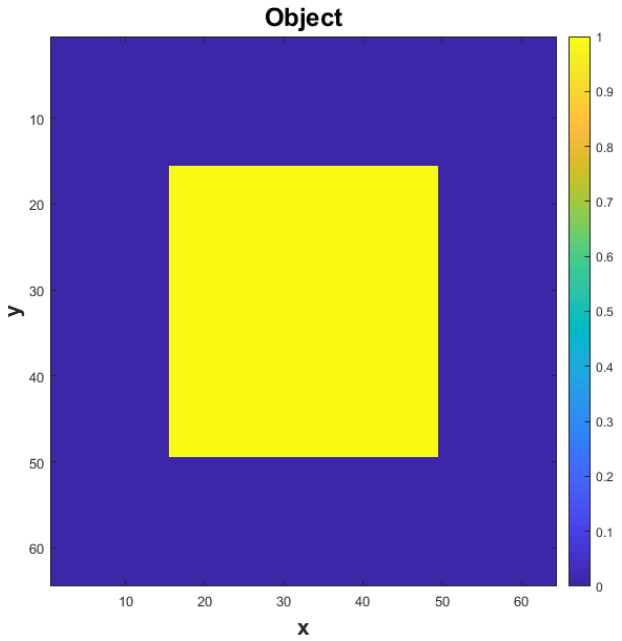

Figure B.1: Square shaped object that is used in different magnetic fields

In the same way as in section 8.2, some k-space samples will be eliminated in the following experiments in order to try to improve the quality of the object retrieved. See sections 6.2 and 8.2 for more details.

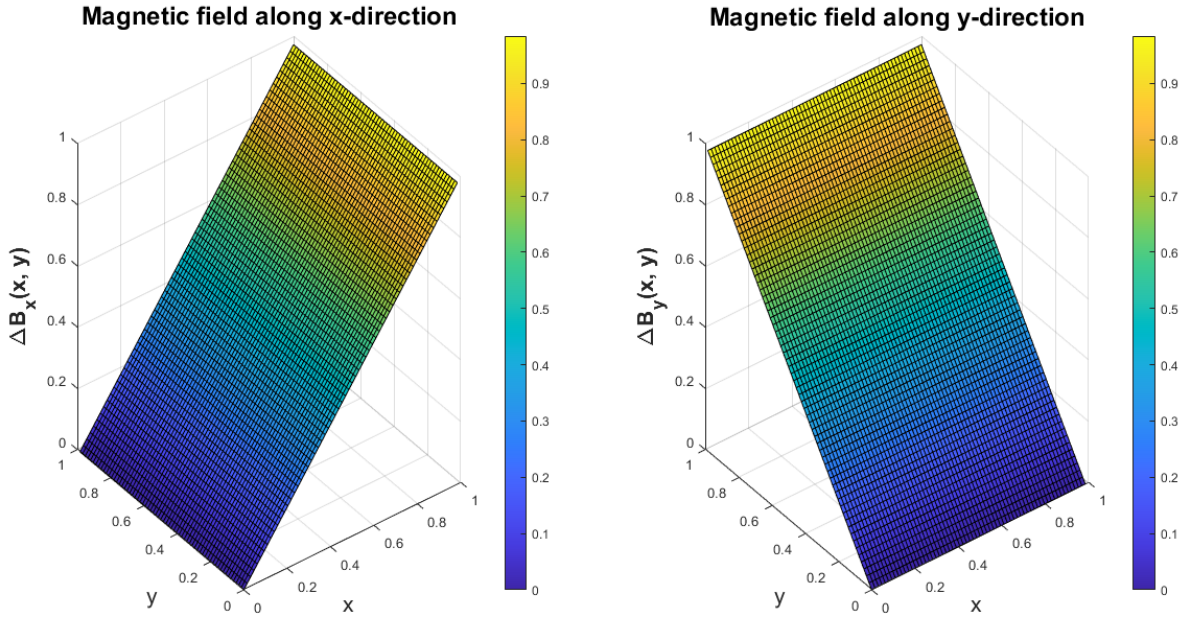

Figure B.2: Linear magnetic fields in both x- and y-directions

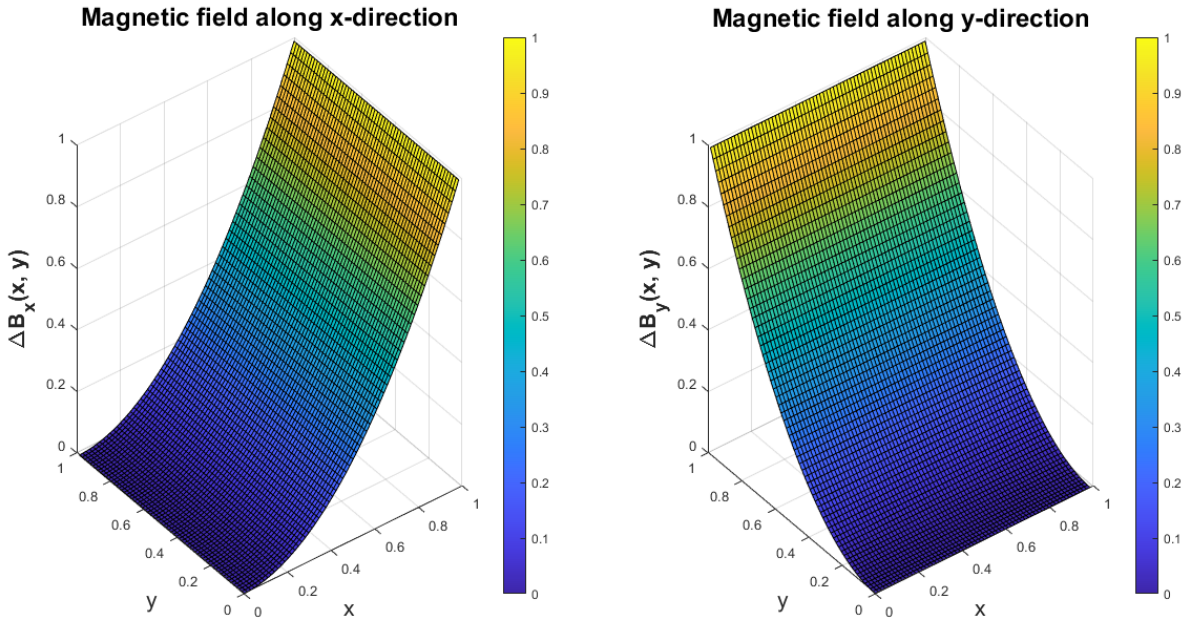

Figure B.3: Quadratic magnetic fields in both x- and y-directions

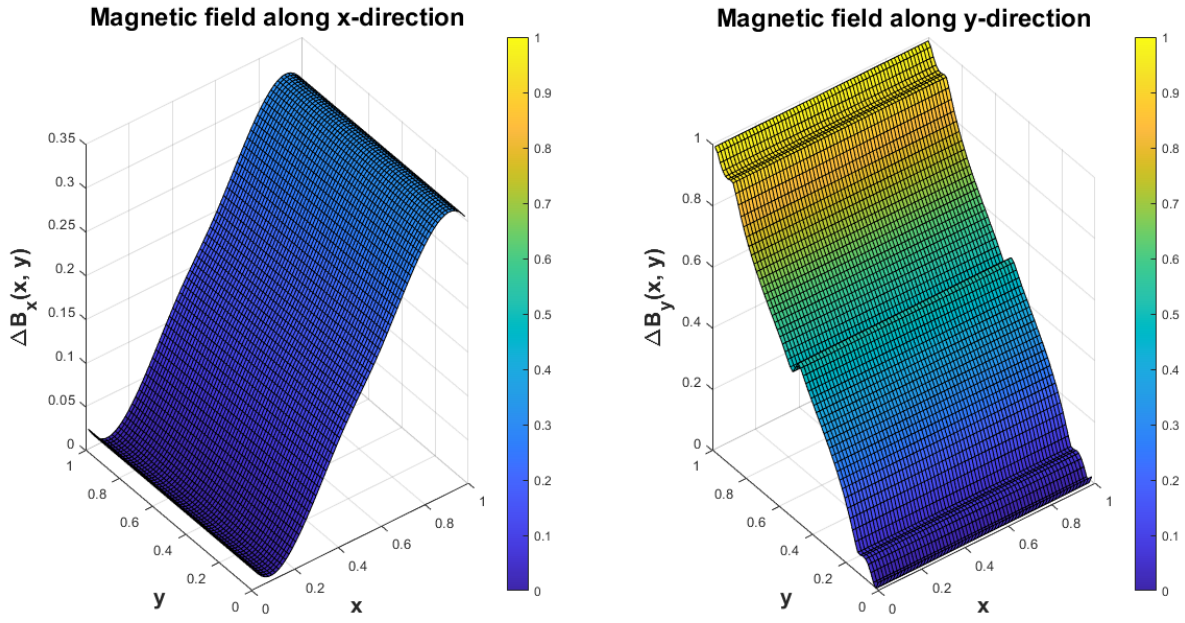

Figure B.4: Approximation of the gradient fields of the LF-MRI LUMC scanner in both x- and y-directions

B.1. Linear Magnetic Field

Figure B.5 corresponds to linear magnetic fields along the x- and y-directions from figure B.2. Both *fft2()* and *nufft2()* work likewise, the object is retrieved perfectly.
Since the two pair of sequences $\mathbf{s}$ and $\mathbf{t}$ are equal to their respective magnetic fields times the number of samples, i.e. $n\Delta B_x$ and $m\Delta B_y$, the perturbation parameter are $\delta^x = 0$ and $\delta^y = 0$. Both parameters are set to a number very close to zero in order to avoid a division by zero in equation (3.17).
The integers K^x and K^y for the nonuniform case equal 3. Nevertheless, looking at the matrices $D^x_{\mathbf{u}}$ and $D^y_{\mathbf{u}}$, whose columns have the $\mathbf{u}_0, \ldots, \mathbf{u}_2$ vectors, only the first column has nonzero elements. This means that the rank of the matrix is one and that the K value can be reduced to one for both cases.
When $K = 1$ is equivalent to the uniform case and that is why the object is retrieved perfectly.

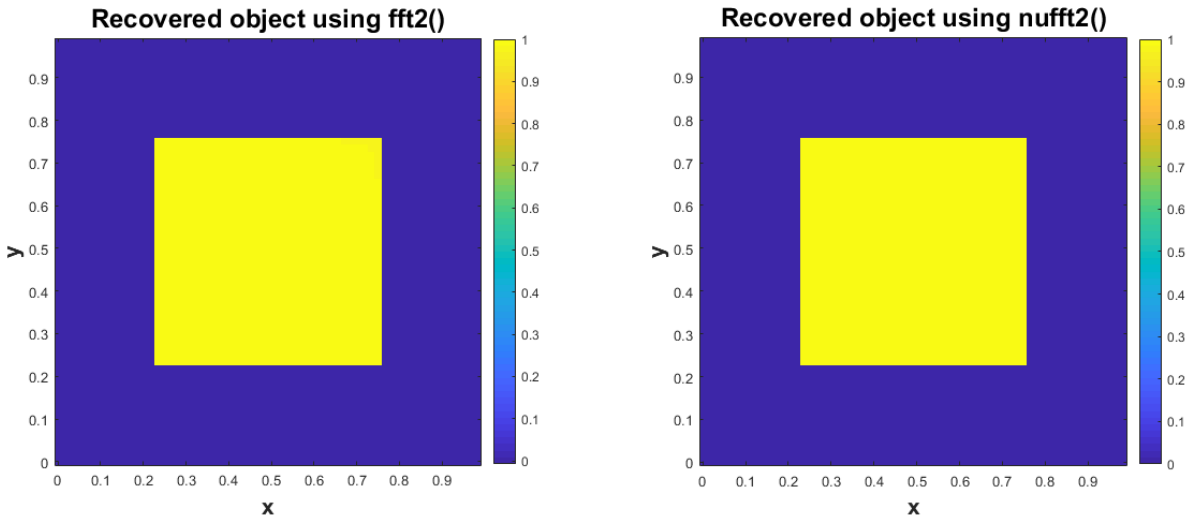

Figure B.5: To the left, recovered square object from linear magnetic fields (figure B.2) using the Fourier transform algorithm, *fft2()*. To the right, same object recovered using the nonuniform Fourier transform algorithm, *nufft2()*

B.2. Quadratic Magnetic Field

The square is placed in the quadratic fields from figure B.3. This time, the field is approximated to the closest equispaced grid, creating the sequences $\mathbf{s^x}$ and $\mathbf{s^y}$. Their respective $\mathbf{t}$ sequences are equal since any point in the magnetic fields is $\Delta B_x(r_i) = 1$ or $\Delta B_y(r_i) = 1$. These sequences can be seen in figure B.6, reshaped to a $m \times n$ matrix. The shape of these sequences is equal to the quadratic magnetic field but discretised to the equispaced points.
The maximum distances between the $\mathbf{s}$ sequence and the nonequispaced samples from the x and y fields are $\delta = 0.47$ in both cases and $K = 14$.

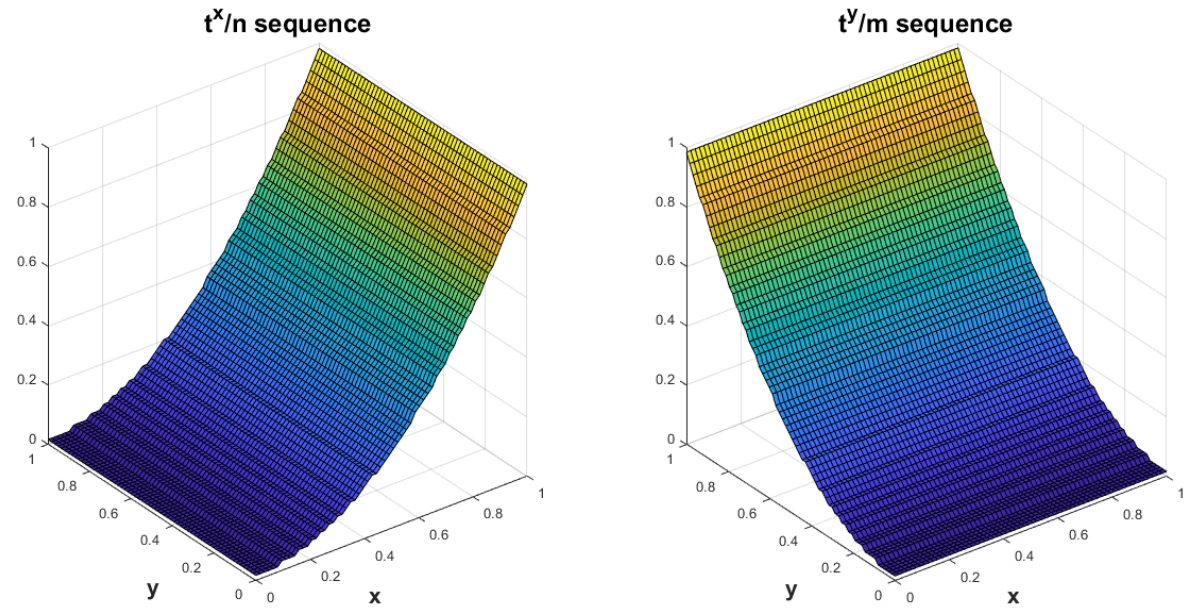

Figure B.6: Sequences t^x/n and t^y/m generated from the quadratic fields of figure B.3

Figure B.7 shows the performance of the uniform and nonuniform algorithms from a top view. The *fft2()* places the square incorrectly, and both linear and nonlinear cases have distortions in the amplitude. The explanation of this can be found in A.2.

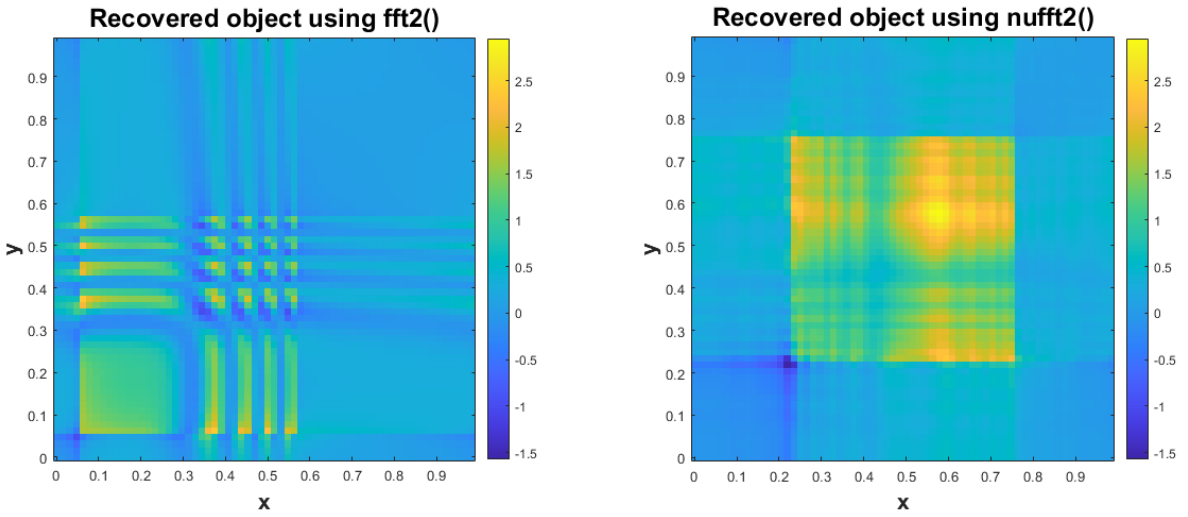

Figure B.7: To the left, recovered square object from quadratic magnetic fields (figure B.3) using the Fourier transform algorithm, *fft2()*. To the right, same object recovered using the nonuniform Fourier transform algorithm, *nufft2()*

Figure B.8 shows the front and side views which resemble the ones obtained in the 1D case, the right image of figure A.6. Therefore, in order to eliminate the amplitude distortions, the upper half of the k-space samples will be eliminated.

In a same way as for the one dimensional case, some k-space samples are eliminated. First the highest frequencies in the k_x-space, then the highest of the k_y-space and last both upper halves of k_x and k_y simultaneously, leading to just using a quarter of the k-space. The results are shown in figure B.9. The left image shows a smoother shape in the x-direction, because half of the k_x-space was removed, whereas in the y-direction keeps presenting the amplitude distortions seen in the right image of figure B.8. The central image presents the same shape as the previous image but with the x and y axis swapped. Because the the k_x-was kept intact while the upper half of the k_y-space was removed. The last image of figure B.8 shows a smooth shape in both directions because only the lower quarter of the k-space was used. Therefore, the front and side views have the same aspect as figure A.9.

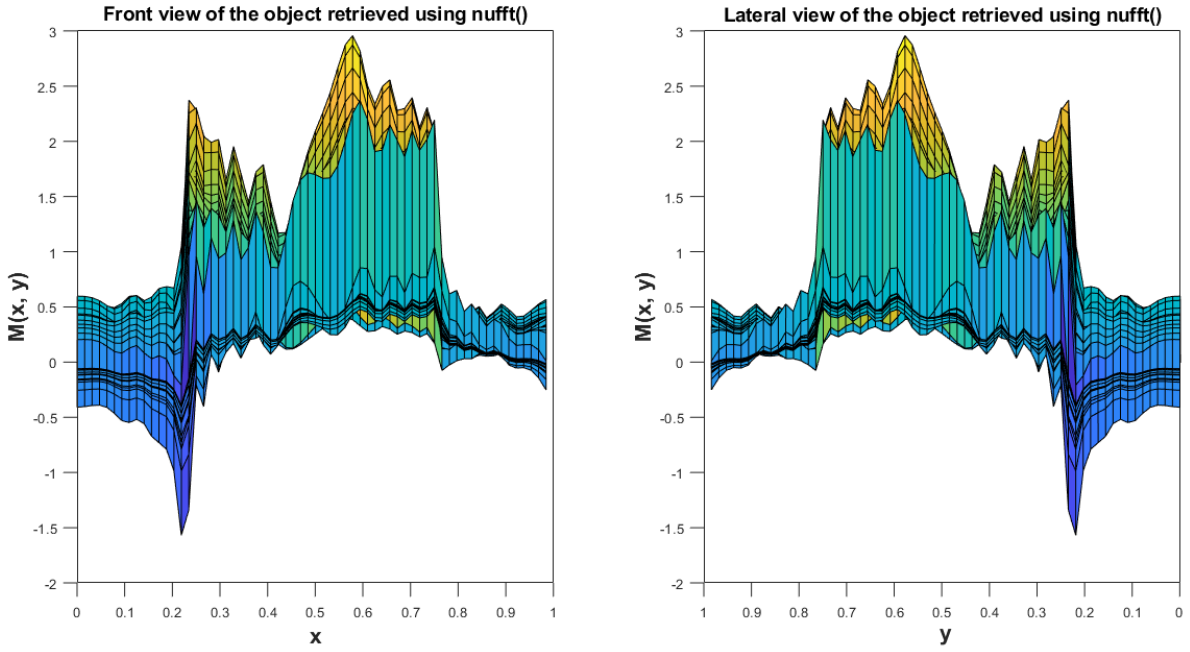

Figure B.8: Recovered square object from quadratic magnetic fields (figure B.3) using the nonuniform Fourier transform algorithm. The left image corresponds to the front view and the right image to the lateral view

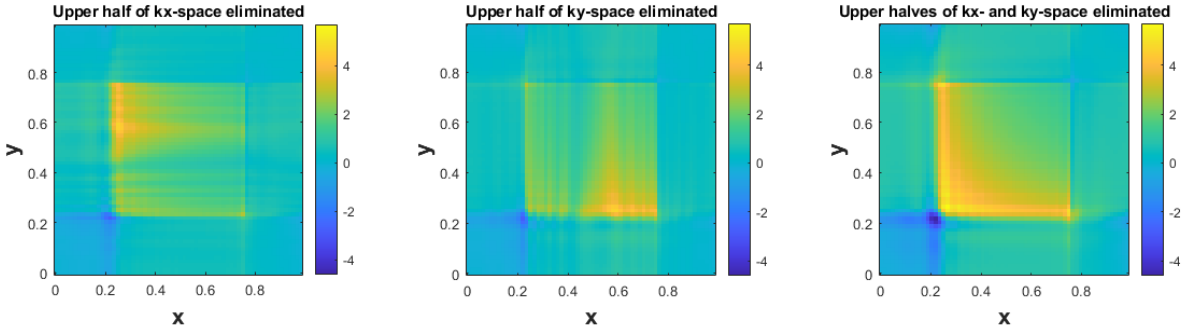

Figure B.9: Recovered square object from a quadratic magnetic field (figure B.3) using the *nufft2()* and eliminating the high frequencies in the k-space as explained in figure 8.3

B.2.1. Results Using CG and NUFFT

Figure B.10 shows the ideal object in the left image and the object retrieved using 500 iterations of the Conjugate Gradient method in the right image. Note that the colours of the ideal object have been slightly changed so that they match the colourbar of the object retrieved and both images can be compared.

The shape of the square can be differentiated. Nevertheless, at the bottom left part of the object retrieved some nonidealities can bee seen. Whereas the upper right part of this object is perfectly retrieved.

Looking at the right image of figure B.7, where one iteration of the CG is used, the shape of the object can be as well differentiated but the interior of the square presents many irregularities in the amplitude. This noise is eliminated when the number of iterations is increase as it can be seen in the right image of figure B.10.

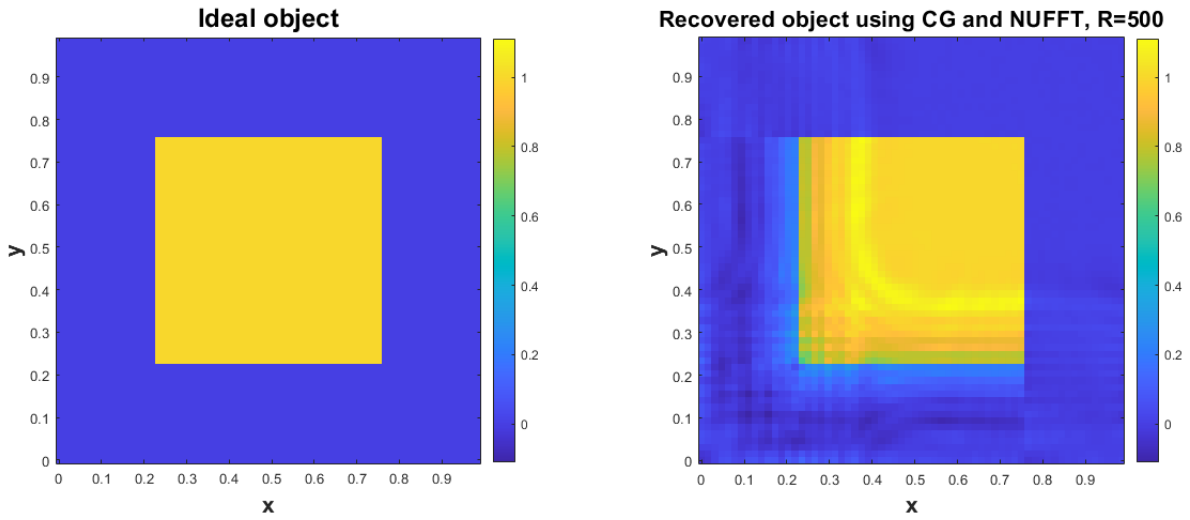

Figure B.10: To the left, ideal object. To the right, retrieved object using the NUFFT and $R = 500$ iterations of the CG from the quadratic magnetic fields, figure B.3

B.3. Low Magnetic Field Approximation

The fields of figure B.4 are approximations of the gradient fields of the MRI scanner of LUMC. The shape of these fields is chosen in order to have a magnetic field along the x-direction, $\Delta B_x(x, y)$, with nonequispaced samples in the x-direction but constant in the y-direction, and a magnetic field along the y-direction, $\Delta B_y(x, y)$, with nonequispaced samples in the y-direction but constant in the x-direction. This way, both look more like to the one dimensional case in section 6.2.1 and comparisons can be better understood.
The $\mathbf{t}$ sequences for the x- and y-gradients of figure B.4 are in figure B.11, reshaped to the $m \times n$ grid. Regarding the $\mathbf{t}^x$ sequence, it is equal to $\mathbf{s}^x$ since the highest value is $\Delta B_x(r_i) \approx 0.35$. The equispaced nodes are noticeable and the x-gradient can be seen clearly discretised in the $\mathbf{s}$ or $\mathbf{t}$ sequence. In the gradient along y-direction, $\mathbf{s}$ and $\mathbf{t}$ differ at $y = 1$, and the latter can be seen in the right image of figure B.11. This sequence is very similar to the linear field, except for the middle part and the peaks at the edges.
The perturbation parameters are $\delta^x = 0.4837$ and $\delta^y = 0.4896$, which holds equation (3.17), and gives $K = 14$ in equation (3.16). Nonetheless, the rank of the matrices $D_{\mathbf{u}}$ is less than fourteen and therefore, the nonuniform Fourier matrices from the fields ΔB_x and ΔB_y can be represented with less than fourteen vectors (equation (3.8)). This can be seen in section 8.3.

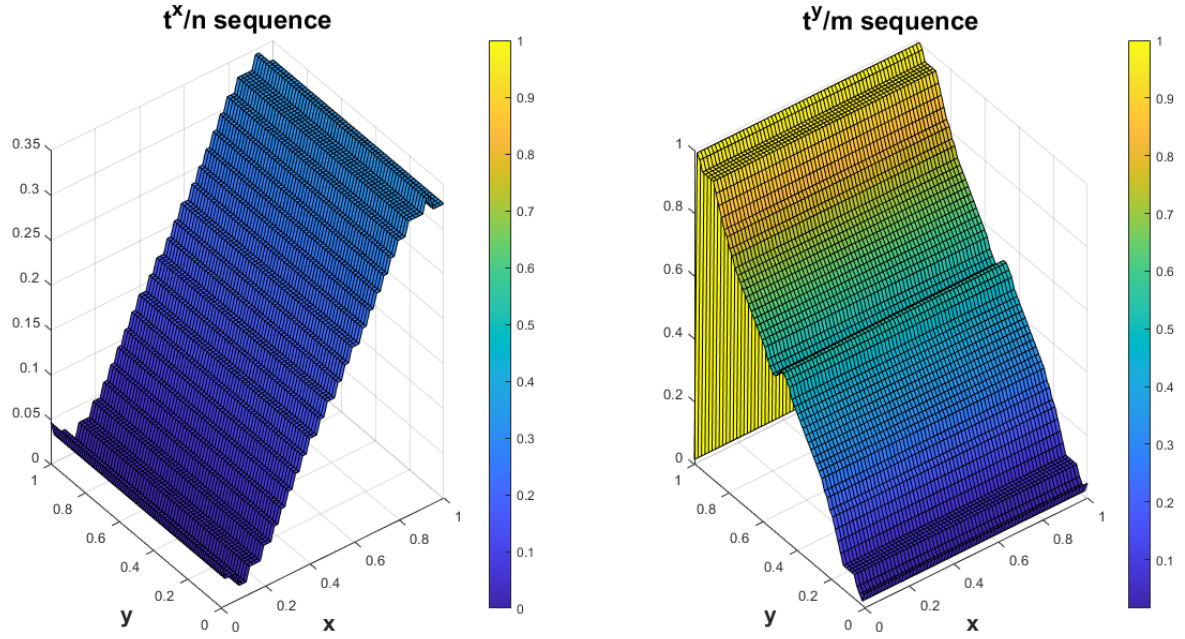

Figure B.11: Sequences t^x/n and t^y/m generated from the low approximation fields of figure B.4

The next figure B.12, shows the retrieved object using these approximated fields. Looking at the *fft2()*, left image of figure B.12, it can be seen that the object is placed to the left. This is because ΔB_x introduces a positive space delay since it is below the linear plane. Moreover, due to the oversampling, the square is shrunk. Note that in the 1D case, the displacement to the left did not exist because the low field of the x-gradient was in the $[0, 1]$ interval (see third image of figure 6.2). Now the values of the x-gradient field are in $[0, 0.35]$ (see left image of figure B.4).
Both *fft2()* and *nufft2()* present horizontal stripes in the middle of the square, due to the shape of the magnetic field in the y-direction at $y \approx 0.5$.

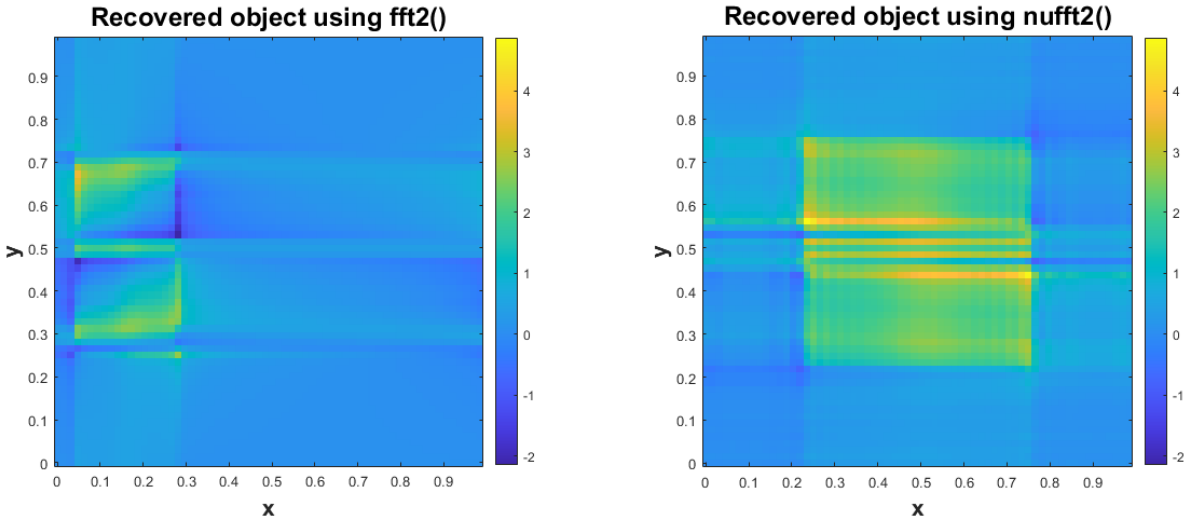

Figure B.12: To the left, recovered square object from the magnetic field approximations of the LF-MRI of LUMC (figure B.4) using the Fourier transform algorithm, *fft2()*. To the right, same object recovered using the nonuniform Fourier transform algorithm, *nufft2()*

Figure B.13 shows the front and side view of the right image of figure B.12. These two images are very similar to the right images of figures 6.6 and 6.9 respectively. The origin of the horizontal lines in the central part of the square in B.12 can be seen in the right image of B.13. This is due to the pronounced peaks in the object generated because of the nonbijective field in the central part of the y-gradient.

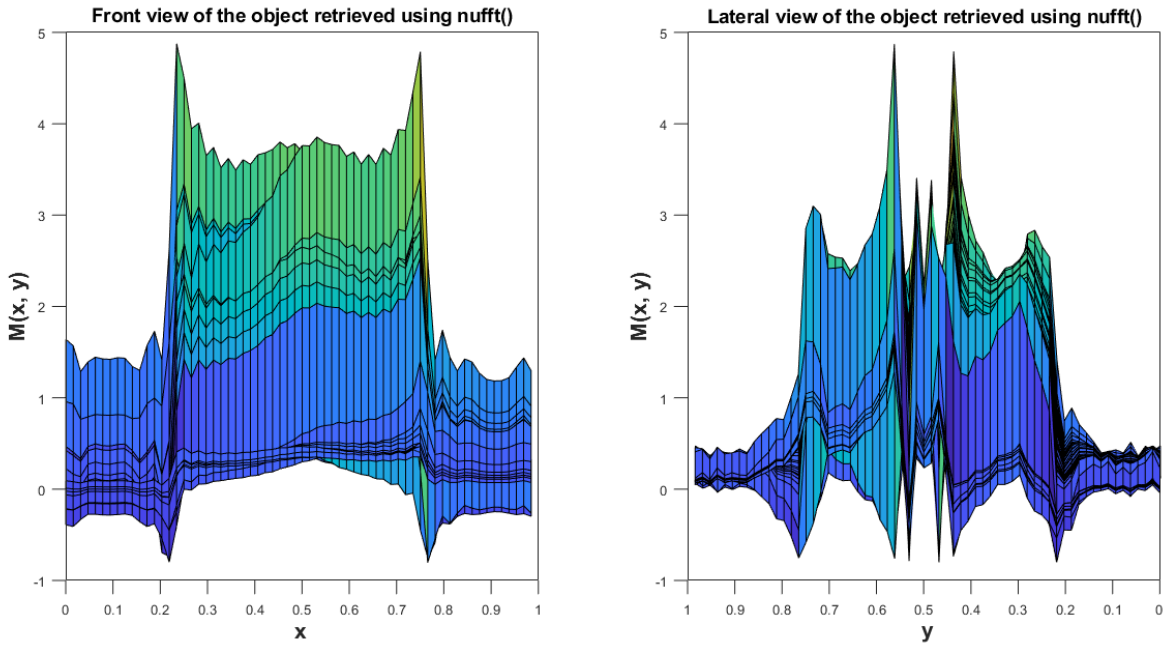

Figure B.13: Recovered square object from an approximation of a low magnetic fields (figure B.4) using the nonuniform Fourier transform algorithm. The left image corresponds to the front view and the right image to the lateral view

To smooth the shape of the object retrieved, the k-space samples are eliminated in figure B.14. Nevertheless, the horizontal stripes are not erased because of the nonidealities in the y-field are right on the object (see figure 6.8).

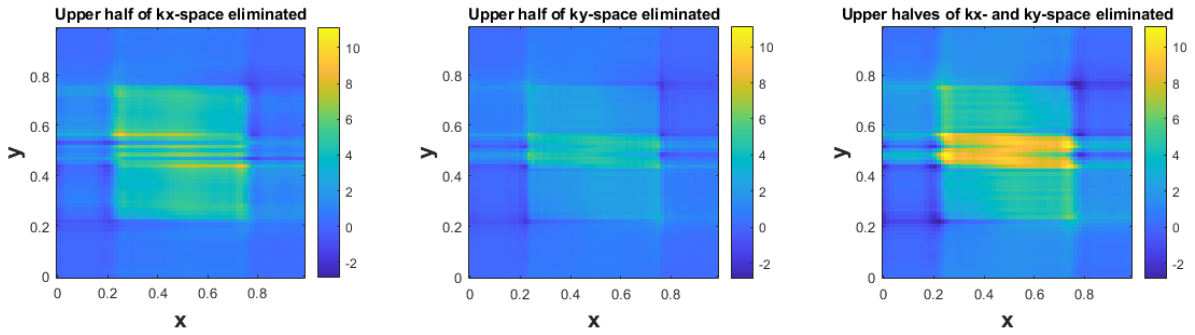

Figure B.14: Recovered square object from an approximation of the low magnetic field (figure B.4) using the *nufft2()* and eliminating the high frequencies in the k-space as explained in figure 8.3

B.3.1. Results Using CG and NUFFT

Figure B.15 shows the ideal object in the left image and the object retrieved using 500 iterations of the Conjugate Gradient method in the right image. Note that the colours of the ideal object have been slightly changed so that they match the colourbar of the object retrieved and both images can be compared.
Vertical lines can be seen at the left and right sides of the object retrieved due to the two bumps of the ΔB_x field at the edges. Whereas in the y-direction, the ΔB_y field looks more linear and the object does not present a noisy background in that direction.
Comparing this object retrieved to the on when using just one iteration of the Conjugate Gradient, figure B.12, it can be seen that the result is better when using 500 iterations. The horizontal lines are attenuated and the background is more uniform.

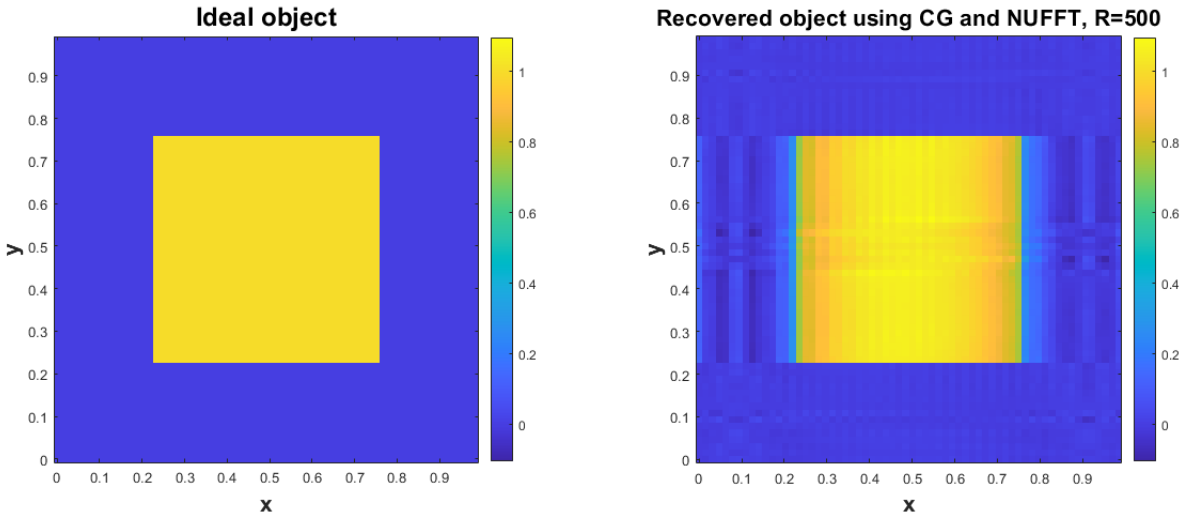

Figure B.15: To the left, ideal object. To the right, retrieved object using the NUFFT and $R = 500$ iterations of the CG from the approximation of the gradient fields from LF-MRI LUMC scanner, figure B.4

Bibliography

[1] Sarah Abdulla. Slice selection, 2020. URL https://www.radiologycafe.com/radiology-trainees/frcr-physics-notes/slice-selection.

[2] A. Aschoff, Paul Kremer, Bahram Hashemi, and Stefan Kunze. The scientific history of hydrocephalus and its treatment. *Neurosurgical Review*, 22(2-3):67–93, 1999. doi: 10.1007/s101430050035.

[3] PDQ Board. Adult central nervous system tumors treatment (pdq®), 2020. URL https://www.ncbi.nlm.nih.gov/books/NBK65982/.

[4] Ryan Compton, Stanley Osher, and Louis Bouchard. Hybrid regularization for mri reconstruction with static field inhomogeneity correction. In *2012 9th IEEE International Symposium on Biomedical Imaging (ISBI)*, pages 650–655. IEEE, 2012.

[5] Tobin A Driscoll, Nicholas Hale, and Lloyd N Trefethen. Chebfun guide, 2014.

[6] Allen D. Elster. Questions and answers in MRI, 2020. URL http://mriquestions.com/what-is-spin.html.

[7] M Espy, M Flynn, J Gomez, C Hanson, R Kraus, P Magnelind, K Maskaly, A Matlashov, Sh Newman, T Owens, et al. Ultra-low-field MRI for the detection of liquid explosives. *Superconductor Science and Technology*, 23 (3):034023, 2010.

[8] Jeffrey A Fessler, Sangwoo Lee, Valur T Olafsson, Hugo R Shi, and Douglas C Noll. Toeplitz-based iterative image reconstruction for mri with correction for magnetic field inhomogeneity. *IEEE Transactions on Signal Processing*, 53(9):3393–3402, 2005.

[9] Daniel Gallichan, Chris A Cocosco, Andrew Dewdney, Gerrit Schultz, Anna Welz, Jürgen Hennig, and Maxim Zaitsev. Simultaneously driven linear and nonlinear spatial encoding fields in mri. *Magnetic resonance in medicine*, 65(3):702–714, 2011.

[10] Latha Ganti. *External Ventricular Drain Placement*. Springer, New York, NY, 2016.

[11] MD Sevillano García, P Cacabelos Pérez, and J Cacho Gutiérrez. Alteraciones del líquido cefalorraquídeo y de su circulación: hidrocefalia, pseudotumor cerebral y síndrome de presión baja. *Medicine-Programa de Formación Médica Continuada Acreditado*, 10(71):4814–4824, 2011.

[12] Sarah J Gaskill, Arthur E Marlin, and Susan Rivera. The subcutaneous ventricular reservoir: an effective treatment for posthemorrhagic hydrocephalus. *Child's Nervous System*, 4(5):291–295, 1988.

[13] Per Christian Hansen, James G Nagy, and Dianne P O'leary. *Deblurring images: matrices, spectra, and filtering*. SIAM, 2006.

[14] Andrzej Herczyński. Bound charges and currents. *American Journal of Physics*, 81(3):202–205, 2013. doi: 10.1119/1.4773441.

[15] E Hoppe-Hirsch, F Laroussinie, L Brunet, C Sainte-Rose, D Renier, G Cinalli, M Zerah, and A Pierre-Kahn. Late outcome of the surgical treatment of hydrocephalus. *Child's nervous system*, 14(3):97–99, 1998.

[16] Pacific Neuroscience Institute. Endoscopic third ventriculostomy, 2020. URL https://www.pacificneuroscienceinstitute.org/hydrocephalus/treatment/endoscopic-techniques/endoscopic-third-ventriculostomy/.

[17] John David Jackson. From lorenz to coulomb and other explicit gauge transformations. *American Journal of Physics*, 70(9):917–928, 2002.

[18] Victor J Katz. The history of stokes' theorem. *Mathematics Magazine*, 52(3):146–156, 1979.

[19] Seo Jin Keun, Woo Eung Je, Katscher Ulrich, and Wang Yi. *Electro-magnetic tissue properties MRI*, volume 1. World Scientific, 2014.

[20] Abhaya V. Kulkarni, James M. Drake, Conor L. Mallucci, Spyros Sgouros, Jonathan Roth, and Shlomi Constantini. Endoscopic third ventriculostomy in the treatment of childhood hydrocephalus. *The Journal of Pediatrics*, 155(2):254–259.e1, 2009. doi: 10.1016/j.jpeds.2009.02.048.

[21] Serge Langlois, Michel Desvignes, Jean-Marc Constans, and Marinette Revenu. Mri geometric distortion: a simple approach to correcting the effects of non-linear gradient fields. *Journal of Magnetic Resonance Imaging: An Official Journal of the International Society for Magnetic Resonance in Medicine*, 9(6):821–831, 1999.

[22] K. M. Laurence and S. Coates. The natural history of hydrocephalus: Detailed analysis of 182 unoperated cases. *Archives of Disease in Childhood*, 37(194):345–362, 1962. doi: 10.1136/adc.37.194.345.

[23] Zhi-Pei Liang and Paul C Lauterbur. *Principles of magnetic resonance imaging*. SPIE Optical Engineering Press [u.a.], 2000.

[24] Patrick L. Lynch. Ommaya reservoir, 2020. URL https://commons.wikimedia.org/wiki/File:Ommaya_01.png.

[25] Christopher Nimsky, Oliver Ganslandt, Bernd Tomandl, Michael Buchfelder, and Rudolf Fahlbusch. Low-field magnetic resonance imaging for intraoperative use in neurosurgery: a 5-year experience. *European Radiology*, 12(11):2690–2703, 2002. doi: 10.1007/s00330-002-1363-9.

[26] Johnes Obungoloch, Joshua R. Harper, Steven Consevage, Igor M. Savukov, Thomas Neuberger, Srinivas Tadigadapa, and Steven J. Schiff. Design of a sustainable prepolarizing magnetic resonance imaging system for infant hydrocephalus. *Magnetic Resonance Materials in Physics, Biology and Medicine*, 31(5):665–676, 2018. doi: 10.1007/s10334-018-0683-y.

[27] T O'Reilly, WM Teeuwisse, and AG Webb. Three-dimensional mri in a homogenous 27 cm diameter bore halbach array magnet. *Journal of Magnetic Resonance*, 307:106578, 2019.

[28] Children's Queensland. Shunt surgery fact sheet, 2020. URL https://www.childrens.health.qld.gov.au/fact-sheet-shunt-surgery/.

[29] Harold L Rekate. The definition and classification of hydrocephalus: a personal recommendation to stimulate debate. *Cerebrospinal Fluid Research*, 5(1), 2008. doi: 10.1186/1743-8454-5-2.

[30] Diego Ruiz-Antolín and Alex Townsend. A nonuniform fast fourier transform based on low rank approximation. *SIAM Journal on Scientific Computing*, 40(1):A529–A547, 2018. doi: 10.1137/17m1134822.

[31] Jonathan Richard Shewchuk et al. An introduction to the conjugate gradient method without the agonizing pain, 1994.

[32] Bradley P Sutton, Douglas C Noll, and Jeffrey A Fessler. Fast, iterative image reconstruction for mri in the presence of field inhomogeneities. *IEEE transactions on medical imaging*, 22(2):178–188, 2003.

[33] SVoJa. Lego MRI cover picture, 2013. URL https://www.flickr.com/photos/92635297@N03/8457354783/.

[34] Quang M. Tieng and Viktor Vegh. Magnetic resonance imaging in nonlinear fields with nonlinear reconstruction. *Concepts in Magnetic Resonance Part B: Magnetic Resonance Engineering*, 39B(3):128–140, 2011. doi: 10.1002/cmr.b.20200.

[35] CH Tseng, GP Wong, VR Pomeroy, RW Mair, DP Hinton, D Hoffmann, RE Stoner, FW Hersman, DG Cory, and RL Walsworth. Low-field MRI of laser polarized noble gas. *Physical review letters*, 81(17):3785, 1998.

[36] User:Glogger, 2020. URL https://commons.wikimedia.org/wiki/File:Fourierop_rows_only.svg.

[37] Matthieu Vinchon, Harold Rekate, and Abhaya V Kulkarni. Pediatric hydrocephalus outcomes: a review. *Fluids and Barriers of the CNS*, 9(1), 2012. doi: 10.1186/2045-8118-9-18.

[38] Michael E Wall, Andreas Rechtsteiner, and Luis M Rocha. Singular value decomposition and principal component analysis. In *A practical approach to microarray data analysis*, pages 91–109. Springer, 2003.

[39] Janaka P Wansapura, Scott K Holland, R Scott Dunn, and William S Ball Jr. Nmr relaxation times in the human brain at 3.0 tesla. *Journal of Magnetic Resonance Imaging: An Official Journal of the International Society for Magnetic Resonance in Medicine*, 9(4):531–538, 1999.

[40] Benjamin C. Warf. Hydrocephalus in Uganda: the predominance of infectious origin and primary management with endoscopic third ventriculostomy. *Journal of Neurosurgery: Pediatrics*, 102(1):1–15, 2005. doi: 10.3171/ped.2005.102.1.0001.

[41] Benjamin C. Warf, Blake C. Alkire, Salman Bhai, Christopher Hughes, Steven J. Schiff, Jeffrey R. Vincent, and John G. Meara. Costs and benefits of neurosurgical intervention for infant hydrocephalus in sub-Saharan Africa. *Journal of Neurosurgery: Pediatrics*, 8(5):509–521, 2011. doi: 10.3171/2011.8.peds11163.

[42] Yudong Zhu. K-space synthesis for mr imaging in the presence of gradient field nonlinearity, October 21 2003. US Patent 6,636,756.